

University of Windsor

Scholarship at UWindor

Electronic Theses and Dissertations

Theses, Dissertations, and Major Papers

9-8-2023

Microstructure, Mechanical Properties and Electrical Conductivities of As-cast Al-0.3Mn Alloy

Wutian Shen
University of Windsor

Follow this and additional works at: <https://scholar.uwindsor.ca/etd>



Part of the [Mechanical Engineering Commons](#)

Recommended Citation

Shen, Wutian, "Microstructure, Mechanical Properties and Electrical Conductivities of As-cast Al-0.3Mn Alloy" (2023). *Electronic Theses and Dissertations*. 9241.

<https://scholar.uwindsor.ca/etd/9241>

This online database contains the full-text of PhD dissertations and Masters' theses of University of Windsor students from 1954 forward. These documents are made available for personal study and research purposes only, in accordance with the Canadian Copyright Act and the Creative Commons license—CC BY-NC-ND (Attribution, Non-Commercial, No Derivative Works). Under this license, works must always be attributed to the copyright holder (original author), cannot be used for any commercial purposes, and may not be altered. Any other use would require the permission of the copyright holder. Students may inquire about withdrawing their dissertation and/or thesis from this database. For additional inquiries, please contact the repository administrator via email (scholarship@uwindsor.ca) or by telephone at 519-253-3000ext. 3208.

**Microstructure, Mechanical Properties and Electrical Conductivities of As-cast
Al-0.3Mn Alloy**

By

Wutian Shen

A Thesis

Submitted to the Faculty of Graduate Studies
through the Department of Mechanical, Automotive and Materials Engineering
in Partial Fulfillment of the Requirements for
the Degree of Master of Applied Science
at the University of Windsor

Windsor, Ontario, Canada

2023

© 2023 Wutian Shen

**Microstructure, Mechanical Properties and Electrical Conductivities of As-cast
Al-0.3Mn Alloy**

by

Wutian Shen

APPROVED BY:

W. Abdul-Kader

Department of Mechanical, Automotive and Materials Engineering

X. Nie

Department of Mechanical, Automotive and Materials Engineering

H. Hu, Advisor

Department of Mechanical, Automotive and Materials Engineering

July 27th, 2023

DECLARATION OF CO-AUTHORSHIP / PREVIOUS PUBLICATION

I. Co-Authorship

I hereby declare that this thesis incorporates material that is result of joint research, as follows:

In all cases, the key ideas, primary contributions, experimental designs, data analysis and interpretation, were performed by the authors, Dr. H. Hu as advisor and Dr. X. Nie and Dr. W. Abdul-Kader. Chapter 2, 3 and 4 were co-authored with Anita Hu, Ali Dhaif J. Wang and Sufeng Liu. Anita Hu, Ali Dhaif, J. Wang and Sufeng Liu contributed in bulk samples preparations.

I am aware of the University of Windsor Senate Policy on Authorship, and I certify that I have properly acknowledged the contribution of other researchers to my thesis and have obtained written permission from each of the co-author(s) to include the above material(s) in my thesis.

I certify that, with the above qualification, this thesis, and the research to which it refers, is the product of my own work.

II. Previous Publication

This thesis includes 4 original papers that have been previously published/submitted for publication in peer reviewed journals, as follows:

| Thesis Chapter | Publication title/full citation | Publication status* |
|--------------------|--|---|
| <i>Chapter [2]</i> | Al-Mn alloys for electrical applications: A review W. Shen, A. Hu, S. Liu, H. Hu | Journal of Alloys and Metallurgical Systems Volume 2, June 2023, 100008 |
| <i>Chapter [3]</i> | Nano Phase-containing Al-0.3Mn Alloy for Potential EV Applications: Microstructure, Tensile Behavior and Electrical Conductivity Wutian Shen, Anita Hu, Jun Wang, Ali Dhaif, Henry Hu | accepted for presentation and publication in the proceedings of ICNFA'23. |
| <i>Chapter [4]</i> | Section Thickness Effect on Microstructure, Mechanical and Electrical Properties of Permanent Steel Mold Cast Al-0.3Mn Alloy | Prepared for submission |

I certify that I have obtained a written permission from the copyright owner(s) to include the above published material(s) in my thesis. I certify that the above material describes work completed during my registration as a graduate student at the University of Windsor.

III. General

I declare that, to the best of my knowledge, my thesis does not infringe upon anyone's copyright nor violate any proprietary rights and that any ideas, techniques,

quotations, or any other material from the work of other people included in my thesis, published or otherwise, are fully acknowledged in accordance with the standard referencing practices. Furthermore, to the extent that I have included copyrighted material that surpasses the bounds of fair dealing within the meaning of the Canada Copyright Act, I certify that I have obtained a written permission from the copyright owner(s) to include such material(s) in my thesis.

I declare that this is a true copy of my thesis, including any final revisions, as approved by my thesis committee and the Graduate Studies office, and that this thesis has not been submitted for a higher degree to any other University or Institution.

ABSTRACT

Al-0.3Mn was prepared by permanent steel mold casting (PSMC) with three different section thicknesses of 6, 10, 20 mm, and also by squeeze casting (SC) with a cross-sectional thickness of 20 mm under an applied pressure of 90 MPa. The first group of samples was employed to investigate the difference in mechanical and electrical properties between the PSMC Al-0.3Mn Alloy and high-purity (HP) Al (99.9%). The results of tensile testing indicated that the ultimate tensile strength (UTS), yield strength (YS) of the cast HP Al significantly increased to 72.3 and 20.4 MPa from 59.2 and 14.0 MPa. However, the elongation (ϵ_f) and electrical conductivity of the cast alloy decreased to 28.9% and 45.6 %IACS from 37.1% and 61.1 %IACS. The large area fraction (2.1%) of the micron Al-Fe-Mn and nano Al-Mn phases in the PSMC Al-0.3%Mn alloy should be responsible for the difference in mechanical and electrical properties between the PSMC Al-0.3Mn alloy and the PSMC HP Al. The second group of samples was used to study the effect of section thicknesses on microstructure, mechanical and electrical properties of the PSMC Al-0.3Mn alloy. The UTS, YS, ϵ_f , and elastic modulus (E) of the alloy increased, when the section thickness of the PSMC Al-0.3Mn decreased to 6 mm from 20 mm. However, the porosity level increased to 1.25% from 2.58% with increasing the thickness to 20 mm from 6 mm, respectively. The fine microstructure and low porosity level resulted in the high mechanical properties and electrical conductivities of the 6 mm sample.

DEDICATION

I dedicate this thesis to beloved people, who have meant and continue to mean so much to me. To my father Yong Shen, and my mother Guihua Wu, who gave me all their love and support. Thank you for the continued encouragement.

For Their Endless Love and Support,

ACKNOWLEDGEMENTS

I would like to graciously express to Dr. Henry Hu, for providing me with the opportunity to work on this project in the engineering materials graduate program of the University of Windsor, and for his kindly suggestion, encouragement and excellent supervision of this research work.

Great thanks to Dr. Walid Abdul-Kade and Dr. Xueyuan Nie for the time given for my research thesis and presentations as my committee members and providing valuable suggestions for this project.

I am very grateful to Mr. Tim Bolger, Mr. Kevin Harkai, Mr. Ram Barakat and other technicians for the technical support, Anita Hu, Ali Dhaif, and all other group members for their technical assistance in the experimental analysis, tests, informative and valuable discussion in this research.

I would like to thank Dr. Narayan Kar and the Natural Sciences and Engineering Research Council of Canada, Nemak, Ford Motor Company of Canada, and University of Windsor for supporting this work.

Most of all I would like to express my deepest gratitude to my family: my parents for their love, understanding, encouragement and support.

TABLE OF CONTENTS

| | |
|--|-------------|
| DECLARATION OF CO-AUTHORSHIP / PREVIOUS PUBLICATION..... | III |
| ABSTRACT..... | VI |
| DEDICATION..... | VII |
| ACKNOWLEDGEMENTS | VIII |
| LIST OF FIGURES | XIII |
| LIST OF TABLES | XIX |
| CHAPTER 1: 1 | |
| 1.1 BACKGROUND | 1 |
| 1.2 OBJECTIVES OF THIS STUDY | 2 |
| 1.3 ORGANIZATION OF THE THESIS | 2 |
| CHAPTER 2: AL-MN ALLOYS FOR ELECTRICAL APPLICATIONS: A REVIEW 4 | |
| 2.1 INTRODUCTION | 4 |
| 2.2 ALUMINUM-MANGANESE SYSTEM..... | 7 |
| 2.2.1 Series of Al alloys..... | 7 |
| 2.2.2 Aluminum-manganese phase diagram..... | 7 |
| 2.2.3 Solubility of Mn in AlPhase | 9 |
| 2.2.4 Ternary phase diagrams for Al-Mn-TM systems | 9 |
| 2.3 MICROSTRUCTURE CHARACTERISTICS OF MN-CONTAINING AL ALLOYS ELECTRICAL RESISTIVITY AND CONDUCTIVITY OF AL-FE ALLOYS | 12 |
| 2.3.1 Mn-containing 3xxx and 7xxx Al alloys | 12 |
| 2.3.2 Al-Ni-Mn alloys | 14 |

| | | |
|-------|---|-----------|
| 2.3.3 | Quasicrystalline Al-Mn alloys..... | 20 |
| 2.4 | ELECTRICAL CONDUCTIVITIES OF MN-CONTAINING AL ALLOYS..... | 26 |
| 2.5 | MECHANICAL PROPERTIES OF MN-CONTAINING AL ALLOYS..... | 29 |
| 2.5.1 | Strengthening Al alloys..... | 29 |
| 2.5.2 | Solid solutions strengthening..... | 31 |
| 2.5.3 | Precipitation strengthening..... | 32 |
| 2.5.4 | Dislocation accumulation strengthening..... | 32 |
| 2.5.5 | Grain boundary strengthening..... | 33 |
| 2.6 | MECHANICAL PROPERTIES OF MN-CONTAINING AL ALLOYS..... | 34 |
| 2.6.1 | Mn-containing 3xxx and 7xxx Al alloys..... | 34 |
| 2.6.2 | Al-Ni-Mn alloys..... | 39 |
| 2.6.3 | Quasicrystalline Al-Mn alloys..... | 44 |
| 2.7 | SUMMARY..... | 46 |
| 2.8 | REFERENCES..... | 48 |
| | CHAPTER 3: NANO PHASE-CONTAINING AL-0.3MN ALLOY FOR POTENTIAL EV APPLICATIONS: MICROSTRUCTURE, TENSILE BEHAVIOR AND ELECTRICAL CONDUCTIVITY..... | 54 |
| 3.1 | 1. INTRODUCTION..... | 54 |
| 3.2 | 2. EXPERIMENTAL PROCEDURE..... | 56 |
| 3.2.1 | 2.1. Materials and Casting..... | 56 |
| 3.2.2 | 2.2. Porosity Measurement..... | 56 |
| 3.2.3 | 2.3. Microstructure Analysis..... | 57 |
| 3.2.4 | 2.4. Tensile Testing..... | 58 |

| | | |
|-------|---|-----------|
| 3.2.5 | 2.5. Measurement of Electrical Conductivity | 58 |
| 3.3 | 3. RESULTS AND DISCUSSION..... | 59 |
| 3.3.1 | 3.1. Microstructure | 59 |
| 3.3.2 | 3.2. Porosity Evaluation..... | 64 |
| 3.3.3 | 3.3. Tensile Behavior..... | 67 |
| 3.3.4 | 3.4. Electrical Conductivities..... | 72 |
| 3.4 | 4. SUMMARY | 74 |
| 3.5 | REFERENCES | 75 |
| | CHAPTER 4: SECTION THICKNESS EFFECT ON MICROSTRUCTURE, MECHANICAL AND ELECTRICAL PROPERTIES OF PERMANENT STEEL MOLD CAST AL-0.3MN ALLOY..... | 78 |
| 4.1 | INTRODUCTION | 78 |
| 4.2 | EXPERIMENT PROCEDURE | 81 |
| 4.2.1 | Material and casting..... | 81 |
| 4.2.2 | Cooling rate determination | 81 |
| 4.2.3 | Porosity measurement..... | 82 |
| 4.2.4 | Microstructure Analysis | 82 |
| 4.2.5 | Tensile Testing | 83 |
| 4.2.6 | Electrical Conductivity..... | 83 |
| 4.3 | RESULTS AND DISCUSSION..... | 85 |
| 4.3.1 | Solidification | 85 |
| 4.3.2 | Microstructural Constituents and Phase Identification..... | 87 |
| 4.3.3 | Dendrite size | 94 |

| | |
|---|------------|
| 4.3.4 Porosity evaluation | 97 |
| 4.3.5 Tensile Properties | 100 |
| 4.3.6 Deformation and Strain Hardening..... | 101 |
| 4.4 ELECTRICAL CONDUCTIVITIES..... | 107 |
| 4.5 CONCLUSIONS..... | 109 |
| 4.6 REFERENCES | 111 |
| CHAPTER 5: CONCLUSIONS..... | 115 |
| CHAPTER 6: FUTURE WORK..... | 118 |
| APENDICES..... | 119 |
| VITA AUCTORIS | 121 |

LIST OF FIGURES

| | |
|--|----|
| Figure 2.1 Al-rich corner of equilibrium binary aluminum-manganese phase [11].... | 8 |
| Figure 2.2 Solubility of Mn in (Al) [13] | 8 |
| Figure 2.3 Partial isothermal sections of Al-Mn-TM ternary phase diagrams: a) Al-Cu-Mn at 750 °C, b) Al-Co-Mn at 800 °C, c) Al-Ni-Mn at 750 °C, d) Al-Fe-Mn at 875 °C, e) Al-Zn-Mn at 600 °C, f) Al-Cu-Mn at 700 °C and g) the compositional regions of the Al-Pd-Mn pha..... | 11 |
| Figure 2.4. As-cast AA3xxx with (a) 0.05 wt%, (b) 0.29 wt%, and (c) 1.04 wt% Mn [18]..... | 16 |
| Figure 2.5. As-cast microstructure of experimental Al-Mn-Mg 3004 alloys with Mn contents: (a) 1.06 (M10), (b) 1.19 (M12), (c) 1.52 (M15), and (d)–(e) 2.05 (M20) wt %, respectively [20]..... | 17 |
| Figure 2.6 Distribution of dispersoids in experimental Al-Mn-Mg 3004 alloys with Mn contents after 375 °C/48 h: (a) 1.06, (b) 1.19, (c) 1.52, and (d) 2.05 wt%, respectively [20]..... | 18 |
| Figure 2.7 Distribution of dispersoid free zone in experimental Al-Mn-Mg 3004 alloys with Mn contents after 375 °C/48 h: (a) 1.06 (M10), (b) 1.19 (M12), (c) 1.52 (M15), and (d) 2.05 (M20) wt%, respectively [20]..... | 19 |
| Figure 2.8 SEM Back-scattered micrographs showing microstructures of TRC Mn-containing 3003 alloy sheets after cold-rolling and various annealing conditions: (a) cold-rolling, and annealing at (b) 530 °C/20 min, (c) 530 °C/15 h, (d) 450 °C/5 h, (e) 450 °C/5 h+ 530 | 19 |

| | |
|---|----|
| Figure 2.9 TEM micrograph showing the dislocation structure of the AA7000 series alloys containing 0.8 wt% Mn. (Arrows indicate Mn-dispersoids) [7]. | 23 |
| Figure 2.10 SEM photomicrographs of Al-Ni-Mn alloys cast with 90 K/s cooling rate. (a) Al-6Ni-4Mn, (b) Al-6Ni-3Mn, (c) Al-6Ni-2Mn, (d) Al-4Ni-4Mn, (e) Al-4Ni-3Mn, (f) Al-4Ni-2Mn [22]. | 23 |
| Figure 2.11 Measured area fractions of O phase as a function of cooling rate[22]. | 24 |
| Figure 2.12 Microstructure characteristics of (a) Al-4Ni and (b) Al-4Ni-2Mn alloys illustrated by SEM pictures; (c) eutectic $Al_9(Ni,Mn)_2$ phase displayed by TEM picture; and diffraction patterns indexed to $Al_9(Ni,Mn)_2$ phase on (d) [001] and (e) [101] axis [23] | 24 |
| Figure 2.13 (a) cellular arrangement of the Al-1 wt% Mn alloy and (b) dendritic arrangement of the Al-1 wt% Ni alloy. Microstructural evolution of the Al-1 wt% Mn1 wt% Ni alloy casting showing (c) cellular, (d) transition and (e) dendritic growth regimes [25] | 25 |
| Figure 2.14 SEM pictures depicting the microstructures of the binary 94Al-6Mn alloy cast in the Cu die with the diameters of (a) \varnothing 4 mm,(b) \varnothing 2 mm, and (c) \varnothing 1 mm [34]. | 28 |
| Figure 2.15 (a) hexagonal λ -Al ₄ Mn phase, (b) b decagonal phase (D-phase) and (c) orthorhombic L-phase revealed microstructure of 94Al-6Mn by TEM pictures and electron diffraction patterns [34]. | 28 |
| Figure 2.16 SEM pictures showing microstructures of 94Al-4Mn-2Fe alloys cast in Cu dies with the diameters of \varnothing 1-4 mm. Low magnification: a-c, and high magnification: d-f [34]. | 29 |

| | |
|--|----|
| Figure 2.17 crystalline Al ₆ (Mn, Fe) phase and quasicrystalline D-phase and I-phase identified by TEM and diffraction analyses in the 94Al–4Mn–2Fe alloy [34]. | 30 |
| Figure 2.18 Mean grain size of the Al-rich matrix as a function of dissolved Mn content [36]. | 30 |
| Figure 2.19 Time vs. temperature curves for heat treatments of (a) H1, (b) H2, and (c) H3 [18]. | 33 |
| Figure 2.20 Mn content-dependent tensile properties of the extruded AA7xxxx wrought Al alloys [7]. | 36 |
| Figure 2.21 Tensile properties of Mn-containing 6000 series Al alloy and commercial 6061 Al alloy. (a) extrusion and (b) T6 heat treatment [7]. | 37 |
| Figure 2.22 Microhardness at room temperature (a) and YS at 300 °C (b) with Mn contents [20]. | 37 |
| Figure 2.23 Creep curves at 300 °C of experimental alloys after 375 °C/48 h [20]. | 38 |
| Figure 2.24 Effects of cooling rates on the yield strengths of the Al-Ni-xMn alloys prepared under different cooling rates [22]. | 38 |
| Figure 2.25 Mn influence on (a) hardness, and YS and UTS and elongation (EL) of the Al-4Ni alloy at (b) 25 °C and (c) 250 °C [23]. | 40 |
| Figure 2.26 Vickers microhardness of the Al–1 wt% Mn and Al–1 wt% Mn–1 wt% Ni cast alloys as a function of the cellular (λ_C) and primary dendritic (λ_1) spacings ($\lambda_C/1-1/2$), and R ² is the coefficient of determination [25]. | 41 |
| Figure 2.27 Hall–Petch grain size dependence of the pre- and unmilled Al samples, and pure nanocrystalline Al for comparison [36]. | 43 |

| | |
|---|----|
| Figure 2.28 Compressive engineering stress–strain curves at room temperature for Al-Mn-Mm alloys [26]. | 44 |
| Figure 3.1 SEM micrographs showing microstructure of PSMC Al-0.3Mn alloy, (a) low and (b) high magnifications, and EDS spectra identifying (c) primary Al phase, (d) micron Al-Fe-Mn phase, and (e) nano Al-Mn phase. | 61 |
| Figure 3.2 SEM micrograph showing microstructure of PSMC HP Al (99.9%), (a) low (b) high magnifications, and EDS spectra identifying (c) primary Al phase, (d) Al-Fe intermetallic phase, | 63 |
| Figure 3.3 Micrographs in binary black and white images showing the contents of intermetallics in (a) the PSMC Al-0.3% Mn alloy and (b) the PSMC HP Al. | 63 |
| Figure 3.4 Area Fractions of the PSMC Al-0.3Mn alloy and HP Al (99.9%). | 64 |
| Figure 3.5 Binary black and white images showing porosity in (a) PSMC Al-0.3Mn alloy and (b) PSMC HP Al. | 65 |
| Figure 3.6 Porosity contents of the PSMC Al-0.3Mn alloy and HP Al (99.9%). | 66 |
| Figure 3.7 Typical engineering stress vs. strain curves of the PSMC Al-0.3Mn alloy and PSMC HP Al. | 66 |
| Figure 3.8 True stress vs. strain curves. | 70 |
| Figure 3.9 Strain hardening curves | 71 |
| Figure 3.10 Electrical conductivities | 71 |
| Figure 4.1 Cooling curves of the PSMC Al-0.3Mn alloy with the section thicknesses of 6, 10 and 20 mm. | 85 |
| Figure 4.2 Cooling rate of the PSMC Al-0.3Mn alloy vs. section thicknesses. | 86 |

| | |
|--|-----|
| Figure 4.3 Simulation on solidification of the the PSMC Al-0.3Mn alloy with the three section thicknesses of 6, 10 and 20 mm, a) 20% b) 40% c) 60%, and d) 80% solidified. | 87 |
| Figure 4.4 SEM micrographs showing microstructures of the PSMC Al-0.3Mn alloy with the section thicknesses of (a) 6, (b) 10, and (c) 20 mm, respectively..... | 89 |
| Figure 4.5 Enlarged SEM micrograph showing the presence of the nano eutectic Al-Mn phase in the section of 10 mm, respectively..... | 89 |
| Figure 4.6 EDS spectra (a), (b), and (c) for the areas containing the primary α -Al phase (area A, dark grey), the nano Al-Mn intermetallic phase (area B, light white), and micron Al-Fe-Mn intermetallic phases (area C, light grey), as shown in Figure 6(b), respecti.... | 90 |
| Figure 4.7 Binary black and white images showing the eutectic content in the PSMC Al-0.3Mn alloy with the section thicknesses of (a) 6, (b) 10, and (c) 20 mm, respectively. | 93 |
| Figure 4.8 Area fractions of the intermetallic phases in the PSMC Al-0.3Mn alloy vs. section thickness. | 94 |
| Figure 4.9 Optical micrographs revealing the primary α -Al dendrites in the PSMC Al-0.3Mn alloy with the section thicknesses of 6, 10, and 20 mm, respectively..... | 96 |
| Figure 4.10 Average primary dendrite size in the PSMC Al-0.3Mn alloy with the section thicknesses of 6, 10 and 20 mm..... | 96 |
| Figure 4.11 Binary black and white images showing porosity in the PSMC Al-0.3Mn alloy with the section thicknesses of (a) 6, (b) 10 and (c) 20 mm, respectively..... | 99 |
| Figure 4.12 Porosity contents vs. section thicknesses. | 99 |
| Figure 4.13 Representative engineering stress vs. strain curves of PSMC Al-0.3Mn alloy with different section thickness of 6, 10, and 20 mm, respectively..... | 100 |

| | |
|--|-----|
| Figure 4.14 Representative true stress vs. strain curves of the PSMC Al-0.3Mn alloy with the three section thicknesses of 6, 10, and 20 mm..... | 105 |
| Figure 4.15 Strain hardening rates vs. true strain for plastic deformation of the PSMC Al-0.3Mn alloy with the three section thicknesses of 6, 10 and 20 mm..... | 106 |
| Figure 4.16 Electrical conductivities vs. Section Thickness..... | 108 |

LIST OF TABLES

| | |
|--|-----|
| Table 2.1 Chemical compositions (wt%) of three AA3xxx samples with different Mn contents [18]..... | 14 |
| Table 2.2 Cooling rates of Cu cylindrical dies [34]..... | 25 |
| Table 2.3 Change of electrical resistivity ($\Delta\gamma$) of Al alloys with common elements and their solubilities [28]..... | 31 |
| Table 2.4 Electrical conductivity for three alloys sample in as-cast and heat treatment conditions %IACS [18]..... | 31 |
| Table 2.5 Flow stresses (σ_{flow}) of Alloy 3 at various strain rates [18]..... | 35 |
| Table 2.6 Flow stresses (σ_{flow}) at various strain rates for Alloy 2 [18]. | 36 |
| Table 3.1 Chemical compositions of Al-0.3Mn alloy and high purity (HP) Al | 56 |
| Table 3.2 Tensile properties of the PSMC Al-0.3Mn alloy and PSMC HP Al (99.9%) at room temperature | 67 |
| Table 3.3 Tensile toughnesses and resiliences of PSMC Al-0.3Mn alloy and PSMC HP Al (99.9%) at room temperature | 69 |
| Table 3.4 Best fit parameters for power equations | 72 |
| Table 4.1 Chemical composition of Al-0.3Mn alloy | 81 |
| Table 4.2 Cooling rates of the PSMC Al-0.3Mn alloys with the section thicknesses of 6, 10 and 20 mm..... | 86 |
| Table 4.3 Elements in analyzed phase shown in Figures 4 and 5..... | 91 |
| Table 4.4 Tensile properties of the PSMC Al-0.3Mn alloy with the section thicknesses of 6, 10 and 20 mm at room temperature..... | 101 |

| | |
|--|-----|
| Table 4.5 Tensile toughnesses and resiliences of PSMC Al-0.3Mn alloy at room temperature | 103 |
| Table 4.6 Best fit parameters for power equations | 104 |

Chapter 1:

1.1 BACKGROUND

With increasing fuel cost and environment concern, there is a large growth of battery-powered electrical vehicles (BEVs) in the automotive market. Due to the average weight of BEVs much higher than that of gasoline-powered vehicles (GPVs), it is necessary to develop new electric motors (EM) with lightweight materials, which have to be cheap, light, and highly efficient. To increase the efficiency of the EM, high electrical conductivity and low resistivity copper is usually used as the main material. As a lightweight material with a density of 2700 kg/m^3 and a melting temperature of 660°C , aluminum is 70 % lighter than copper, and its melting point 423°C lower than that of copper. Compared to copper, it is very easy to manufacture the rotor bars in the EM with aluminum via casting processes. However, the mechanical properties of the ultimate tensile strength (UTS) and the yield strength (YS) of pure aluminum are very low. The introduction of traditional alloying elements such Si, Mg and Cu adversely affects the electrical conductivity of these alloy alloys. Mn is a considerable alloying element due to its extremely low solubility, which is only 0.62 atomic percentage at 658°C (1.25 weight percentage). The addition of Mn to Al can increase the Al strengths and should have a minor effect on electrical conductivities of Al-Mn alloys. The tensile properties of light Al and Mg alloys are often influenced by their section thickness. The previous results of tensile testing indicate that ultimate tensile strength (UTS), yield strength (YS), elongation (e_f), strain hardening rate ($d\sigma/d\varepsilon$), as well as resilience (U_r) and toughness (U_t) increase significantly with a reduction in the section thickness of the alloy.

In various casting processes, it is demonstrated that permanent steel mold casting (PSMC) is a well-developed manufacturing process and has been extensively used to cast aluminum alloys.

1.2 OBJECTIVES OF THIS STUDY

The objectives of this work are outlined as follow:

- Review the mechanical properties and microstructure of Mn-containing Al alloys
- Study the effect of Mn addition on mechanical properties and electrical conductivity of HP Al;
- Investigate the effect of section thicknesses of 6, 10 and 20 mm on the mechanical and electrical properties of the PSMC Al-0.3Mn alloy with 0.3 wt% Mn;
- Analyze the microstructures of the Al-0.3Mn alloy influenced by the section thicknesses; and
- Understand the relation between microstructure and mechanical and electrical properties of Al-0.3Mn alloy.

1.3 ORGANIZATION OF THE THESIS

This thesis contains six chapters. Chapter 1 provides a general background of research and develop a lightweight EMs with light alloys, which should be cheap, light, and higher efficient, and the objectives of this study. Chapter 2 provides the literature review about the potential Al-Mn cast alloys for motor applications in electric vehicles. Chapters 3 presents the mechanical and electrical properties of PSMC Al-0,3Mn Alloy and HP Al (99.9%). And Chapter 4 reports the results of the effects of section thickness on microstructure, mechanical and electrical properties of PSMC Al-0.3Mn Alloy. Chapter 5

concludes and summarizes the present study. Lastly, Chapter 6 presents the recommendations for future work.

Chapter 2: Al-Mn alloys for electrical applications: A review

2.1 INTRODUCTION

Aluminum is the most abundant metallic element in Earth's crust and the most widely used nonferrous metal. Aluminum alloys are widely used alloys for aircraft components, automotive and electronic technology, due to their lightweight, good corrosion resistance, high specific strengths, and rigidity. Especially with the emergence of battery-powered electric vehicles (BEVs) in the past decade, light alloys have become popular in the automotive industry for the weight reduction of the electric vehicles. This is because the BEVs are, in general, heavier than gasoline or diesel-powered vehicles (GDVs) and the weight reduction of the BEVs is an urgent task for the automotive industry [1–3]. Currently, Al alloys used in the automotive industry contains the elements of Si, Mg and Cu in either wrought (5xxx and 6xxx series) or cast (3xx series) format. The Si, Cu and Mg-containing Al alloys in the as-cast condition have high strengths over 90 MPa in yield strength (YS) and 150 MPa in ultimate tensile strength (UTS). But high strength and high electrical conductivity are mutually exclusive in metallic materials. Commercially available Al alloys have low electrical conductivities less than 40%IACS, since the solubilities of Si, Cu and Mg in Al are relatively high, which are 1.60, 5.65 and 17.1 wt%, respectively. It is almost impossible for the automotive industry to manufacture conductive components in electric motors (EMs) with conventional high strength Al alloys due to their low electrical conductivities [4–6].

Manganese as a low-cost transition metal has a multifaceted array of industrial alloy uses in ferrous alloys-steels and cast iron, which can improve their strength, workability,

and wear resistance. The 3xxx series of Al alloys employs Mn as a major alloying element, and are used for applications, in which moderate strength combined with high ductility and excellent corrosion resistance is required. With low weight percent of Mn addition, the YS and UTS of Al alloys increase without sacrificing ductility, as Mn in aluminum-rich alloys forms a manganese dispersoid of Al_6Mn , which blocks the dislocation and changes the slip system by means of cross-slip [7]. Compared to common alloying elements, Si, Cu and Mg, Mn has a low solubility in pure aluminum, which minimizes the reduction in electrical conductivity. The maximum solubility of Mn is 1.25 wt% at 658 ° C [7,8]. Their current application includes beverage cans, pipes in the chemical industry for roof cladding, wall coverings, pressure vessels, roller shutters, roller doors and heat exchangers [8]. As a result, low Mn addition enables the development of low-cost Al alloys with not only high strengths but also high electrical conductivities, which are required for applications in BEVs. The potential application for Al-Mn alloys in the BEVs includes rotor bars in induction motors [1,2].

In the electric power industry (EPI), steel reinforced aluminum conductors (SRAC) are widely used for overhead transmission lines. The conductors are designed with different layers of aluminum and steel strands. The external pure aluminum strands conduct the electric current and the steel strands in the core are designed to endure the mechanical loads induced by various environmental conditions such as wind and ice. However, the interaction of steel and pure aluminum strands with the environment results in galvanic corrosion of the strands over time, which is externally invisible. The corrosion causes a reduction in the mechanical properties of the SRAC conductors leading to unexpected

failure. The development of high strength Al-Mn alloys with high electrical conductivities could remove steel strands as supporting cores in the conventional transmission line. As a result, the failure of the transmission line caused by galvanic corrosion could be eliminated. As such, lightweight high strength Al-alloy-based conductors of transmission line are highly demanded [9].

This review presents the series of wrought and cast Al alloys in association with alloying elements. According to Al-Mn binary phase diagram, the temperature-dependent solubilities of Mn in Al are revealed. The dependence of microstructure development of Al-Mn alloys on Mn contents and cooling rates is displayed. The influence of Mn content on mechanical properties and electrical conductivity of 3xxx and 7xxx Al alloys is discussed. The effect of heat treatment on the electrical conductivities of Mn-containing Al alloys is highlighted.

2.2 ALUMINUM-MANGANESE SYSTEM

2.2.1 Series of Al alloys

Aluminum alloys can be classified into two groups, which are wrought alloys and cast alloys [8,10]. The designation of wrought alloys has a four-digit system given by the aluminum association. The principal alloying element is expressed by the first digit. A modification of the specific alloys is shown by the second digit. A specific alloy in the series is identified by the third and fourth digits. A three-digit system is applied to the casting Al alloys. The major alloying element is indicated by the first digit. The second and third digits are used to define the purity of the aluminum.

2.2.2 Aluminum-manganese phase diagram

Phase diagrams can reveal the microstructural constituency and phase composition of materials in concentration-temperature coordinates. The equilibrium phase diagrams depict the phase constituents of materials in the equilibrium states. Fig. 2.1 presents the Al rich corner of the equilibrium binary Al-Mn phase diagram, which shows the precipitation of Al-Mn phase. This precipitation process can take place in cast slabs during the re-heating process before hot rolling. The amount and the size of the precipitated phase can be changed by adjusting the process parameters of temperature and time. Higher temperature and longer time mean coarser precipitates [11]. Based on the equilibrium Al-Mn phase diagram, manganese forms the particle Al_6Mn , which locks the dislocation and increase the strength of the alloys. After the reheating process, the precipitation of Al_6Mn phase can occur. The eutectic reaction

$L \leftrightarrow (Al) + Al_6Mn$ occurs at $658\text{ }^\circ\text{C}$ and the eutectic composition is $1.0 \pm 0.1\text{ at\% Mn}$ [12].

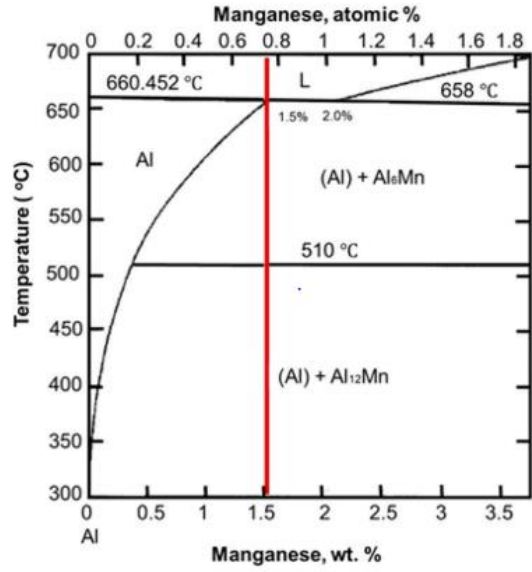


Figure 2.1 Al-rich corner of equilibrium binary aluminum-manganese phase [11]

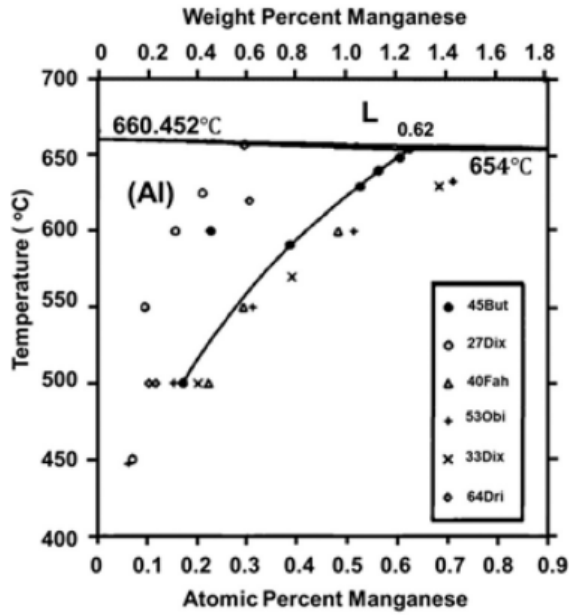


Figure 2.2 Solubility of Mn in (Al) [13]

2.2.3 Solubility of Mn in Al

Fig. 2.2 is an enlarged Al rich corner of Al-Mn binary phase diagram, which shows the maximum solubility of Mn in Al solid solution. According to Fig. 2.2, the solubility of manganese in aluminum increases with increasing temperature. Manganese has a relatively low solubility in aluminum. The maximum solubility is 0.62 at. percentage at 658 °C (1.25 wt percentage). In the range of 500 °C to 658 °C, the solubility of manganese in aluminum increases from 0.18 at% to 0.62 at%. Low solubility of Mn in Al could reduce the castability of Al alloys [13]. The maximum solubility of 1.25 wt% Mn in Al is also listed in reference [8]. However, Bubonyi and Barkoczy [11] indicated that the maximum solubility was 1.5% Mn in Al (Fig. 2.1). The difference in the values of the maximum solubility might result from the variation of the solidification processes. Further investigation on the Mn solubility is needed.

2.2.4 Ternary phase diagrams for Al-Mn-TM systems

Grushko et al. [14] presented the phase diagrams for Al-Mn-TM (TM = Fe, Co, Ni, Cu, Zn, Pd) systems as shown in Fig. 2.3. Their results showed that the solubility of Fe, Co, Ni, Cu, Zn and Pd in μ -Al₄Mn and λ -Al₄Mn was low, and the high-temperature T-Al₃Mn dissolved up to at least 14.5, 12, 16 and 7.5 of Fe, Cu, Zn and Pd, respectively. The metastable φ -Al₁₀Mn₃ was stabilized by Fe, Co, and Ni in wide ternary compositional regions. In Al-Co-Mn, such a region propagated up to Al₅Co₂. In alloys with Fe, Co and Ni, the ternary hexagonal so-called ζ -phase (P6₃/m, $a \cong 1.76$, $c \cong 1.25$ nm) was formed along ~80 at% Al. In alloys with Cu and Pd, the orthorhombic so-called R-phase (Bbmm, $a \cong 2.41$, $b \cong 1.25$, $c \cong 0.76$ nm) was found at similar compositions. Ternary phases in

the Al-rich region of the Al–Mn–Ni alloy system at 950, 850 and 750 °C were investigated by Balanetsky et al. [15]. Two new ternary intermetallic compounds were revealed: the φ -phase (Al₅Co₂-type, hP26, P63/mmc; $a = 0.76632(16)$ and $c = 0.78296(15)$ nm) and the κ -phase (κ -Al_{14.4}Cr_{3.4}Ni_{1.1}-type, hP227, P63/m; $a = 1.7625(10)$ and $c = 1.2516(10)$ nm). The formation of the O-phase (Pmmn; oP650; O-Al₇₇Cr₁₄Pd₉-type; $a = 2.3316(16)$, $b = 1.2424(15)$ and $c = 3.2648(14)$ nm) was identified in as-cast as well as samples annealed up to 958 h. The study of phase equilibria in the Al-rich region of the Al–Mn–Ni alloy system at 1000, 950, 850, 750, 700, 645 and 620 °C confirmed the presence of three ternary thermodynamically stable intermetallics, the φ -phase (Al₅Co₂-type, hP26, P63/mmc; $a = 0.76632(16)$, $c = 0.78296(15)$ nm), the κ -phase (κ -Al_{14.4}Cr_{3.4}Ni_{1.1}-type, hP227, P63/m; $a = 1.7625(10)$ and $c = 1.2516(10)$ nm), and the O-phase (Pmmn; oP650; O-Al₇₇Cr₁₄Pd₉-type; $a = 2.3316(16)$, $b = 1.2424(15)$ and $c = 3.2648(14)$ nm), as well as three ternary metastable phases, the decagonal D₃-phase with periodicity about 1.25 nm, the Al₉(Mn,Ni)₂-phase (Al₉Co₂-type, P1121/a, mP22; $a = 0.8585(16)$, $b = 0.6269(9)$, $c = 0.6205(11)$ nm, $\beta = 95.34(10)^\circ$) and the O₁-phase (base-centered orthorhombic, $a \approx 23.8$, $b \approx 12.4$, $c \approx 32.2$ nm) [16]. Walnsch et al. [17] studied the phase relations in the Mn-rich corner of the ternary Al–Mn–Ni system at 800 and 1000 °C regarding the phase equilibria and the stability of the disordered A2 phase. The decomposition of the disordered A2 phase by a eutectoid type of reaction ($A2 \rightleftharpoons A1 + B2$) in the Mn-rich corner of the Al–Mn–Ni system was investigated by means of transmission electron microscopy and in-situ X-ray diffraction. Calculations based on the present

description were in excellent agreement with the experimental data available in literature.

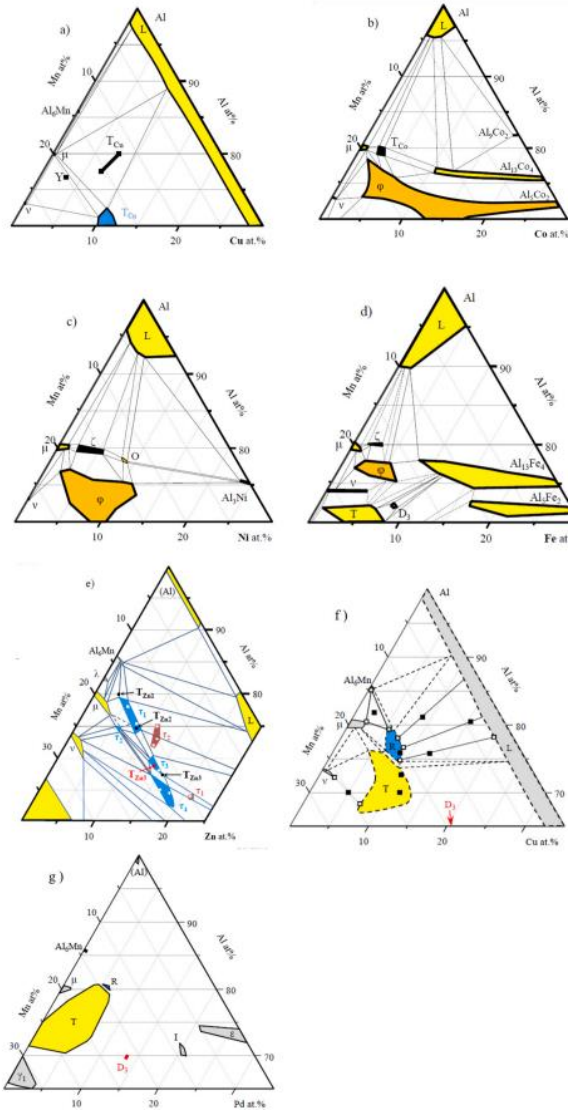


Figure 2.3 Partial isothermal sections of Al-Mn-TM ternary phase diagrams: a) Al-Cu-Mn at 750 °C, b) Al-Co-Mn at 800 °C, c) Al-Ni-Mn at 750 °C, d) Al-Fe-Mn at 875 °C, e) Al-Zn-Mn at 600 °C, f) Al-Cu-Mn at 700 °C and g) the compositional regions of the Al-Pd-Mn pha

2.3 MICROSTRUCTURE CHARACTERISTICS OF MN-CONTAINING AL ALLOY ELECTRICAL RESISTIVITY AND CONDUCTIVITY OF AL-FE ALLOYS

2.3.1 Mn-containing 3xxx and 7xxx Al alloys

Miri [18] showed that the hot deformation of AA3xxx Al alloys Mn was affected by Mn addition and homogenization treatment. Three ascast AA3xxx samples with different manganese contents of 0.05, 0.29 and 1.04 wt% were employed for microstructure observation. The first AA3xxx sample contained 0.36 wt% Fe, 0.05 wt% Mn, 0.15 wt% Si, 0.009 wt% Ti, while the second AA3xxx sample had 0.37 wt% Fe, 0.29 wt% Mn, 0.15 wt% Si, 0.008 wt% Ti. The third AA3xxx sample was prepared with the compositions of 0.37 wt% Fe, 1.04 wt% Mn, 0.15 wt% Si, 0.008 wt% Ti. The manganese weight percentages of the three alloys were quite different, although the composition variation in Fe and Ti was very little and negligible. The detailed chemical compositions of the three sample are listed in Table 2.1. The microstructures of the three alloys are shown in Fig. 2.4. As the Mn content rised from 0.05 to 0.29–1.04 wt%, the percentage of the Al-Mn intermetallic phase increased from 4.8 to 7.6–11.1%, and the size of the primary Al phase was reduced [18]. The formation of MnAl might result from the nonequilibrium solidification (rapid cooling), while the point of 1.25% Mn is present in the equilibrium phase diagram. The high Mn content promotes the formation of MnAl dispersoids. The massive presence of MnAl at the grain boundaries retards the grain growth and reduce the grain size. The high fraction of MnAl dispersoids causes large scatter of conductive electrons, which increases electrical resistivity and decreases electrical conductivities. Liu

and Chen [19,20] investigated the effect of Mn contents (up to 2 wt%) on the evolution of microstructure of Al–Mn–Mg 3004 alloy. Their results showed that, in the as-cast microstructure, the dominant intermetallics were interdendritic $\text{Al}_6(\text{MnFe})$ until to 1.5 wt% Mn. With further addition of Mn to 2 wt%, the blocky primary $\text{Al}_6\text{Mn}/\text{Al}_6(\text{MnFe})$ and high volume of fine $\text{Al}_6(\text{MnFe})$ intermetallics formed in the matrix, leading to the rapid increase on the volume fraction of intermetallics (Fig. 2.5). After the precipitation heat treatment (375 °C/ 48 h), the precipitation of dispersoids increased with increasing Mn contents and reached the peak condition in the alloy with 1.5 wt% Mn. However, the 2 wt% Mn resulted in the lowest volume fraction of dispersoids (Fig. 2.6) and highest volume of dispersoid free zone (Fig. 2.7). Huang et al. [21] developed a two-step annealing (TSA) process consisting of a prerecovery process (450 °C/5 h) and a following recrystallization process (530 °C/15 h) to tailor microstructure of a cold rolled twin-roll cast (TRC) Mn-containing 3003 alloy sheet. The distribution of the second phase particles was examined by SEM backscattered technique, as displayed in Fig. 2.8. It can be seen that small primary particles with a mean size about 0.5 μm distributed at the grain boundaries and along the rolling direction in the cold-rolled condition (Fig. 2.8a). For the single-step annealing (SSA) sample, copious fine dispersoids can be observed on the sub-grain boundaries during recovery at 530 °C for 20 min (Fig. 2.2b). After complete recrystallization, both dispersoids and primary particles became coarser after the long duration at 530 °C (Fig. 2.8c). In the case of TSA, a large number of fine precipitates emerged during pre-recovery treatment as well (Fig. 2.8d). Most of them are located on the sub-grain boundaries in the interior of grains, which was similar to the observation in Fig. 2.8b. However, some local regions

about 1–2 μm in thickness (marked by arrows in Fig. 2.2d) were observed in the vicinity of primary particles, where only few precipitates existed or even no precipitates at all. Nam and Lee [7] examined the microstructures and dislocation structures of the AA7000 series alloys containing 0.8 wt% Mn using transmission electron microscopy (TEM). Fig. 2.9 shows the TEM micrograph of the dislocation structure in the Mn-containing 7000 series alloy. The added manganese formed a manganese dispersoid of Al_6Mn . This dispersoid had an incoherent structural relationship with respect to the matrix, the face-centered cubic (FCC) crystal structure, in retarding the motion of dislocations that increased strengths. Once the dislocation was blocked by the dispersoid, it tended to change the slip system by means of cross-slip. This cross-slip allowed the deformation to maintain uniformly good ductility. TEM observation proved the above mentioned activities of dislocation by analyzing the characters of the dislocations around and away from the dispersoids.

Table 2.1 Chemical compositions (wt%) of three AA3xxx samples with different Mn contents [18]

| | Fe [wt%] | Mn [wt%] | Si [wt%] | Ti [wt%] | Al [wt%] |
|---------|----------|----------|----------|----------|----------|
| Alloy 1 | 0.36 | 0.05 | 0.15 | 0.009 | Bal. |
| Alloy 2 | 0.37 | 0.29 | 0.15 | 0.008 | Bal. |
| Alloy 3 | 0.37 | 1.04 | 0.15 | 0.008 | Bal. |

2.3.2 Al-Ni-Mn alloys

Due to their potential for high-temperature applications, Al–Ni–Mn alloys were attractive to the automotive and aerospace industries. Fan et al. [22] studied precipitation

hardening of eutectic and hypoeutectic Al-Ni alloys containing 2–4 wt% Mn with focus on the effect of the alloys' chemical composition and solidification cooling rate on microstructure. The alloys were cast in a fast-cooling die to achieve different cooling rates up to 90 K/s. SEM pictures of different Al-Ni-Mn alloys given in Fig. 2.10 depicts the influence of alloy composition on the microstructure of the alloys. The primary α -Al dendrites eutectic α -Al, eutectic Al₃Ni, and primary O phase were found in the cast alloys. Fig. 2.6 presents measured area fractions of O phase as a function of cooling rate. The quantity of O phase in the Al-Ni-Mn alloys was predominantly affected their chemical compositions. The high levels of Ni and/or Mn boosted the O phase formation as revealed in Figs. 2.10 and 11. The presence of Mn-enriched O phase (14.55 wt% Mn) suppressed the formation of the Mn-supersaturated solid solution as well as precipitation strengthening by Al₆Mn precipitates. Moreover, the O phase was rich in Ni (5.3 wt% Ni), of which formation reduced the amount of Al₃Ni eutectic that forms by the eutectic reaction.

The effect of Mn on microstructure of Al-4Ni alloy cast in a steel mold was investigated by Fang et al. [23]. Addition of Mn transformed the eutectics from Al₃Ni/ α -Al to Al₉(Ni,Mn)₂/ α -Al phases. Fig. 2.12 gives SEM and TEM micrographs revealing the microstructure characteristics of the Al-4Ni and Al-4Ni-2Mn alloys. The primary α -Al dendrites and eutectic phases were present in the two alloys. The primary α -Al in the Al-4Ni alloy had 0.28 wt% Ni. However, the Al-4Ni-2Mn alloy had the α -Al contained with about 0.43 wt% Ni and 1.6 wt% Mn. The Ni solubility in Al was very limited. But, the Mn solubility in Al was relatively high around 1.8 wt%. Therefore, the large amount of Mn in the primary α -Al phase was detected, compared to that of Ni. There are the cylindrical

eutectic intermetallic phases in both the Al-4Ni and Al-4Ni-2Mn alloys. The Ni content of the eutectic intermetallic phase in the Al-4Ni alloy 23.4 at%Ni, indicating a Al₃Ni phase. The eutectic intermetallic phase of the Al-4Ni-2Mn alloy contained 13.5 at%Ni and 3.7 at%Mn, which suggested the presence of the Al₉(Ni,Mn)₂ phase instead of Al₃Ni. Fig. 2.12c, d, and e present TEM picture and diffraction patterns of the intermetallic phase. The similar work was also performed by Yu et al. [24].

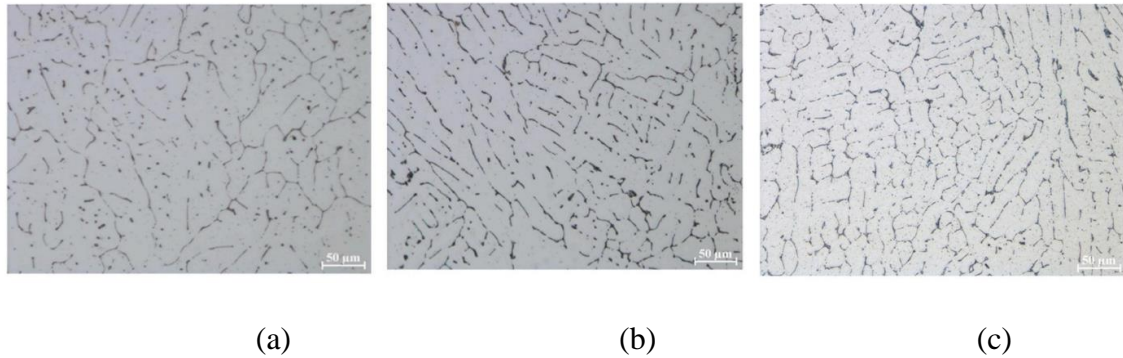


Figure 2.4. As-cast AA3xxx with (a) 0.05 wt%, (b) 0.29 wt%, and (c) 1.04 wt% Mn [18].

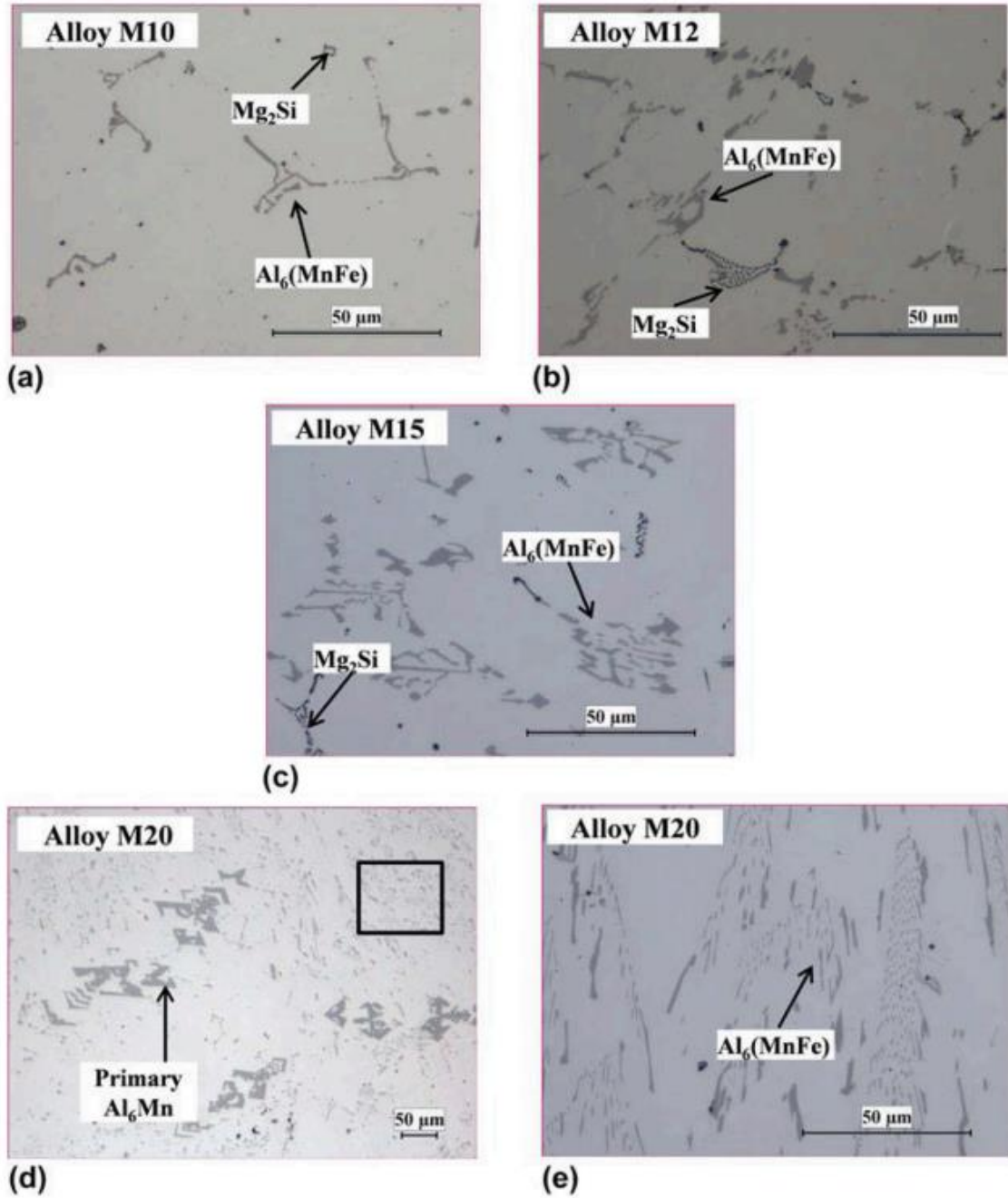


Figure 2.5. As-cast microstructure of experimental Al–Mn–Mg 3004 alloys with Mn contents: (a) 1.06 (M10), (b) 1.19 (M12), (c) 1.52 (M15), and (d)–(e) 2.05 (M20) wt %, respectively [20]

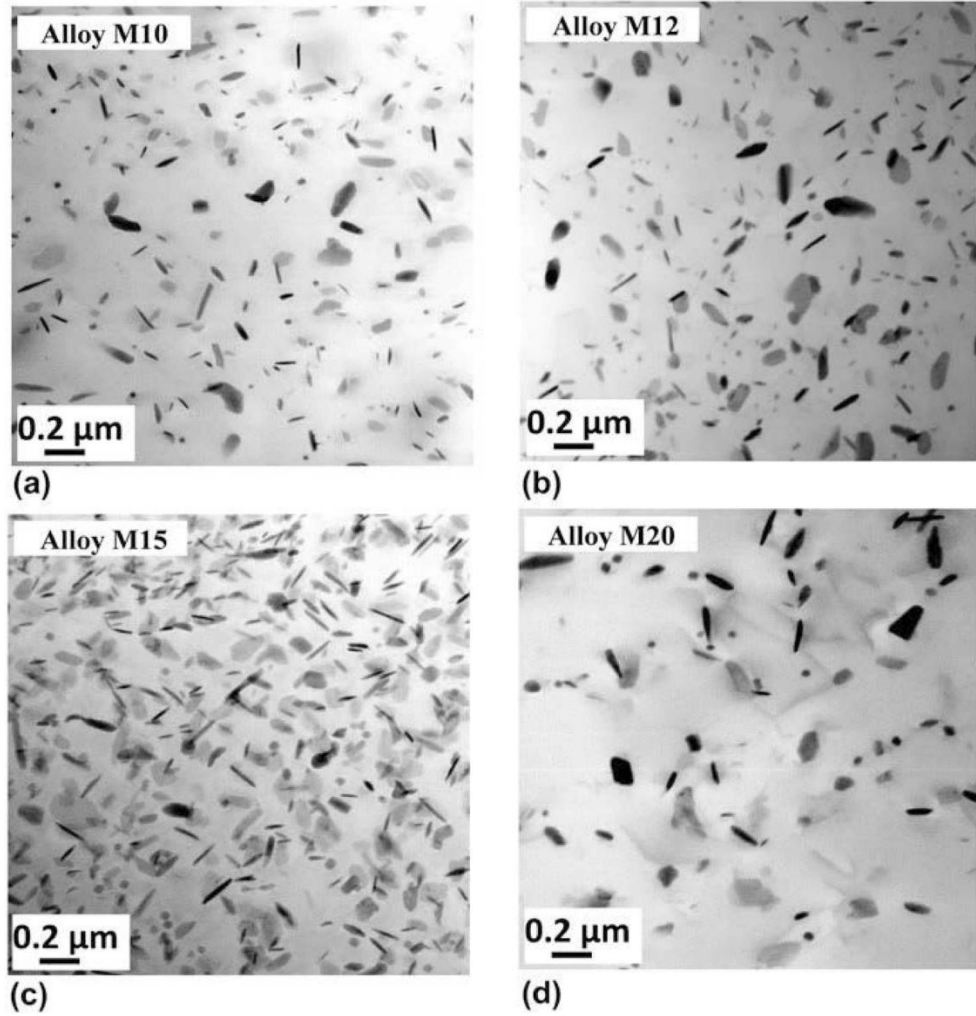


Figure 2.6 Distribution of dispersoids in experimental Al–Mn–Mg 3004 alloys with Mn contents after 375 °C/48 h: (a) 1.06, (b) 1.19, (c) 1.52, and (d) 2.05 wt%, respectively [20].

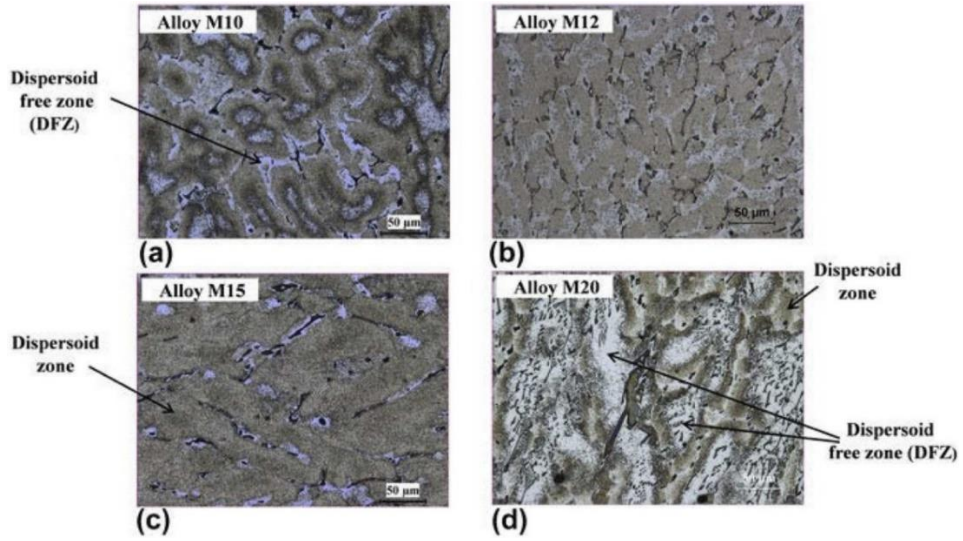


Figure 2.7 Distribution of dispersoid free zone in experimental Al–Mn–Mg 3004 alloys with Mn contents after 375 °C/48 h: (a) 1.06 (M10), (b) 1.19 (M12), (c) 1.52 (M15), and (d) 2.05 (M20) wt%, respectively [20].

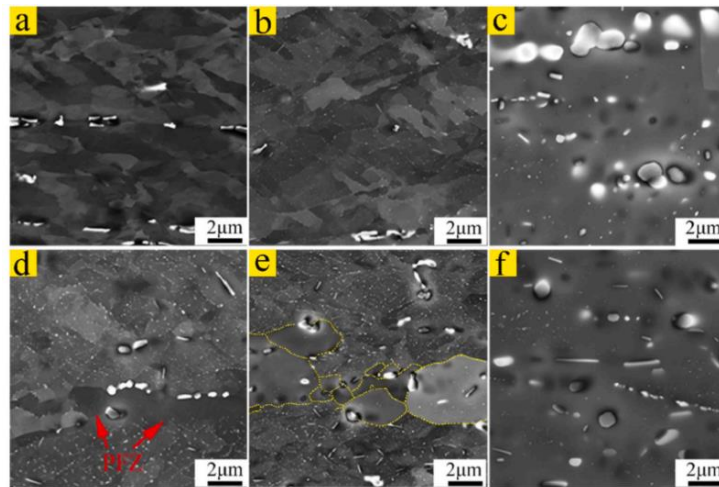


Figure 2.8 SEM Back-scattered micrographs showing microstructures of TRC Mn-containing 3003 alloy sheets after cold-rolling and various annealing conditions: (a) cold-rolling, and annealing at (b) 530 °C/20 min, (c) 530 °C/15 h, (d) 450 °C/5 h, (e) 450 °C/5

h+ 530

Oliveira et al. [25] studied the effect of Ni on the microstructure of Al-1 wt% Mn alloy prepared by directional solidification (DS). The microstructure of the directionally solidified (DS) Al-1 wt% Mn alloy was shown to be characterized by an α -Al primary phase having a cellular morphology with the eutectic mixture at the boundaries (Fig. 2.13). However, the morphology of the α -Al phase of the DS Al-1 wt % Mn-1 wt% Ni alloy casting depended on the magnitude of the experimental solidification cooling rate (CR). For $CR > 2.3$ °C/s, the morphology was cellular; in the range of $2.3 < CR < 1.1$ °C/s, became the cellular/dendritic transition. For $CR < 1.1$ °C/s, the microstructure was entirely dendritic. The eutectic mixture remained in the intercellular and interdendritic regions. The cellular and primary dendritic spacings of the alloys were correlated with CR by experimental power function equations

2.3.3 Quasicrystalline Al-Mn alloys

Due to the demand for highly functional lightweight materials, development of Al alloys containing amorphous, quasicrystalline phases as strengthening phases have been motivated [17–24]. Very high (104–107 K/s) cooling rates were required for the formation of quasicrystalline phases in Al alloys, of which casting of the alloys became a costly [26–33].

Recently, Stan-Głowiński et al. [34] employed intermediate cooling rates (102–103 K/s) to cast Al alloyed with low-cost elements of Mn and Fe for formation of quasicrystalline phases. They selected two alloys of 94Al–6Mn and 94Al–4Mn–2Fe (at%). The alloys were prepared by suction casting into Cu cylindrical dies, of which with height

was 35 mm and diameters were 1, 2, 3 and 4 mm. Table 2.2 gives the averaged cooling rates calculated for Cu cylindrical dies.

Fig. 2.14 presents SEM (BSE) micrographs revealing the microstructure features of the 94Al–6Mn alloy in the middles of the castings solidified in the Cu cylindrical dies with different diameters. Different rod diameters resulted in different cooling rates. The small size die led to high cooling rate. The 1-mm diameter die gave the highest cooling rate of 103 K/s. The capability of acquiring bulk quasicrystal-strengthened Al-rich alloys (94Al–6Mn and 94Al–4Mn–2Fe) was evaluated at intermediate cooling rates. SEM, TEM, X-ray diffraction and differential scanning calorimetry (DSC) were employed to understand the cooling rate effect on the quasicrystalline phase formation. The lowest cooling rate was 40 K/s which was present in the 4 mm diameter rod. The microstructure consisted of needles of the particle phase. At the highest cooling rate with 103 K/s, particles became micron plates dispatched radially. In the 2 mm and 3 mm samples with the cooling rates of 102 K/s, both needles and plate-like particles phase were observed. The plate-like morphology was also observed at the edge of the slow cooling samples. SEM pictures presented in Fig. 14 depicted the microstructures of the binary 94Al–6Mn alloy [34]. TEM micrographs (Fig. 2.15) reveal presence of crystalline hexagonal λ -Al₄Mn phase and quasicrystalline decagonal phase (D-phase) and orthorhombic L-phase. The fast cooling promoted the formation of the orthorhombic L-phase and suppressed the formation of the icosahedral quasicrystalline phase (I-phase). The formation of a quasicrystalline phase (I-phase) was promoted by the Fe introduction into the 94Al–6Mn binary alloy [34]. Fig. 2.16 presents SEM picture showing microstructure features of 94Al–4Mn–2Fe alloy. The coarse

microstructures (Fig. 2.16a, d) were present in the casting with the slowest cooling rate. The crystalline orthorhombic $\text{Al}_6(\text{Mn}, \text{Fe})$ phase was found in the alloy along with the primary Al. The SEM analysis detected a small amount of $\text{Al}_3(\text{Mn}, \text{Fe})$ phase as shown in Fig. 2.17a. The median cooling rate of 102 K/s resulted in the formation of the quasicrystalline D-phase and the orthorhombic $\text{Al}_6(\text{Mn}, \text{Fe})$ as depicted in Fig. 2.16b, e. The micron D-phase had the similar size and morphology to those found in the 94Al–6Mn binary (Fig. 2.14b). As illustrated in Fig. 2.16c, f, the fast cooling led to the excessive presence of I-phase, of which structure was identified by TEM and diffraction analyses (Fig. 2.17c, d). Fig. 2.16f shows that the fine eutectic phase encompassed the star-shaped I-phase. Jun et al. [35] investigated the formation of the I-phase in mish-metal (Mm)-containing Al94Mn6 alloy cast in Cu dies. An addition of Mm into the Al94Mn6 alloy generated icosahedral quasicrystalline phase (IQC) with an extinction of hexagonal and Al_6Mn phases, and the fraction of IQC increased continuously with an increase in Mm content. K.A.Darling et al.[36] examined the applicability of high energy mechanical alloying for producing high-strength, nanocrystalline Al8 at% Mn alloy powders and characterized the influence of Mn content on the inherent microstructure of the alloy. The solubility level (3.1 at% Mn) obtained was upto five times the equilibrium solubility limit (0.62 at%Mn) of Mn in Al. The observed microstructures were consistent with being a nanocomposite composed of an Al–Mn solid solution matrix with dispersed Mn particles. For alloys with solid solutions upto 3.1 at %, increasing the Mn content correlated with a decrease in the matrix grain size down to a minimum of 12 nm (Fig. 2.18)

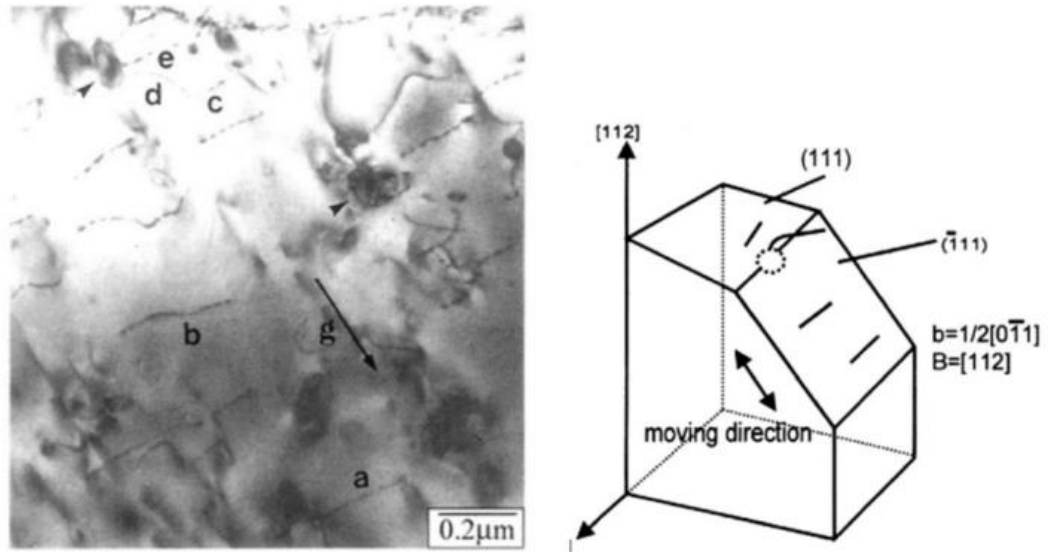


Figure 2.9 TEM micrograph showing the dislocation structure of the AA7000 series alloys containing 0.8 wt% Mn. (Arrows indicate Mn-dispersoids) [7].

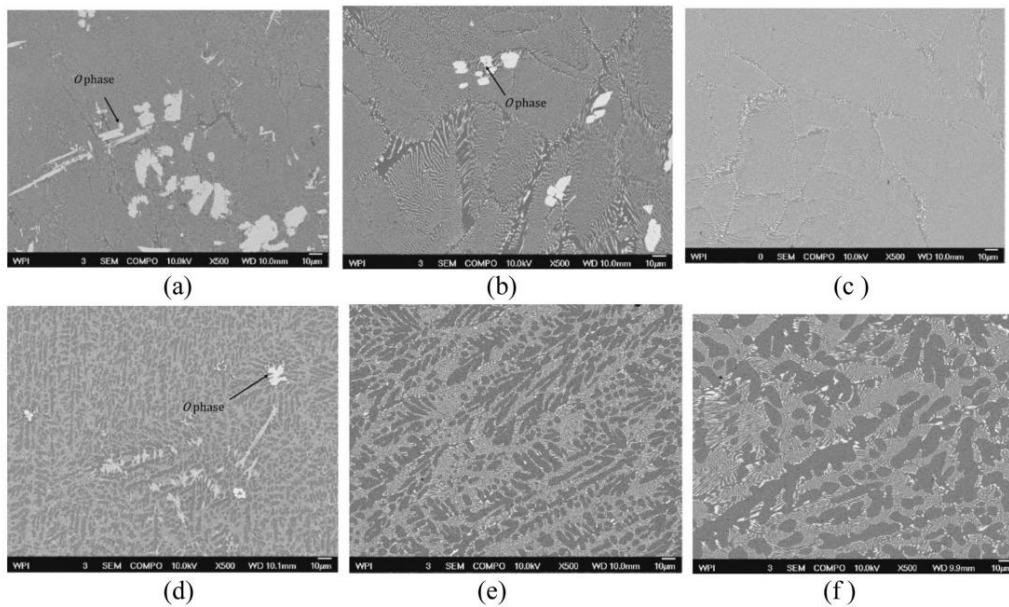


Figure 2.10 SEM photomicrographs of Al-Ni-Mn alloys cast with 90 K/s cooling rate. (a) Al-6Ni-4Mn, (b) Al-6Ni-3Mn, (c) Al-6Ni-2Mn, (d) Al-4Ni-4Mn, (e) Al-4Ni-3Mn, (f) Al-4Ni-2Mn [22]

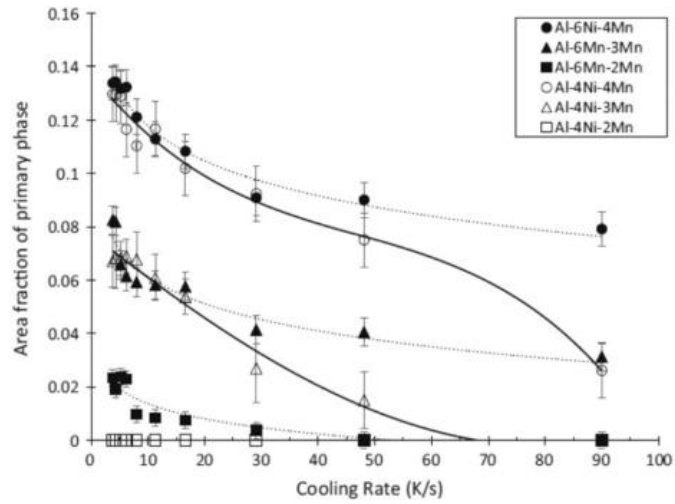


Figure 2.11 Measured area fractions of O phase as a function of cooling rate[22].

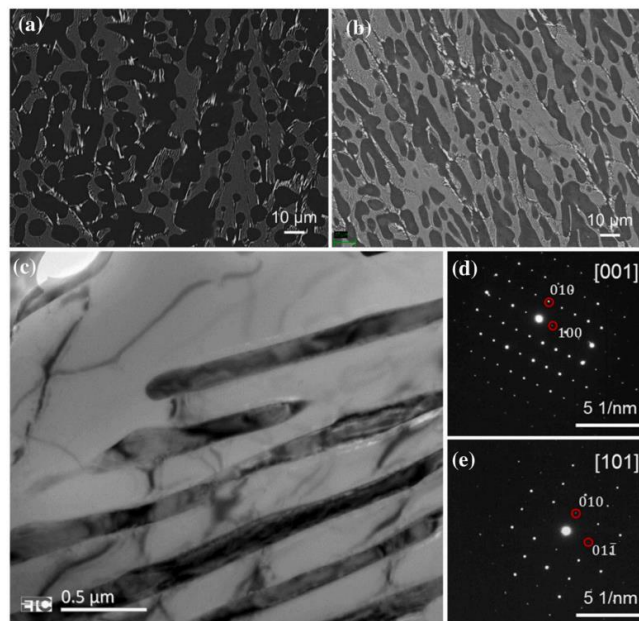


Figure 2.12 Microstructure characteristics of (a) Al-4Ni and (b) Al-4Ni-2Mn alloys illustrated by SEM pictures; (c) eutectic $\text{Al}_9(\text{Ni},\text{Mn})_2$ phase displayed by TEM picture; and diffraction patterns indexed to $\text{Al}_9(\text{Ni},\text{Mn})_2$ phase on (d) [001] and (e) [101] axis

[23]

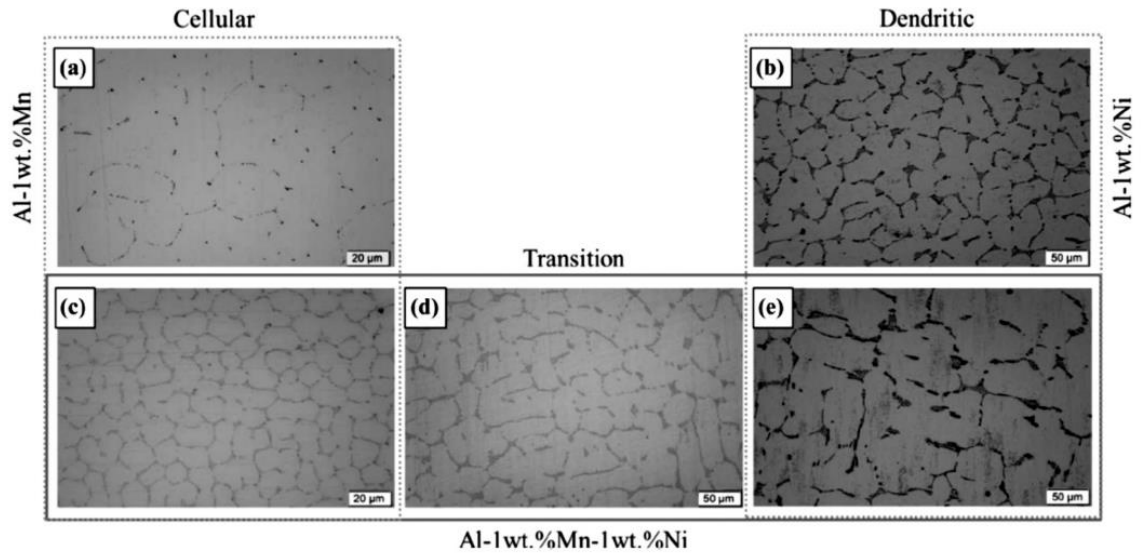


Figure 2.13 (a) cellular arrangement of the Al-1 wt% Mn alloy and (b) dendritic arrangement of the Al-1 wt% Ni alloy. Microstructural evolution of the Al-1 wt% Mn-1 wt% Ni alloy casting showing (c) cellular, (d) transition and (e) dendritic growth regimes

[25]

Table 2.2 Cooling rates of Cu cylindrical dies [34].

Cooling rates of Cu cylindrical dies [34].

| Rod diameter (mm) | 4 | 3 | 2 | 1 |
|--------------------|----------------------|-------------------------------------|-------------------------------------|-----------------------------------|
| Cooling rate (K/s) | 40 (slow cooling) | 1×10^2 (median cooling) | 1×10^2 (median cooling) | 1×10^3 (fast cooling) |

2.4 ELECTRICAL CONDUCTIVITIES OF MN-CONTAINING AL ALLOYS

The electrical conductivity of alloys is one of important properties, especially for applications of electric motors. Electrical conductivity (α) is reciprocal of electrical resistivity (γ) [18,37,38]. Matthiessen's rule [1,2,37,38] relates the conductivity and electrical resistivity to the chemical composition (ϵ) of the alloy:

$$\alpha = 1/\gamma \quad (1)$$

$$\gamma = \gamma_{\text{pure}}(T) + \sum \gamma_j \epsilon_j \quad (2)$$

where $\gamma_{\text{pure}}(T)$ is the temperature-dependent electrical resistivity of pure Al, γ_j is the electrical resistivity of specific component j in solid solution, ϵ_j is the concentration of a specific component j in solid solution [27,28].

Table 2.3 presents the change of the electrical resistivity resulting from introduction of different solutes in aluminum alloys. It can be seen from Table 2.4 that the electrical resistivity of Al alloys was affected considerably by the addition of iron and manganese. In other words, they produced the lowest effect on the electrical conductivity of Al. Among them, iron has the lowest solubility in fcc-Al, because Fe can form constitute precipitates during casting and solidification [2]. Although Al solid solution could be supersaturated by Mn, the formation of Mn containing dispersoids are often formed in Al alloys [7, 8, 2127, 35].

Miri [14] measured the electrical conductivities of as-cast three AA3xxx Al alloys with different Mn contents. Table 2.4 presents the electrical conductivities for three alloys in the as-cast and heat treatment conditions %IACS [18]. Since the contents of other alloying elements, Fe, Si and Ti were almost constant in the three alloys, their electrical

conductivities were dictated by the Mn content in Al solid solution. The lowest electrical conductivity of 29.98% IACS of Alloy 3 in the as-cast condition possessed the highest Mn level of 1.04 wt% in aluminum. Meanwhile, Alloy 1 with the lowest Mn content of 0.05 wt% in Al exhibited the highest electrical conductivity of 55.46% IACS.

Miri [18] investigated the influences of heat treatments on electrical conductivities of Mn-containing AA3xxx Al alloys by employing three different schemes of heat treatments. They were, Homogenization #1, H1, Homogenization #2, H2, and Homogenization #3, H3, of which details were given in Fig. 2.19. The results showed that during heat treatment, the dispersoids formed by migration of the Mn from Al solid solution to dispersoid particles. The electrical conductivities of the three alloys increased following the treatment. The increases in electrical conductivities of Alloy 1 and Alloy 2 were about 5% and 10%, which were limited. The application of the heat treatment to alloy 3 increased the electrical conductivity by almost 30%. This might be attributed to the fact that the Mn was highly supersaturated in solid solution of the as-cast Alloy 3. Heat treatment of Alloy 3 promoted a large amount of dispersoid formation. The difference in electrical conductivities between the different treatments for a specific alloy was insignificant.

The effect of heat treatment on the electrical conductivity of the TRC 3003 alloy was also studied by Huang [21]. The TSA annealing process significantly increased the electrical conductivity of the TRC 3003 alloy to 50% IACS from 28% IACS by about 80%, while the SSA improved the electrical conductivity by only 60%. The increase in the electrical conductivity should be attributed to fact that the applied heat treatment reduced

the Mn concentration in solid solution and increased the amount of Mn precipitated out of the solid solution.

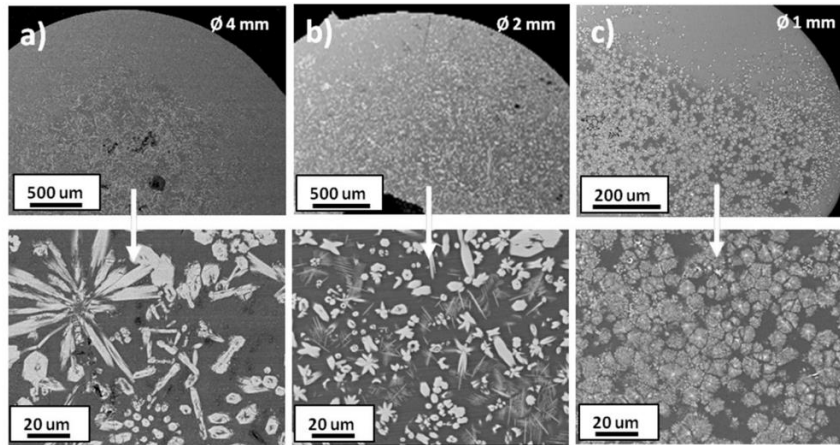


Figure 2.14 SEM pictures depicting the microstructures of the binary 94Al–6Mn alloy cast in the Cu die with the diameters of (a) Ø 4 mm,(b) Ø 2 mm, and (c) Ø 1 mm

[34]

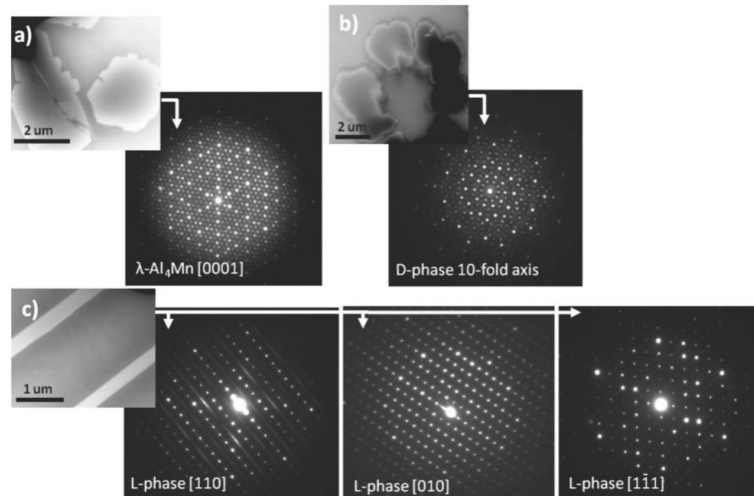


Figure 2.15 (a) hexagonal λ -Al₄Mn phase, (b) decagonal phase (D-phase) and (c) orthorhombic L-phase revealed microstructure of 94Al–6Mn by TEM pictures and electron diffraction patterns [34].

2.5 MECHANICAL PROPERTIES OF MN-CONTAINING AL ALLOYS

2.5.1 Strengthening Al alloys

The total strength (σ) of alloys can be calculated by Eq. (3) given below [1,39,40]:

$$\sigma = \sigma_0 + \sigma_{gs} + \sigma_{ss} + \sigma_{dis} + \sigma_p \quad (3)$$

where σ_0 is Peierls stress, σ_{gs} is grain boundary strengthening, σ_{ss} is solid solution strengthening, σ_{dis} is dislocation strengthening, and σ_p represents precipitation strengthening. All of these strengthening contributions lead to a degradation of the electrical conductivity, as conductive electrons are scattered by solute atoms and crystal defects. Each scattering event causes an electron to lose kinetic energy and to change its direction, thus increasing electrical resistivity or decreasing electrical conductivities.

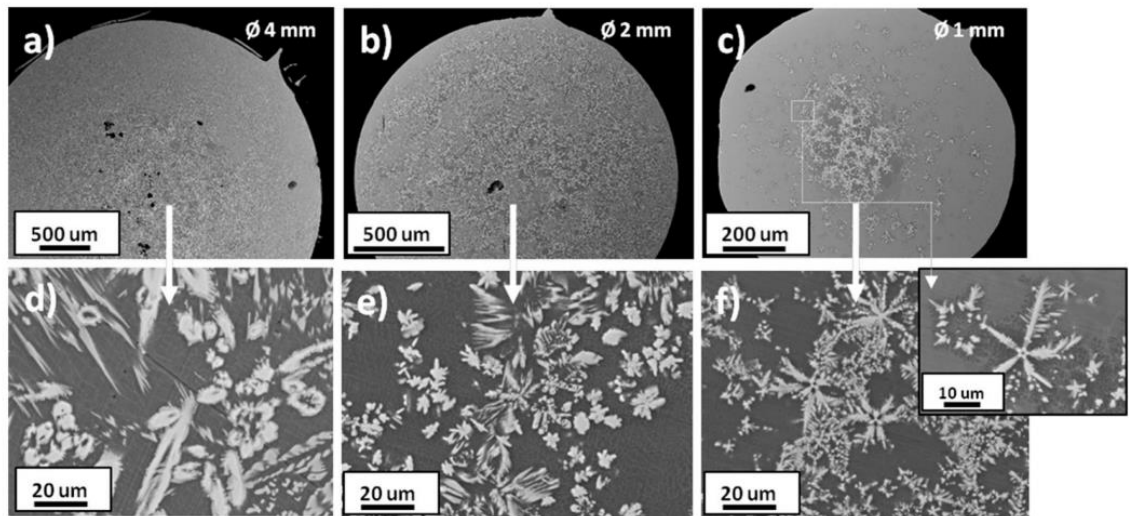


Figure 2.16 SEM pictures showing microstructures of 94Al–4Mn–2Fe alloys cast in Cu dies with the diameters of \varnothing 1–4 mm. Low magnification: a–c, and high magnification: d–f [34].

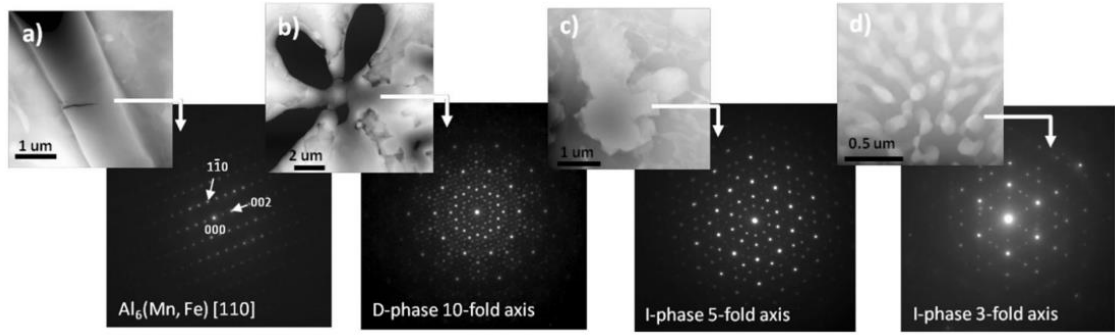


Figure 2.17 crystalline $\text{Al}_6(\text{Mn}, \text{Fe})$ phase and quasicrystalline D-phase and I-phase identified by TEM and diffraction analyses in the 94Al–4Mn–2Fe alloy [34].

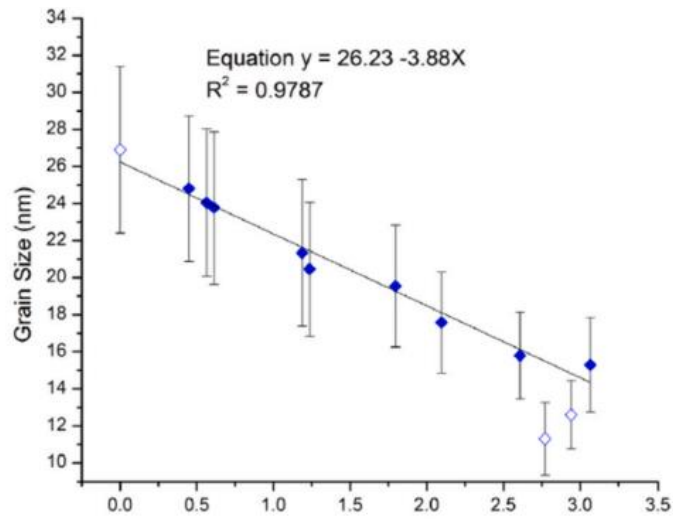


Figure 2.18 Mean grain size of the Al-rich matrix as a function of dissolved Mn content [36]

Table 2.3 Change of electrical resistivity ($\Delta\gamma$) of Al alloys with common elements and their solubilities [28].

| element | Mg | Si | Cu | Zn | Fe | Mn |
|---|------|------|------|------|-------|-------|
| $\Delta\gamma$ ($\Omega\text{m}/\text{wt}\% \times 10^9$) | 6.11 | 6.68 | 3.32 | 1.01 | 38.00 | 31.43 |
| Solubility (wt%) | 17.1 | 1.60 | 5.65 | 31.6 | 0.025 | 1.25 |

Table 2.4 Electrical conductivity for three alloys sample in as-cast and heat treatment conditions %IACS [18].

| | %IACS | | |
|---------|--------------------------|--------------------------|--------------------------|
| | Alloy 1 [0.05 wt% Mn] | Alloy 2 [0.29 wt% Mn] | Alloy 3 [1.04 wt% Mn] |
| As-cast | 55.46 | 45.30 | 29.98 |
| H1 | 57.90 | 50.27 | 40.73 |
| H2 | 58.27 | 50.68 | 41.77 |
| H3 | 58.22 | X | 40.45 |

2.5.2 Solid solutions strengthening

The solid solutions strengthening works by adding atoms of one element (the alloying element) to the crystalline lattice of another element (the base metal), forming a solid solution. This strengthening can be separated into substitutional solid solution strengthening and interstitial solid solution strengthening. Substitutional solid solution strengthening occurs when the solute atom is large enough (difference in atomic radii between the two atoms is less than about $\pm 15\%$). When the size of the solute atom less than 57% the radii of the solvent atoms can stay inside interstitial sites between the solvent

atoms, an interstitial solid solution forms. The atoms packed at the interstitial sites can result in the bonds of the solvent atoms to compress and thus deform [41].

2.5.3 Precipitation strengthening

For certain classes of alloys, heat treatment is often applied to improve their strength and hardness via precipitation hardening, in which second-phase precipitates are present as obstacles to dislocation glide. The inter-particle spacing, size, shape of precipitates, coherency of the matrix/precipitate interface, and spatial distribution of the precipitates govern the strengthening effect [42].

2.5.4 Dislocation accumulation strengthening

A dislocation is a linear or one-dimensional material defect around which some of the atoms are misaligned. Almost all metals and alloys contain some dislocations that are introduced during solidification, and as a consequence of thermal stresses that result from rapid cooling. The plastic deformation can result in dislocations to initiate from the surfaces, at stress concentrations or inside the material at defects and grain boundaries [43]. The ease with which a metal is capable of plastic deformation is a function of dislocation mobility—that is, restricting dislocation motion leads to increased hardness and strength. The large number of dislocations inside the grain and at its boundaries provides a considerable amount of strengthening in alloys, because dislocation multiplication or the formation of new dislocation hinder the motion of a dislocation. Thus, the high dislocation density enhances dislocation strengthening [44].

2.5.5 Grain boundary strengthening

Grain boundaries are barriers to dislocation movement. A metal or alloy that has small grains is stronger than one with large grains because the former has more grain boundary area and consequently more barriers to dislocation motion. The alteration of the grain size influences the number of dislocations that accumulate at the grain boundary. Based on the well-known Hall-Petch equation [45], a reduction in the grain size increases the yield strength significantly.

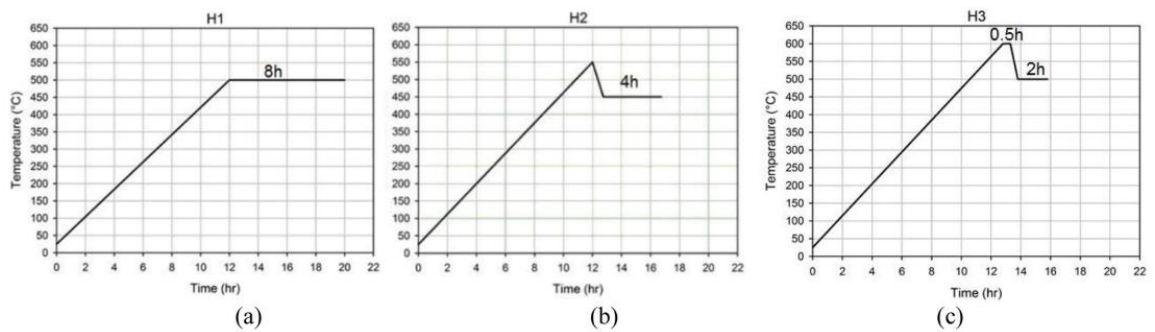


Figure 2.19 Time vs. temperature curves for heat treatments of (a) H1, (b) H2, and (c) H3 [18].

2.6 MECHANICAL PROPERTIES OF MN-CONTAINING AL ALLOYS

2.6.1 Mn-containing 3xxx and 7xxx Al alloys

To understand the hot deformation behavior of Mn-containing AA3xxx wrought Al alloys, Miri [18] performed plane strain compression (PSC) tests at the deformation strain rates of 0.1, 1.0 and 10 s⁻¹, and the deformation temperature of 300–500 °C with 100 °C temperature steps. From the stress-strain curves, the average flow stresses at the strain of 0.20 and 0.45 were calculated. Table 2.5 lists the flow stresses of Alloy 3 for strain rates of 0.1 and 10 for all three heat treatments of H1, H2 and H3 and temperatures of 300, 400 and 500 °C. Flow stresses of Alloy 2 for H1 and H2 and for the same temperatures and strain rates of 0.1 and 10 are given in Table 2.6. For Alloys 2 and 3, flow stresses for the same temperature and strain rate was similar or slightly lower for PSC specimens heat treated in H2 than those for H1. The PSC specimen of Alloy 2 treated in condition H2 showed the minimum flow stress (20.58 MPa) in the tested alloys. In one specific heat treatment, flow stress decreased as temperatures rose. Moreover, at a specific temperature, a high strain rate increased the flow stress. Alloy 3 with high Mn content exhibited higher flow stress for the same temperature and strain rate and heat treatment than those of Alloy 2 with low Mn content.

To show the Mn effect on the mechanical properties of other wrought Al alloys, AA6xxx and 7xxx series alloys were included. Nam et al. [7] investigated the influence of the Mn content on the mechanical properties of extruded AA6xxx and AA7xxxx wrought Al alloys by tensile testing with a strain rate of 4×10^{-3} s⁻¹. Fig. 2.20 presents the Mn content-dependent tensile properties of the extruded AA7xxxx wrought Al alloys with the

Mn addition varying from 0.1 to 1.2 wt% [7]. It was found that, below 0.7 wt%, the enhancement of the yield strength and ultimate tensile strength was very significant. When the Mn content became higher than 0.7 wt%, the effect of Mn on the strengths of the extruded AA7xxxx wrought Al alloys was limited. With the addition of Mn from 0.1 to 1.2 wt%, the elongation reduction of the extruded AA7xxxx wrought Al alloys was negligible. Fig. 2.21 displays the tensile properties of the Mn-containing AA6xxx series wrought Al alloys in both the extruded and T6 conditions, and compares them with the relevant properties of the commercial 6061 wrought Al alloy [7]. It can be seen from Fig. 2.21(a) that, in an extruded state, the strength of the Mn-containing alloy had higher than that of the Al 6061 with the same level of elongation. Under the T6 condition as shown in Fig. 2.21(b), the Mn-containing alloy also exhibited strengths higher than that of the T6-treated Al 6061, while the T6 treatment reduced their elongation considerably. The heat treatment increased the manufacturing cost, although the T6 treatment affected the mechanical properties of the Mn-containing AA6xxx series wrought Al alloys. The elimination of the heat treatment could reduce the production cost by 15% and increase productivity significant

Table 2.5 Flow stresses (σ_{flow}) of Alloy 3 at various strain rates [18].

| Flow stresses (σ_{flow}) of Alloy 3 at various strain rates [18]. | | | H1 | H2 | H3 |
|---|------------------------------------|---------------------------------------|------------------------------|---------------------------------|---------------------------------|
| Alloy 3 | Strain rate (s^{-1}) | Temperature ($^{\circ}\text{C}$) | σ_{flow} (MPa) | σ_{flow} (MPa) | σ_{flow} (MPa) |
| | 0.1 | 300 | 75.49 | 74.26 | 70.06 |
| | | 400 | 45.53 | 45.61 | 39.51 |
| | | 500 | 29.77 | 30.95 | 24.50 |
| | 10 | 300 | 101.59 | 101.40 | 97.00 |
| | | 400 | 72.84 | 69.94 | 66.96 |
| | | 500 | 47.97 | 47.13 | 42.93 |

Table 2.6 Flow stresses (σ_{flow}) at various strain rates for Alloy 2 [18].

| | | | H1 | H2 |
|---------|------------------------------------|---------------------------------------|------------------------------|------------------------------|
| Alloy 2 | Strain rate (s^{-1}) | Temperature ($^{\circ}\text{C}$) | σ_{flow} (MPa) | σ_{flow} (MPa) |
| | 0.1 | 300 | 60.65 | 57.84 |
| | | 400 | 34.90 | 33.68 |
| | | 500 | 21.69 | 20.58 |
| | 10 | 300 | 87.09 | 84.42 |
| | | 400 | 59.69 | 57.19 |
| | | 500 | 37.76 | 36.69 |

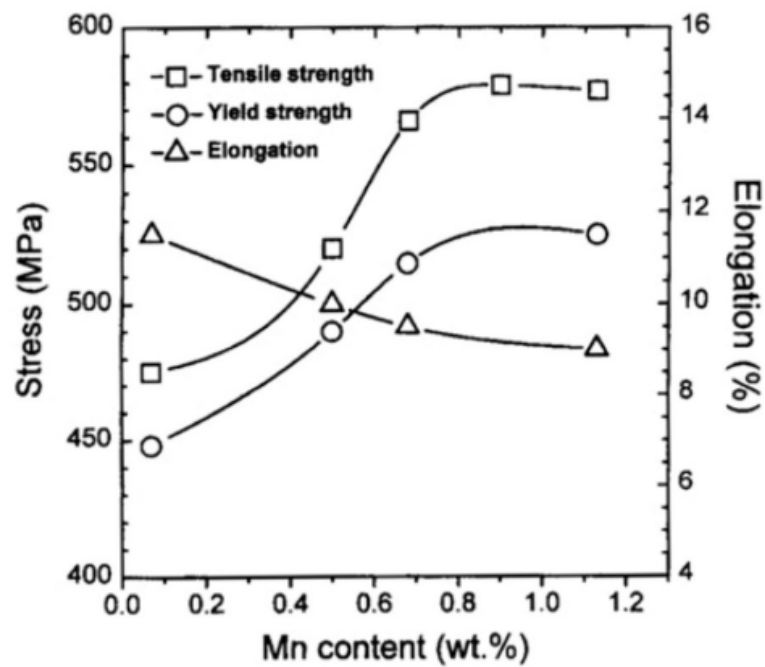


Figure 2.20 Mn content-dependent tensile properties of the extruded AA7xxx wrought Al alloys [7].

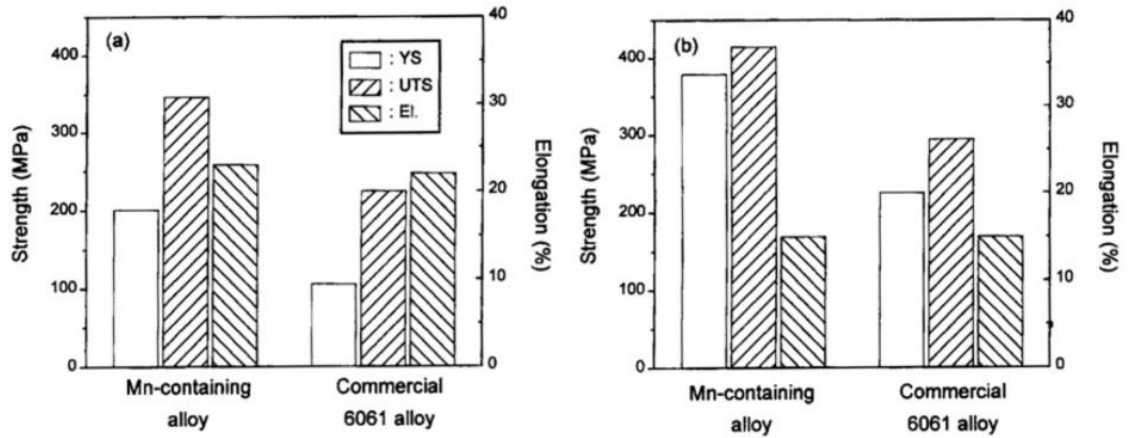


Figure 2.21 Tensile properties of Mn-containing 6000 series Al alloy and commercial 6061 Al alloy. (a) extrusion and (b) T6 heat treatment [7].

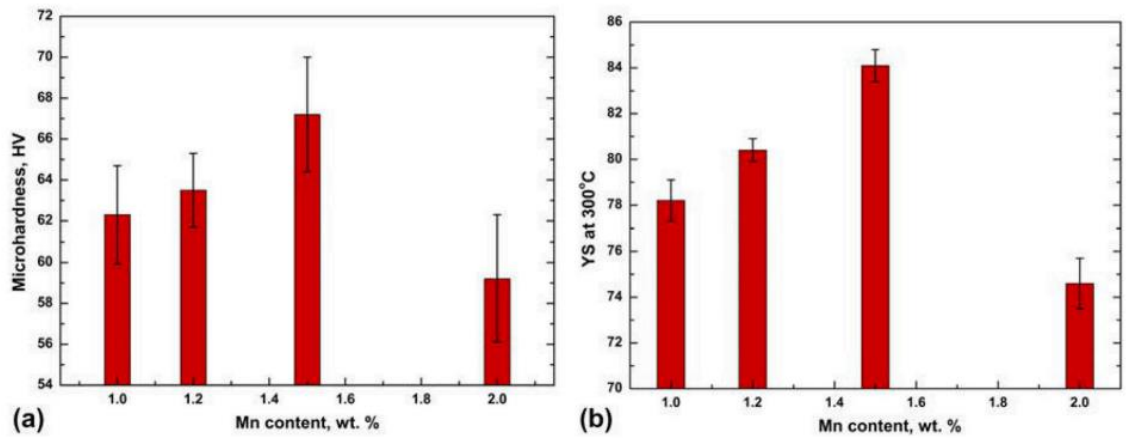


Figure 2.22 Microhardness at room temperature (a) and YS at 300 °C (b) with Mn contents [20].

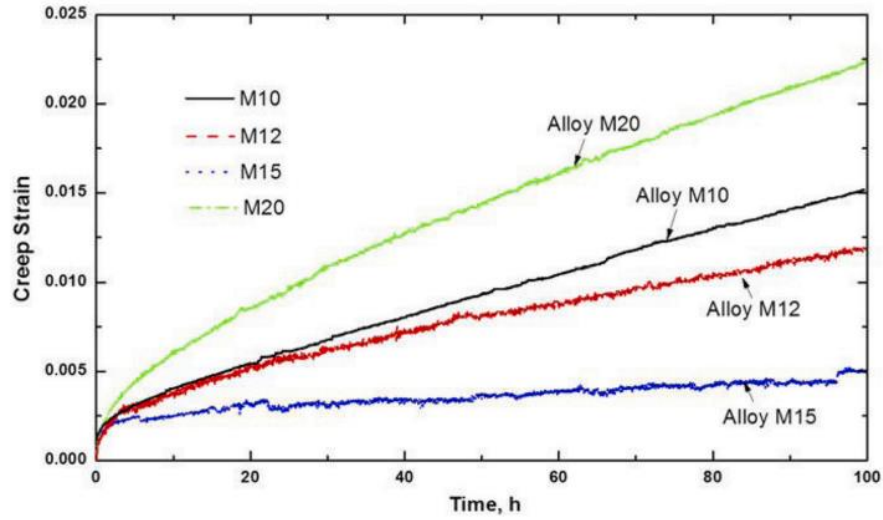


Figure 2.23 Creep curves at 300 °C of experimental alloys after 375 °C/48 h [20].

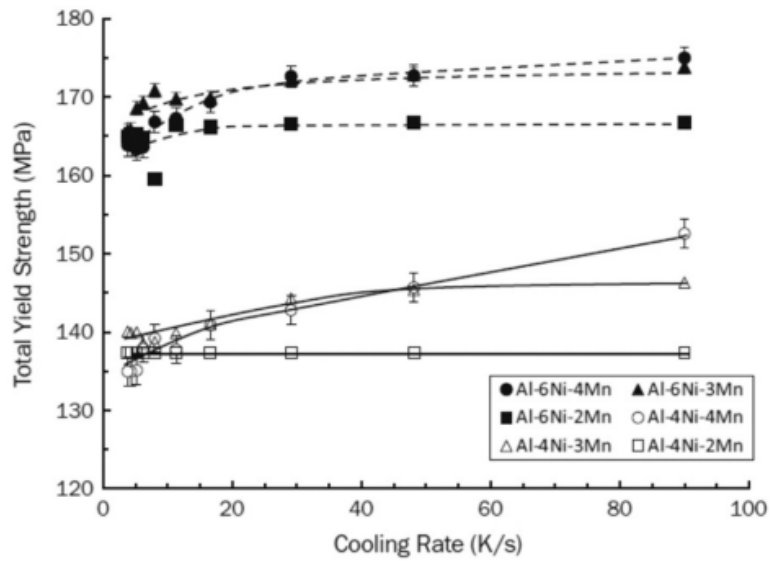


Figure 2.24 Effects of cooling rates on the yield strengths of the Al-Ni-xMn alloys prepared under different cooling rates [22]

Liu and Chen [19] applied the precipitation treatment to the permanent mold cast Al–Mn–Mg 3004 alloy. It was shown that the peak compression yield strength (YS) at 300 °C

of the alloy reached as high as 78 MPa due to a large volume fraction (~ 2.95 vol%) of α -Al(MnFe)Si dispersoids. The dispersoids were found to be thermally stable at 300 °C for up to 1000 h of holding, leading to consistently high mechanical performance and creep resistance. They also investigated the effect of Mn content on mechanical properties of the cast 3004 alloy. Their results as displayed in Figs. 2.22 and 2.23 indicated that the best combination of microhardness at room temperature, YS, and creep resistance at 300 °C obtained by heat treatment at 375 °C/48 h was obtained, as the Mn content was optimized at 1.5 wt%, due to the important contribution of dispersoid strengthening

2.6.2 Al-Ni-Mn alloys

The yield strengths (YS) of Al-Ni alloys containing 2–4 wt% Mn varying with chemical compositions and solidification cooling rates were evaluated by Fan et al. [22]. Fig. 2.15 presents the effects of cooling rates on the yield strengths of the Al-Ni-xMn alloys. Close examination of Fig. 2.24 revealed that the yield strengths of the Al-6Ni-xMn alloys were higher than those of Al-4Ni-xMn alloys. To effectively increase the yield strengths of the Al-6Ni-xMn alloys, the high Mn levels of 3 and 4 wt% were needed, as the cooling rate was > 30 K/s for Al-6Ni-xMn alloys, and > 50 K/s for Al-4Ni-xMn alloys. At the Mn level of 2 wt%, the cooling rate had little effect on the yield strengths of both Al-6Ni-xMn and Al-4Ni-xMn alloys [22]. The study by Fang [23] showed that, at the room temperature of 25 °C and the elevated temperature of 250 °C, the tensile and yield strengths as well as the hardness of Al-4Ni alloy were enhanced by Mn as depicted in Fig. 2.25. The Al-4Ni alloy presented hardness of 42.3 HV10, while the Al-4Ni-2Mn alloy showed a 53% increase to 64.5 HV10. When the Mn level was further increased to 3.01 wt% and 3.77

wt%, the hardness increased to 67.2 HV10 and 69.9 HV10, respectively, as shown in Fig. 2.25a. The yield strength at 25 °C increased from 48 MPa to 92 MPa with 1.87 wt% Mn and then to 117 MPa with 3.77 wt% Mn (Fig. 2.25b). At 250 °C, the yield strength increased from 35 MPa to 82 MPa with 1.87% Mn and then to 101 MPa with 3.77% Mn (Fig. 2.25c).

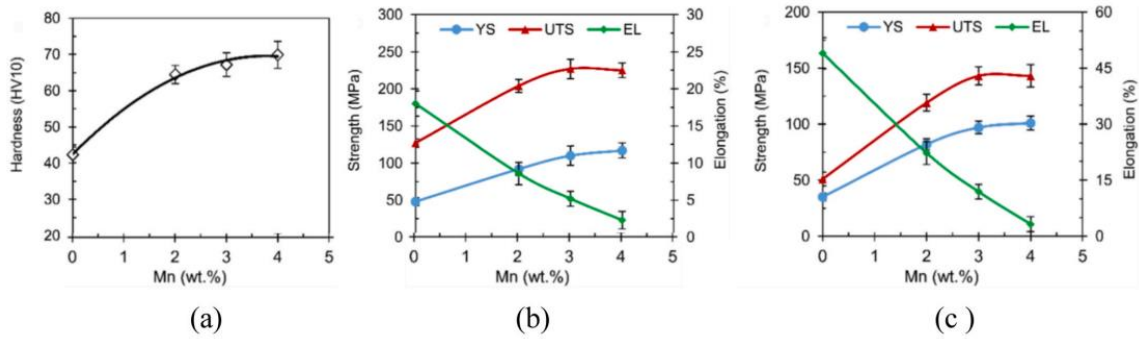


Figure 2.25 Mn influence on (a) hardness, and YS and UTS and elongation (EL) of the Al-4Ni alloy at (b) 25 °C and (c) 250 °C [23].

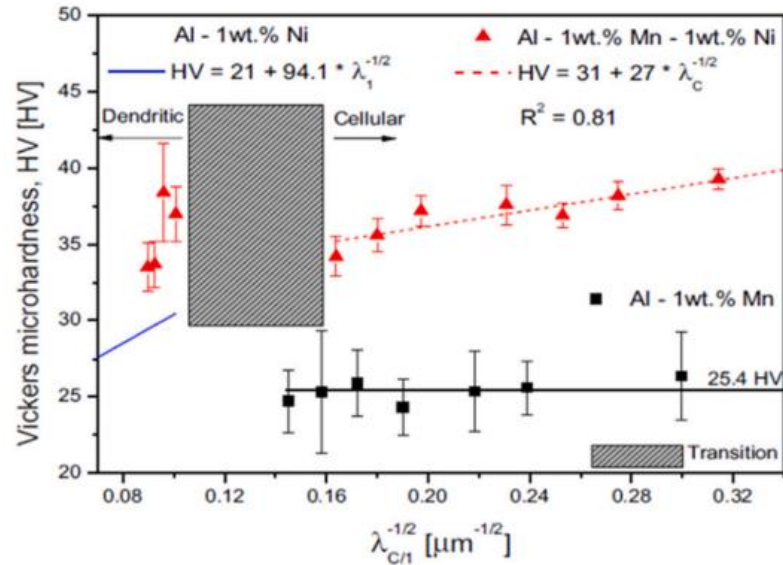


Figure 2.26 Vickers microhardness of the Al-1 wt% Mn and Al-1 wt% Mn-1 wt% Ni cast alloys as a function of the cellular (λ_C) and primary dendritic (λ_1) spacings ($\lambda_C/1-1/2$), and R^2 is the coefficient of determination [25]

The ultimate tensile strength (UTS) rose from 123 MPa for the Al4Ni alloy to 202 MPa for the Al-4Ni-2Mn alloy, and then to 223 MPa as the Mn level reached 3.77 wt% at 25 °C (Fig. 2,25b). The UTS increased from 51 MPa for the Al-4Ni alloy to 120 MPa for the Al-4Ni-2Mn alloy, further to 223 MPa as the Mn level reached 3.77 wt% at 250 °C (Fig. 2,25c).

Based on strengthening mechanisms as discussed in the preceding section, it was almost impossible for Ni with an ultra low solubility (0.05 wt% at 640 °C) of Ni in Al matrix to generate solid solution strengthening. However, Mn had a solubility of 1.25 wt% at 658 °C and an atomic radius of 1.40 Å larger than that (1.25 Å) of Al. In the Al-Mn solid solution, the atomic lattice distortion impeded dislocation movement during plastic

deformation for high strengths. Also, the high level of Mn boosted the amount of eutectic phases and primary intermetallic phases. The Al-4Ni alloy contained 44 vol% of eutectic phases. With 1.87 wt% Mn addition, the eutectic phases increased to 51 vol%, while no primary intermetallic phase was found. With 3.01 wt% Mn addition, the eutectic phases increased to 58 vol%, and the primary intermetallic phase was found at a level of 1 vol%. When the Mn content was increased to 3.77 wt %, the eutectic phases increased to 60 vol% and the primary intermetallic phase increased to 5 vol%. The high content of the eutectic phases and primary intermetallic phases induced secondary-phase strengthening. The alloys with Mn exhibited less strength loss than Al-4Ni alloy at 250 °C. The eutectic $\text{Al}_9(\text{Ni,Mn})_2$ phase showed good thermal stability. No coarsening was observed after 2000 h at 250 °C.

Oliveira [25] reported the relation between the microstructure and the mechanical properties of Al-Mn binary and Al-Mn-Ni ternary alloys in the as-cast condition. A Hall-Petch-type equation was established relating the Vickers microhardness (HV) of the Al-1 wt% Mn and Al-1 wt% Mn-1 wt% Ni alloys to their cellular (λ_C) and primary dendritic (λ_1) for the alloys as shown in Fig. 2.26.

Darling et al. [36] investigated the microhardness of mechanically alloyed Al-8 at%Mn alloys prepared by ball milling. A Hall-Petch plot for the Al-rich matrix grain size as a function of milling time, showing the linear increased in hardness with decreasing Al grain size. The plot included hardness values for both the pre-milled and non-pre-milled Al as well as literature data for pure Al. There was a change in the Hall-Petch slope at a grain size of 25 nm (around $0.2 \text{ nm}^{-1/2}$), which was attained after 5-10 h of milling. Also, for

the alloys with up to 3.1 at% Mn in solid solution, increasing the Mn content correlated with a decrease in the matrix grain size down to a minimum of 12 nm ($0.29 \text{ nm}^{-1/2}$). A high hardness values of 4 GPa was obtained. Fig. 2.27.

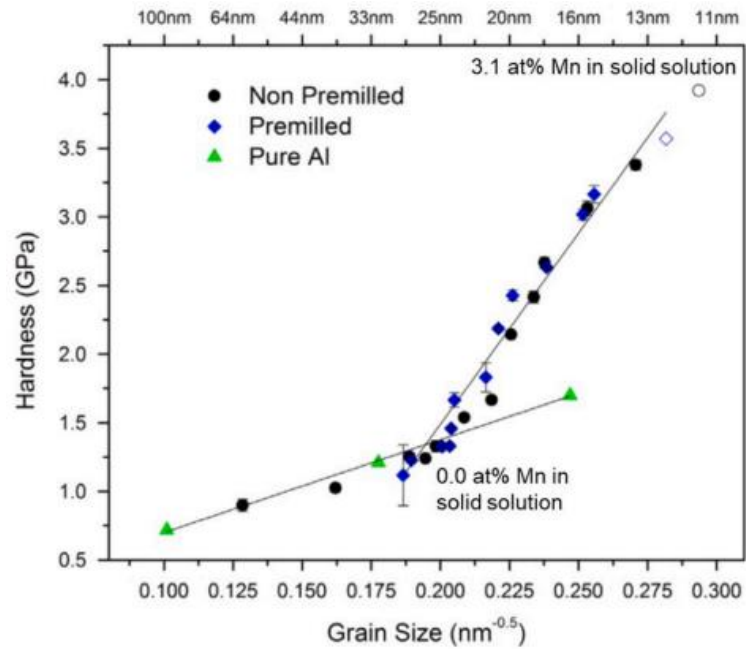


Figure 2.27 Hall-Petch grain size dependence of the pre- and unmilled Al samples, and pure nanocrystalline Al for comparison [36]

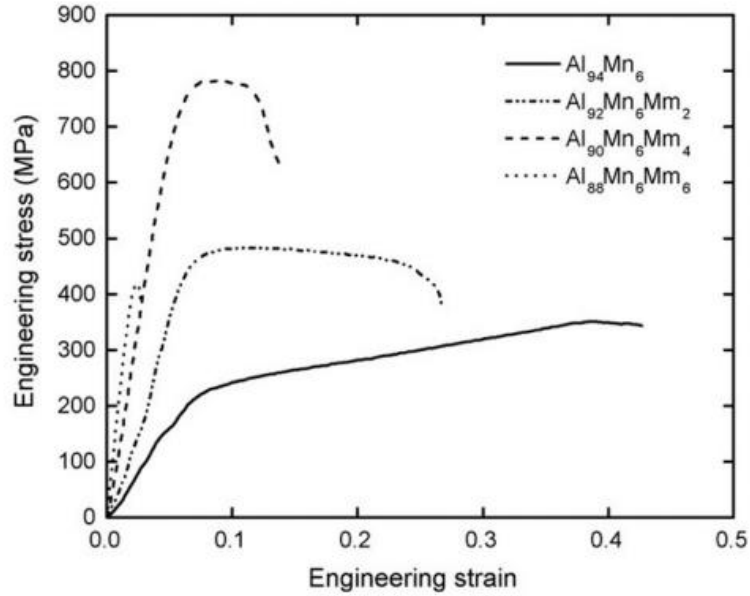


Figure 2.28 Compressive engineering stress–strain curves at room temperature for Al-Mn-Mm alloys [26].

Mraied and Cai [46] studied the effects of Mn alloying on the tribocorrosion behavior of magnetron-sputtered Al-Mn thin films with 5.2 at% and 20.5 at% Mn in a 0.6 M NaCl aqueous solution. Tribocorrosion resistance was found to be strongly affected by the alloying concentration and applied potential. Higher Mn content increased the ratio of hardness to elastic modulus(H/E) and promoted the formation of denser and more compact passive film, consequently, improving tribocorrosion resistance of Al. In particular, alloying with 20.5 at% Mn led to an increase of the corrosion resistance by about 10 times and the hardness by around 8 times compared to pure Al.

2.6.3 Quasicrystalline Al-Mn alloys

Jun et al. [26] evaluated tensile properties of quasicrystal Al-MnMm alloys with compression tests. The compressive engineering stress–strain curves of the Al Mn Mm

alloys obtained at room temperature and under a constant crosshead speed of 1 mm/min, are given in Fig. 2,28. Compressive yield strength (σ_{cys}) and ultimate compressive strength (σ_{ucs}) of the Al-Mn-Mm alloys were improved remarkably with Mm content up to 4%, while elongation was steeply deteriorated by the Mm addition. The change in σ_{cys} and σ_{ucs} with Mm content might well be closely associated with the microstructural evolution (increased quantity of IQC with finer morphology).

2.7 *Summary*

Al alloys has a great potential for engineering applications employed in the battery-powered electric vehicles as well as in the electric power industry. Mn as a transition metallic alloying element can enhance mechanical properties of Al alloys prepared by either wrought or casting processes without sacrificing high electrical conductivities of aluminum required by electric motor applications in the BEV and EPI. This is because Mn is capable of generating second phase or precipitation strengthening with Al and has a relatively low maximum solubility in Al solid solution. When the low contents of Mn (0.05–1.20 wt%) were introduced into the conventional wrought 3xxx and 7xxx Al alloys, their YS and UTS increased by about 50%. The added manganese formed a manganese dispersoid of Al₆Mn and/or Al₃Mn, which had an incoherent structural relationship with respect to the FCC matrix in retarding the motion of dislocations that increased strengths. With the increased levels (2–4 wt%) of Mn, the yield strengths of cast Al-Ni alloys increased by two times at 25 °C and three times at 250 °C. This increase resulted from transformation of the eutectic phase from Al₃Ni/ α -Al to Al₉(Ni, Mn)₂/ α -Al. As extremely high cooling rates (10⁴–10⁷ K/s) were applied, cast Mn containing Al alloys with the high level (4 and 6 wt%) of Mn addition developed quasicrystalline phases as strengthening phases. As a result, the Mn-containing Al alloys with misch metal exhibited around 800 MPa in ultimate compressive strength.

Studies on electrical properties of Mn-containing Al alloys are scarce. But, Mn addition affected the electrical conductivity of Al alloys. It has been shown that the low amount (0.05 wt%) of Mn had little effect on the electrical conductivity of the as-cast 3xxx

Al alloy. As Mn addition increased to 1.04 wt%, the electrical conductivity of the as-cast 3xxx Al alloy reduced less than 30% IACS, which is unacceptable for the BEV and EPI applications. Although heat treatment could increase the electrical conductivities, additional manufacturing steps make components costly. To satisfy the engineering requirement for electric motor applications, the level of Mn addition in Al alloys should be limited to maintain high electrical conductivities. Meanwhile, high cooling rates need to be applied during casting, which can generate high mechanical properties. The combination of low Mn contents and high cooling rates in casting could make the advent of cost-effective Mn-containing Al alloys in the BEVs and EPI feasible.

2.8 REFERENCES

- [1] Y. Li, A. Hu, Y. Fu, S. Liu, W. Shen, H. Hu, X. Nie, Al alloys and casting processes for induction motor applications in battery-powered electric vehicles: a review, *Metals* Vol.12 (2022) p216.
- [2] S. Liu, A. Hu, H. Hu, X. Nie, N.C. Kar, Potential Al-Fe cast alloys for motor applications in electric vehicles: an overview, *Key Eng. Mater.* Vol923 (2022) p3–p19.
- [3] M.Y. Murashkin, I. Sabirov, X. Sauvage, R.Z. Valiev, Nanostructured Al and Cu alloys with superior strength and electrical conductivity, *J. Mater. Sci.* Vol51 (1) (2016) p33–p49.
- [4] Y. Li, Y. Fu, A. Hu, X. Nie, H. Hu, Effect of Sr and Ni Addition on Microstructure, Tensile Behavior and Electrical Conductivity of Squeeze Cast Al-6Si-3Cu Al Alloy, *Key Eng. Mater.* Vol921 (2022) p3–p14.
- [5] H. Ishikawa, Y. Takashima, Y. Okada, Squirrel-Cage motor Rotor and Squirrel-Cage Motor. U.S. Patent No. 9,935,533, 4, 2018.
- [6] P. Sivanesh, K. Charlie, S.J. Robert, F. Ethan, E. Paul, Aluminum Alloys for Die Casting. U.S. Patent No. WO 2020/028730 A1, 2020.
- [7] S.W. Nam, D.H. Lee, Eff. Mn Mech. Behav. Al Alloy. - *Met. Mater. Int.* Vol. 6 (No. 1) (2000) p13–p16.
- [8] J. Davis, *ASM Specialty Handbook: Aluminum and Aluminum Alloys*; ASM International: Materials Park, OH, USA, 2002.
- [9] M. Hassanipour, M. Diago, D. Valiquette, F. Guay, A. Leblond, Characterization of aluminum conductors, steel reinforced in overhead transmission lines, in: S. Broek (Ed.),

Light Metals 2023, The Minerals, Metals & Materials Society, 2023, , https://doi.org/10.1007/978-3-031-22532-1_49, pp 355-359

[10] D. Beaulieu, Characteristics of Structural Aluminum; Presses de l'aluminium: Chicoutimi, QC, Canada, 2005.

[11] T. Bubonyi, P. Barkoczy. Evaluation of Eutectic Structure in Aluminum Alloys. DOI:10.26649/musci.2019.073, MultiScience - XXXIII. microCAD International Multidisciplinary Scientific Conference, University of Miskolc, Borsod-Abaúj-Zemplén, Hungary, 23–24 May, 2019.

[12] A.J. McAlister, J.L. Murray, The (Al-Mn) aluminum-manganese system - journal of phase equilibria, Bull. Alloy Phase Diagr. Vol. 8 (No. 5) (1987).

[13] R.J. Schaefer, L.A. Bendersky, D. Shechtman, W.J. Boettinger, F.S. Biancaniello, Icosahedral and Decagonal Phase Formation in Al-Mn Alloys, Metall. Trans. A Vol. 17 (1986) p2117–p2125.

[14] B. Grushko, D. Pavlyuchkov, S.B. Mi, S. Balanetsky, Ternary phases forming adjacent to Al₃Mn-Al₄Mn in Al-Mn-TM (TM = Fe, Co, Ni, Cu, Zn, Pd), J. Alloy. Compd. Vol. 677 (2016) 148–162.

[15] S. Balanetsky, G. Meisterernst, M. Feuerbacher, The Al-rich region of the Al–Mn–Ni alloy system. Part I: Ternary phases at 750–950 °C, J. Alloy. Compd. Vol. 509 (2011) 3787–3794. [16] S. Balanetsky, G. Meisterernst, B. Grushko, M. Feuerbacher, The Al-rich region of the Al–Mn–Ni alloy system. Part II. Phase equilibria at 620–1000 °C, J. Alloy. Compd. Vol. 509 (2011) 3795–3805.

[17] Mario J. Alexander Walnsch, Martin Kriegel, Mykhaylo Rudolph, Olga Motylenko, Andreas Fabrichnaya, Leineweber, Thermodynamic assessment and experimental investigation of the Al–Mn–Ni system, *Calphad* Vol. 64 (2019) 78–89.

[18] R.M. Miri, Effect of Manganese (Mn) Content and Homogenization Treatment on Hot Deformation of AA3xxx Aluminum Alloys, Master Thesis, University of Waterloo, Waterloo, Ontario, Canada, 2016.

[19] K. Liu, X.-G. Chen, Development of Al-Mn-Mg 3004 alloy for applications at elevated temperature via dispersoid strengthening, *Mater. Des.* Vol. 84 (2015) 340–350.

[20] K. Liu, X.-G. Chen, Evolution of microstructure and elevated temperature properties with Mn addition in Al-Mn-Mg alloys, *J. Mater. Res.* Vol 32 (2017) 2585–2593.

[21] Li Huang, Guangjie Huang, Lingfei Cao, Xiaodong Wu, Zhihong Jia, Mingyong Xia, Qing Liu, Influence of pre-recovery on the subsequent recrystallization and mechanical properties of a twin-roll cast Al-Mn alloy, *Mater. Sci. Eng. A* Vol. 682 (2017) 63–72.

[22] Y. Fan, K. Huang, M.M. Makhlof, Precipitation Strengthening in Al-Ni-Mn Alloys, *Metall. Mater. Trans. A.* Vol46 (2015) p5830–p5841.

[23] J. Fang, X. Dong, S. Ji, Effect of Mn on microstructure and mechanical properties of Al-4Ni Alloy, *JOM* Vol. 73 (No. 12) (2021) p3819–p3826.

[24] Qitang Wentao Yu, Li Hao, Jiehua Fan, Li, Eutectic solidification microstructure of an Al-4Ni-2Mn alloy, *J. Alloy. Compd.* Vol. 688 (2016) 798–803.

[25] Ricardo Oliveira, Rafael Kakitani, Lucas R. Ramos, Danilo L. Gonçalves, Amauri Garcia, Noé Cheung, The Roles of Mn and Ni Additions to Fe-Contaminated Al in

Neutralizing Fe and Stabilizing the Cellular α -Al Microstructure, *J. Sustain. Metall* Vol. 5 (2019) 561–580.

[26] A. Inoue, F. Kong, S. Zhu, C. Liu, Al-Marzoukic F. (2015) Development and applications of highly functional Al-based materials by use of metastable phases. *Mater Res* 18:1414–1425 *J Mater Sci* Vol52 (2017), p7794–p7807 7805.

[27] A. Inoue, A. Kimura, Sh Yamaura, Production and mechanical properties of aluminum alloys with dispersed nanoscale quasicrystalline and amorphous particles, *Met. Mater. Int* Vol.9 (2003) p527–p536.

[28] T.J. Watson, M.A. Gordillo, I. Cernatescu, M. Aindow, Structure and mechanical properties in a powder-processed icosahedral-phase-strengthened aluminum alloy, *Scr. Mater.* Vol.123 (2016) p51–p54.

[29] K. Stan-Głowinska, L. Litynska-Dobrzynska, J. Morgiel, A. Goral, M.A. Gordillo, J.M. Wiezorek, Enhanced thermal stability of a quasicrystalline phase in rapidly solidified Al–Mn–Fe–X alloys, *J. Alloy Compd.* Vol. 702 (2017) p216–p228.

[30] J.A. Juarez-Islas, D.H. Warrington, H. Jones, Formation of stable and metastable phases in Al–Mn alloys by the use of a gravity chill casting technique, *J. Mater. Sci.* Vol.24 (1998) p2076–p2080.

[31] R.D. Field, H.L. Fraser, Precipitates possessing icosahedral symmetry in a rapidly solidified Al–Mn alloy, *Mater. Sci. Eng.* Vol. 68 (1998) L17–L21.

[32] K. Kimura, T. Hashimoto, K. Suzuki, K. Nagayama, H. Ino, S. Takeuchi, Structure and stability of quasicrystalline Al–Mn alloys, *J. Phys. Soc. Jpn* Vol. 55 (1986) 534–543.

[33] A. Inoue, L. Arnberg, B. Lehtinen, M. Oguchi, T. Masumoto, Compositional analysis of the icosahedral phase in rapidly quenched Al–Mn and Al–V Alloys, *Met. Trans. A* Vol. 17A (1986) p1657–1661.

[34] K. Stan-Głowiński, A. Rogal, Lukasz, Góral, A. Wierzbicka-Miernik, J. WojewodaBudka, N. Schell, L. Lityńska-Dobrzyńska, Formation of a quasicrystalline phase in Al–Mn base alloys cast at intermediate cooling rates, *J. Mater. Sci.* Vol. 52 (2017) p7794–p7807.

[35] J.H. Jun, J.M. Kim, K.T. Kim, W.J. Jung, Fabrication and mechanical properties of quasicrystal-reinforced Al–Mn–Mm alloys, *Mater. Sci. Eng. A* Vol. 449–451 (2007) p979–p982.

[36] K.A. Darling, A.J. Roberts, L. Armstrong, D. Kapoor, M.A. Tschopp, L.J. Kecskes, S.N. Mathaudhu, Influence of Mn solute content on grain size reduction and improved strength in mechanically alloyed Al-Mn alloys, *Mater. Sci. Eng. A* Vol. 589 (2014) 57–65.

[37] B. Raeisinia, W.J. Poole, D.J. Lloyd, "Examination of precipitation in the aluminium alloy AA6111 using electrical resistivity measurement," *Mater. Sci. Eng.* Vol. 420 (2006) p245–p249.

[38] P.L. Rossiter, *The Electrical Resistivity of Metals and Alloys*, Cambridge university press., Cambridge, 1987.

[39] N. Kamikawa, X. Huang, N. Tsuji, N. Hansen, Strengthening mechanisms in nanostructured high-purity aluminium deformed to high strain and annealed, *Acta Mater.* Vol. 57 (2009) p4198–p4208.

[40] H. Asgharzadeh, A. Simchi, H.S. Kim, Microstructural features, texture and strengthening mechanisms of nanostructured AA6063 alloy processed by powder metallurgy, *Mater. Sci. Eng. A* Vol. 528 (2011) p3981–p3989.

[41] W. Soboyejo, *Mechanical Properties of Engineered Materials* Vol. 152 CRC Press., Boca Raton, FL, USA, 2002.

[42] A. Kelly, R.B. Nicholson (Eds.), *Strengthening Methods in Crystals*, Elsevier, UK, 1971.

[43] M.F. Ashby, The deformation of plastically non-homogeneous materials, *Philos. Mag.* Vol. 21 (1970) p399–p424.

[44] M.Y. Murashkin, I. Sabirov, X. Sauvage, R.Z. Valiev, Nanostructured Al and Cu alloys with superior strength and electrical conductivity, *J. Mater. Sci.* Vol. 51 (2016) p33–p49.

[45] E.O. Hall, The deformation and aging of mild steel. *Proc. Phys. Soc. B.* Vol. 64, 1951: p747–p753.

[46] Hesham Mraied, Wenjun Cai, The effects of Mn concentration on the tribocorrosion resistance of Al–Mn alloys, *Wear* Vol 380–381 (2017) 191–202

Chapter 3: Nano Phase-containing Al-0.3Mn Alloy for Potential EV Applications: Microstructure, Tensile Behavior and Electrical Conductivity

3.1 1. INTRODUCTION

To reduce greenhouse gas emissions, battery-powered electric vehicles (BEVs) are gaining the popularity in the auto community. For further expansion of the BEV market, development of inexpensive, lightweight, highly efficient induction motors becomes an urgent task the automotive industry to, since the current BEVs are considerably heavier than those gasoline-powered vehicles (GPVs). In induction motors, squirrel cage rotors play a key role in electromechanical energy conversion [1-3]. At present, pure Al as a substitute for copper is used for production of rotor bars in induction motors by casting because of its high electrical conductivity, lightweight and low price. Unfortunately, the tensile properties including the ultimate tensile strength (UTS) and yield strength (YS) of the pure aluminum are very low. The engineering performance assurance of Al rotor bars requires a large cooling system to be placed in the induction motor. The installation of the cooling system enlarges the size and makes the induction motor much heavy, and consequently increases the BEV weight [1]. A reduction in the BEV weight becomes essential for low battery energy consumption and long driving range [3].

The employment of conventional Al casting alloys for the rotor bar could eliminate the large cooling system and reduce the motor weight. However, commercially available Al casting alloys containing Si, Mg and Cu exhibit low

electrical conductivities around 30 %IACS, because they have high solubilities in aluminum solid solution [4-11]. Manganese as a low-cost transition metal has a multifaceted array of industrial alloy uses in ferrous alloys-steels and cast iron, which can improve their strength, workability, and wear resistance. The 3xxx series of wrought Al alloys employs Mn as a major alloying element, and are used for applications, in which moderate strength combined with high ductility and excellent corrosion resistance is required. With low weight percent of Mn addition, the YS and UTS of Al alloys increase without sacrificing ductility, as Mn in aluminum-rich alloys forms a manganese dispersoid of Al_6Mn , which blocks the dislocation and changes the slip system by means of cross-slip [7]. Compared to common alloying elements, Si, Cu and Mg, Mn has a low solubility in pure aluminum, which could minimize the reduction in electrical conductivity. The maximum solubility of Mn is 1.25 wt% at 658 °C [7, 8]. As a result, low Mn addition enables the development of low-cost Al alloys with not only high strengths but also high electrical conductivities, which are required for applications in BEVs. However, simultaneous studies on microstructure, tensile behavior and electrical conductivities of castable Al-Mn alloys are scarce.

In the present study, an Al-0.3Mn alloy and HP Al (99.9%) were cast in a permanent steel mold (PSMC) to produce rectangular casting plates. The mechanical properties and the electrical conductivities of the prepared castings were evaluated. The preliminary microstructure analyses of the PSMC Al-0.3Mn alloy and HP Al was carried out. printer.

3.2 2. EXPERIMENTAL PROCEDURE

3.2.1 2.1. Materials and Casting

The Al-0.3Mn alloy with the chemical composition in Table 3.1 was selected for investigation. High purity (HP) Al (99.9%) was also used for the purpose of comparison, of which composition is given in Table 3.1. In each casting run, about 1 kg of the alloy melt was prepared in an electric resistance furnace using a graphite crucible. The melt was held at $750\text{ }^{\circ}\text{C}\pm 10\text{ }^{\circ}\text{C}$ for about 20 min, stirred for 10 minute to homogenize its chemical composition, and then poured into a permanent steel mold to produce a rectangular casting plate with the dimensions of $150\text{ mm} \times 125\text{ mm} \times 10\text{ mm}$.

Table 3.1 Chemical compositions of Al-0.3Mn alloy and high purity (HP) Al

| Materials | chemical composition (wt%) | | | | | | | |
|-----------|----------------------------|-------|-------|--------|-------|-------|--------|--------|
| | Mn | Fe | Si | Cu | Zn | C | Al | Others |
| Al-0.3Mn | 0.30 | 0.034 | 0.062 | <0.002 | <0.01 | <0.01 | remain | None |
| HP Al | - | 0.030 | 0.060 | - | 0.001 | <0.01 | 99.9% | 0.13 |

3.2.2 2.2. Porosity Measurement

Porosity was quantitatively determined by density measurements. Based on the weight measurement of both the permanent steel mold cast (PSMC) Al-0.3Mn and PSMC HP Al specimens in air and water, the actual density (D_a) of each specimen was determined using Archimedes principle based on ASTM Standard D3800 [12]

$$D_a = \frac{D_w W_a}{W_a - W_w} \quad (\text{Eq 1})$$

where W_a and W_w are the weight of the specimen in the air and in the water, respectively, and D_w the density of water. The porosity of each specimen was calculated by the following equation. The porosity of each specimen was calculated by the density values through the following equation (ASTM C948) [13]

$$\% \text{ Porosity} = \left[\frac{D_t - D_a}{D_t} \right] \times 100\% \quad (\text{Eq 2})$$

where D_t is the theoretical densities of the pure Al, with the density of 2.70 g/cm³ [9], and the Al-0.3Mn alloy calculated based on the weight percentages of Al (2.70 g/cm³) and Mn (7.43 g/cm³), with the density of 2.72 g/cm³.

3.2.3 2.3. Microstructure Analysis

Metallographic samples were cut from the center of cast specimens. The standard mounting and polishing procedure were applied to the cut metallographic samples subsequently before the observation. The detailed features of the microstructure were characterized by a scanning electron microscope (SEM), HitachiTM Tabletop Microscope TM3000 (Tokyo, Japan), with a maximum resolution of 30 nm in a backscattered mode/1 μm in x-ray diffraction mapping mode, and useful magnification of 10 to 10,000. maximize composition reading of the energy dispersive spectroscopy (EDS) data. Quantitative evaluation of specimen microstructures consisted of calculating area fractions of different phase constituents and porosity. This procedure was completed with ImageJ, a public domain image processing system [14].

3.2.4 Tensile Testing

The mechanical properties of both the PSMC Al-0.3Mn and PSMC HP Al specimens were evaluated by the tensile testing, which was carried out at ambient temperature on a MTS Criterion (Model 43) Tensile Test Machine (Eden Prairie, MN, USA) equipped with a data acquisition system. According to ASTM B557 [15], subsize flat tensile specimens (0.025 m in gage length, 0.006 m in width, and 0.010 m in as-cast thickness) were machined from the sectioned coupons. The strain rate during tensile testing was 0.5 mm/min with a sampling rate of 10 Hz. The tensile properties, including 0.2% yield strength (YS), ultimate tensile strength (UTS), elongation to failure (e_f), and elastic modulus (E) were obtained based on the average of three tests.

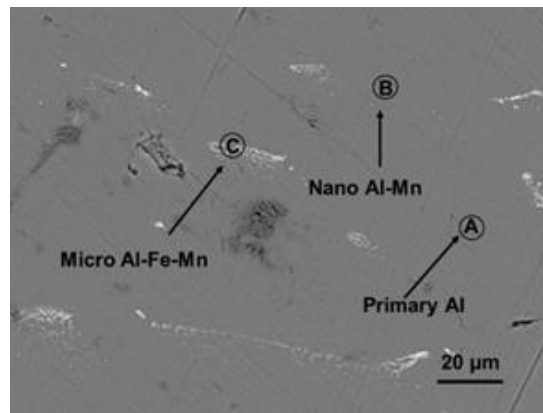
3.2.5 Measurement of Electrical Conductivity

The electrical conductivity is an important electrical property of the both the PSMC Al-0.3Mn alloy and PSMC HP Al specimens. The handheld device SIGMASCOPE with FS40 probe was employed to perform the electrical conductivity measurements of the the PSMC Al-0.3Mn alloy and PSMC HP Al specimens based on the phase sensitive eddy current method. This type of signal evaluation enables non-contact measurement. It also minimizes the influence of surface roughness. The measuring range of the device is 0.5 - 108% IACS (% International Annealed Copper Standard), and the accuracy at room temperature is $\pm 0.5\%$ of the measured reading. The minimum measurable radius of the specimen was 7 mm. The electrical conductivity data were obtained based on the average of three tests.

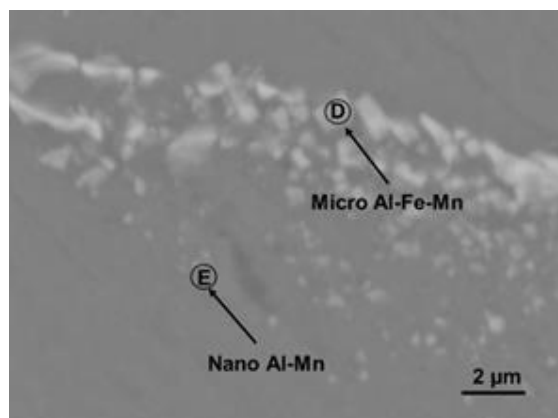
3.3 RESULTS AND DISCUSSION

3.3.1 Microstructure

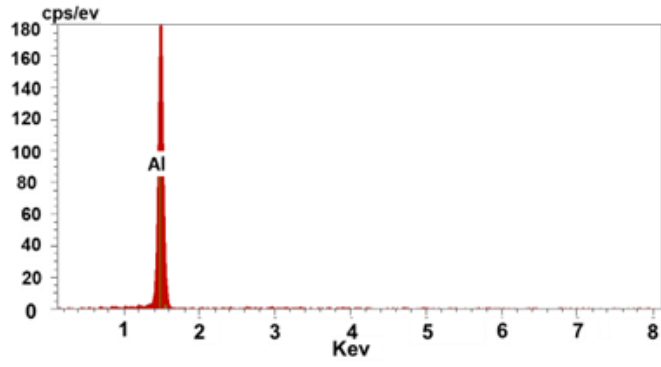
Figure 3.1 presents SEM micrographs and EDS spectra showing the microstructural constituents of the permanent steel mod cast (PSMC) Al-0.3% Mn alloy and PSMC HP Al. The microstructure of the PSMC Al-0.3Mn alloy mainly consisted of not only the primary α -Al phase (gray) but also the micron Al-Fe-Mn intermetallic phases and nano Al-Mn intermetallic phase (white). The observation on the element distribution and phase morphology in areas A, B and C implied the presence of the primary Al phase as matrix and the intermetallic phases in the form of precipitates as indicated in Figure 3.1(a)-(d).



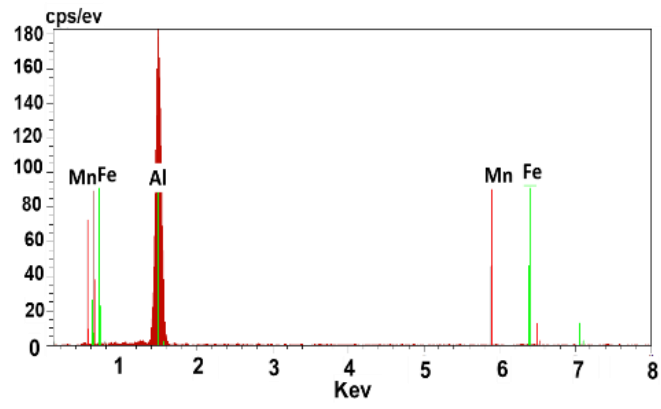
(a)



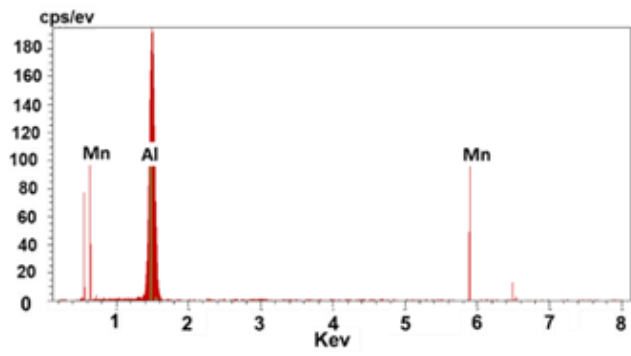
(b)



(c)



(d)



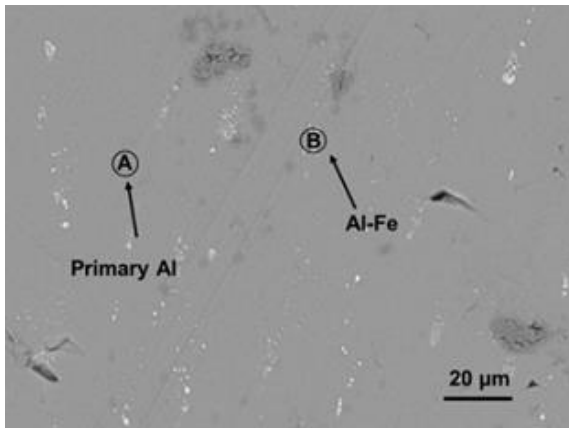
(e)

Figure 3.1 SEM micrographs showing microstructure of PSMC Al-0.3Mn alloy, (a) low and (b) high magnifications, and EDS spectra identifying (c) primary Al phase, (d) micron Al-Fe-Mn phase, and (e) nano Al-Mn phase.

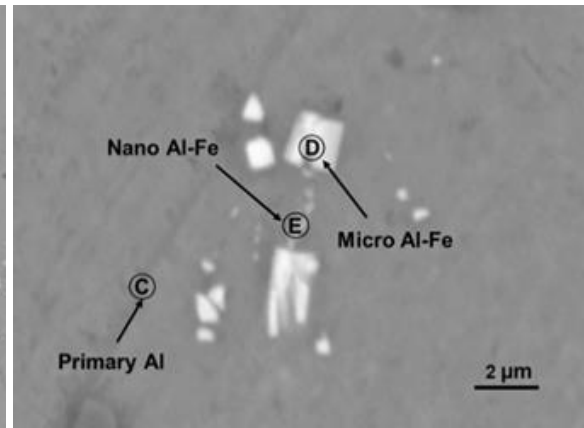
Also, according to the SEM and EDS analyses, nano Al-Mn particles were identified besides the micron-sized Al-Fe-Mn phase as can be seen from areas E and D in Figure 3.1 (b). The examination of the SEM micrograph also revealed the presence of porosity (dark gray), due to the poor feedability of the PSMC Al-0.3Mn alloy.

Figure 3.2 gives SEM micrograph and EDS spectra for the PSMC HP Al. Compare to that of the PSMC Al-0.3Mn alloy, the microstructure of the PSMC HP Al was comprised of different phases and porosity. The microstructural constituents were identified by the EDS spectra given in Figure 3.2 (c) and (d). It was revealed that the primary Al (gray), and micron Al-Fe and nano Al-Fe intermetallic phases (white) were present in the microstructure. The porosity was also observed due to the poor castability of the HP Al.

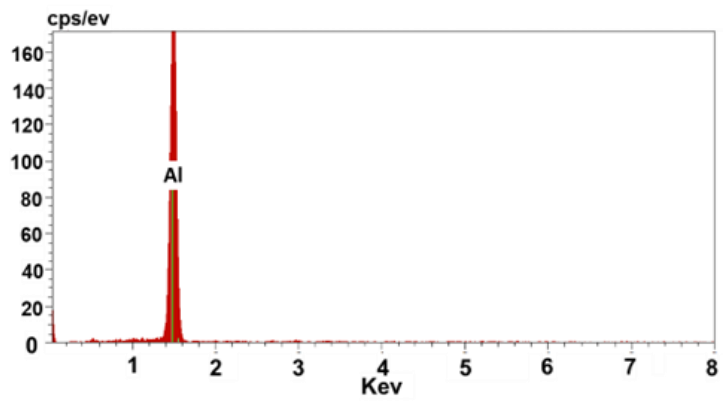
To determine the area fractions of the intermetallic phases, ImageJ was used to convert the SEM micrographs to binary and white images, with the black areas representing the intermetallic phases (Al-Fe-Mn, Al-Fe and Al-Mn phases) and the white areas representing primary α -Al. Following conversion, the software automatically calculated area fractions of black and white areas. Figure 3.3 presents the converted micrographs highlighting the presence of the intermetallic phases in the observed PSMC Al-0.3Mn alloy and HP Al represented by the black areas. Figure 3.4 shows the area fractions of the intermetallic phases. The area fractions of the intermetallic phases in the PSMC Al-0.3Mn alloy and the PSMC HP Al were measured to be 2.1 and 0.4% , respectively.



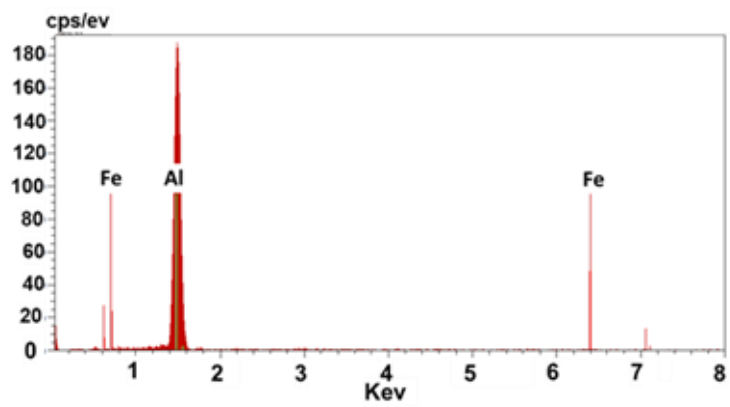
(a)



(b)

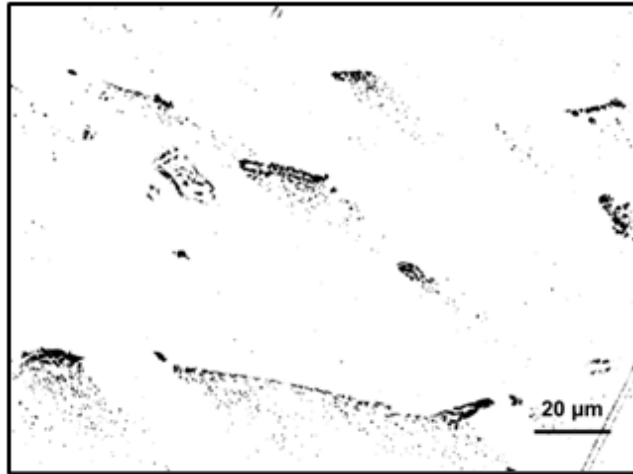


(c)

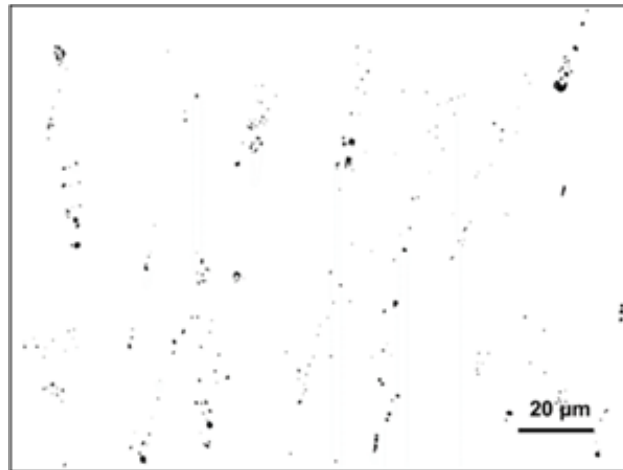


(d)

Figure 3.2 SEM micrograph showing microstructure of PSMC HP Al (99.9%), (a) low (b) high magnifications, and EDS spectra identifying (c) primary Al phase, (d) Al-Fe intermetallic phase,



(a)



(b)

Figure 3.3 Micrographs in binary black and white images showing the contents of intermetallics in (a) the PSMC Al-0.3% Mn alloy and (b) the PSMC HP Al.

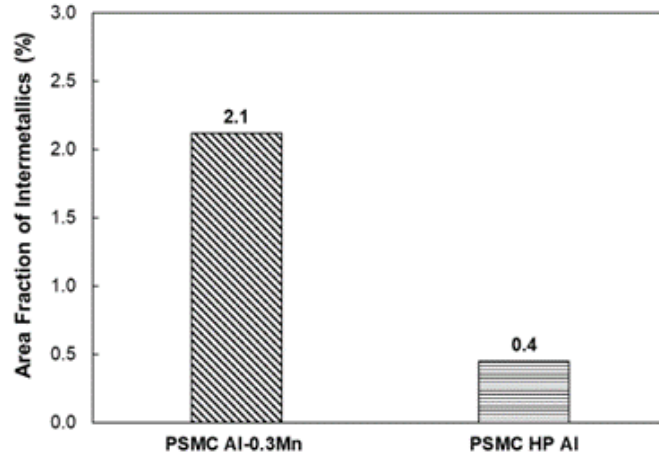
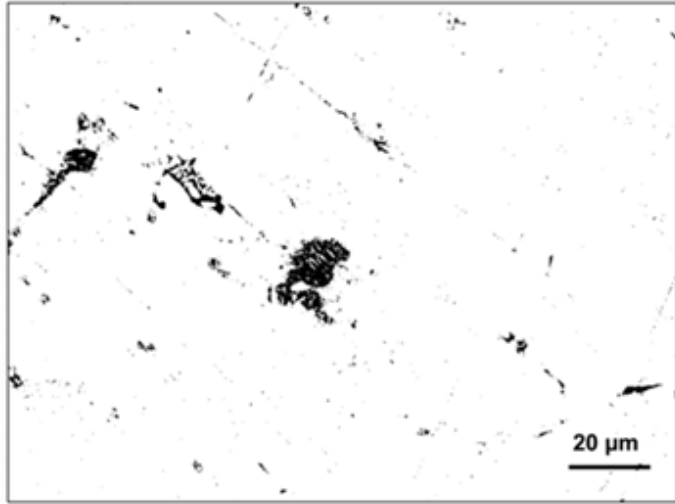


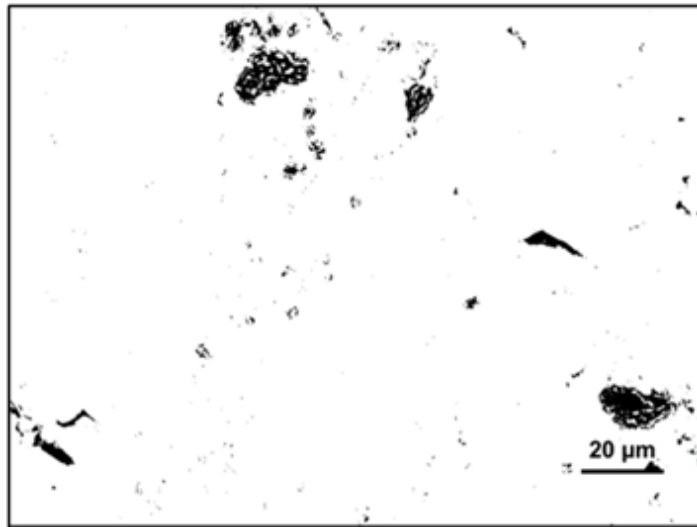
Figure 3.4 Area Fractions of the PSMC Al-0.3Mn alloy and HP Al (99.9%).

3.3.2 3.2. Porosity Evaluation

Figure 3.5 presents the binary black and white images converted from the SEM micrographs by ImageJ, showing the porosity contents in the PSMC Al-0.3Mn alloy and PSMC HP Al. It is worthwhile noting that both the PSMC Al-0.3Mn alloy and the HP Al were cast in the steel mold with the cross-section thickness of 10 mm, which suggested they were cooled in a relatively slow rate. Therefore, these two materials exhibited the large number of gas and shrinkage pores (black area). The porosities of the PSMC Al-0.3Mn alloy and the PSMC HP Al alloys determined quantitatively from the density measurements and the imageJ analyses are shown in Figure 3.6. The porosity of the PSMC Al-0.3Mn alloy was around 2.26% from the density measurement and 2.12% from the imageJ. The PSMC HP Al had a porosity level of 2.25% from the imageJ, which was similar with that (2.26%) of the PSMC Al-0.3Mn alloy.



(a)



(b)

Figure 3.5 Binary black and white images showing porosity in (a) PSMC Al-0.3Mn alloy and (b) PSMC HP Al.

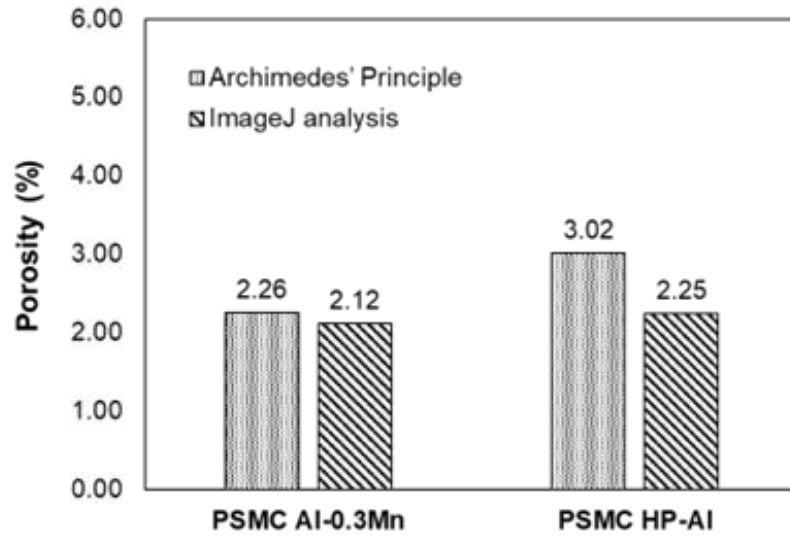


Figure 3.6 Porosity contents of the PSMC Al-0.3Mn alloy and HP Al (99.9%).

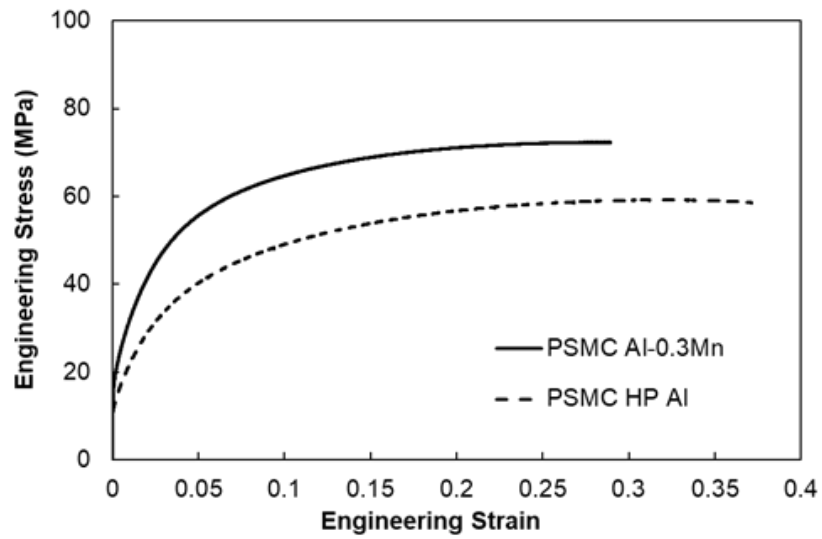


Figure 3.7 Typical engineering stress vs. strain curves of the PSMC Al-0.3Mn alloy and PSMC HP Al.

Table 3.2 Tensile properties of the PSMC Al-0.3Mn alloy and PSMC HP Al (99.9%)
at room temperature

| Material | UTS (MPa) | YS (MPa) | e_f (%) | Modulus (GPa) |
|---------------------|-----------|----------|-----------|---------------|
| PSMC Al-0.3Mn Alloy | 72.3 | 20.4 | 28.9% | 66.3 |
| PSMC HP Al | 59.2 | 14.0 | 37.1% | 60.8 |

3.3.3 Tensile Behavior

Tensile properties

The typical engineering stress–strain curves from tensile testing of the PSMC Al-0.3Mn alloy and PSMC HP Al with a cross-sectional thickness of 10 mm are shown in Figure 3.7. Table 3.2 lists the tensile properties of the PSMC Al-0.3Mn alloy and HP Al. As shown in Figure 3.7, the slope of the linear portion of the engineering curve for the PSMC Al-0.3Mn alloy had a large increasing tendency than that of the PSMC HP Al. The UTS of the PSMC Al-0.3Mn alloy and PSMC HP Al were 72.3 MPa and 59.2 MPa, respectively, which signifies an improvement of 22% over that of the PSMC HP Al for the as-cast conditions. The yield strength of the PSMC Al-0.3Mn alloy was 20.4 MPa on average, which was 46% higher than that of the PSMC HP Al (14.0 MPa). However, the elongation of the PSMC Al-0.3Mn alloy was 28.9%, whereas the elongation of the PSMC HP Al (99.9%) was 37.1%, which had a decrease of 22% over that of the PSMC HP Al.

Resilience

The ability of a material to absorb energy is referred to as resilience when it is deformed elastically, and releases that energy upon unloading. The resilience is usually measured by

the modulus of resilience which is defined as the maximum strain energy absorbed per unit volume without creating a permanent distortion. It can be calculated by integrating the stress-strain curve from zero to the elastic limit. In uniaxial tension, the strain energy per unit volume can be determined by the following equation [4, 16, 17]:

$$U_r = \frac{(YS)^2}{2E} \quad (\text{Eq 3})$$

where U_r is the modulus of resilience, YS is the yield strength, and E is the Young's modulus. The calculated modulus of resilience for PSMC Al-0.3Mn alloy and PSMC HP Al (99.9%) are given in Table 3.3. In comparison between the PSMC Al-0.3Mn alloy and PSMC HP Al (99.9%), the modulus of resilience in the PSMC Al-0.3Mn alloy was 3.14 kJ/m^3 higher than that of the PSMC HP Al (99.9%) (1.61 kJ/m^3). As such, the PSMC Al-0.3Mn alloy was much more capable of resisting energy loads in engineering application during service, in which no permanent deformation and distortion are allowed.

Toughness

The tensile toughness of a ductile alloy is its ability to absorb energy during static loading condition, i.e., static deformation with a low strain rate. The ability to bear applied stresses higher than the yield strength without fracturing is usually required for various engineering applications. The toughness for ductile alloys can be considered as the total area under the stress-strain curve for the amount of the total energy per unit volume. To evaluate the deformation behavior, the energy expended in deforming a ductile alloy per unit volume given by the area under the stress-strain curve can be approximated by [4, 16]

$$U_t = U_{el} + U_{pl} = \frac{(YS+UTS) \times e_f}{2} \quad (\text{Eq 4})$$

where U_t is the total energy per unit volume required to reach the point of fracture, U_{el} is the energy per unit volume for elastic deformation, U_{pl} is the energy per unit volume for plastic deformation, and e_f is the elongation at fracture. Table 3.3 lists the calculated U_t for the PSMC Al-0.3Mn alloy and PSMC HP Al (99.9%). The PSMC Al-0.3Mn alloy had a U_t value of 13.40 MJ/m^3 , which was comparable to that (13.58 MJ/m^3) of the PSMC HP Al (99.9%). The total area under the engineering stress and strain curve of the PSMC Al-0.3Mn alloy was almost the same as that of the PSMC HP Al (99.9%). This was because the PSMC Al-0.3Mn alloy had the much higher ultimate tensile strength and yield strength, despite the PSMC HP Al (99.9%) having a very high elongation. Hence, the PSMC Al-0.3Mn alloy capable of absorbing the energy during deformation was as tough as the PSMC HP Al (99.9%).

Table 3.3 Tensile toughnesses and resiliences of PSMC Al-0.3Mn alloy and PSMC HP Al (99.9%) at room temperature

| Material | Resilience (kJ/m^3) | Toughness (MJ/m^3) |
|---------------------|-----------------------------------|----------------------------------|
| PSMC Al-0.3Mn Alloy | 3.14 | 13.40 |
| PSMC HP Al | 1.61 | 13.58 |

Strain Hardening

Figure 3.8 show the true stress vs. strain curves of the PSMC Al-0.3Mn alloy and PSMC HP Al. The true stress and strain for plastic deformation can be related by the power law equation:

$$\sigma_t = K \varepsilon_t^n \quad (\text{Eq 5})$$

where σ_t is the true stress, ε_t is the true strain, K is the strength coefficient, and n is the strain-hardening exponent [17, 18]. The regression analysis indicated that the power expression agreed well with the tensile data. The numerical values of the derived constants in Eq (5) with the regression coefficients (R^2) are listed in Table 3.4. The high strain-hardening exponent implied that the PSMC Al-0.3Mn alloy would gain strength more quickly than the PSMC CP Al during plastic deformation.

To determine the strain-hardening rate ($d\sigma_t/d\varepsilon_t$), Eq (5) was differentiated to obtain:

$$d\sigma_t/d\varepsilon = K n \varepsilon_t^{n-1} \quad (\text{Eq 6})$$

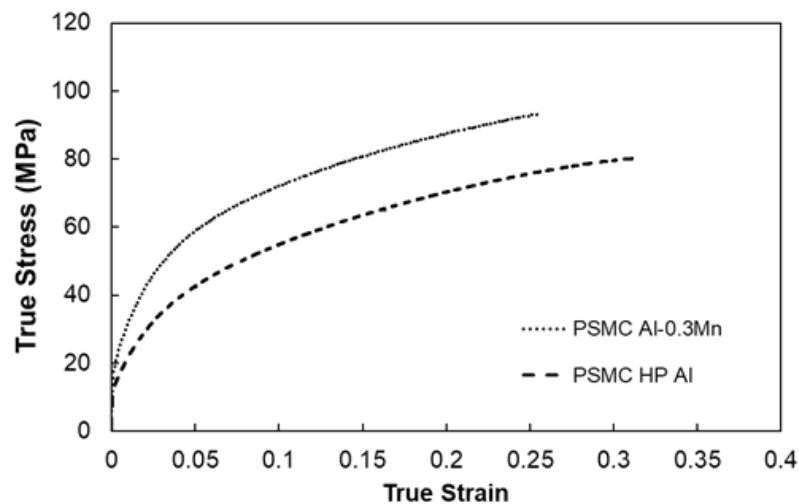


Figure 3.8 True stress vs. strain curves

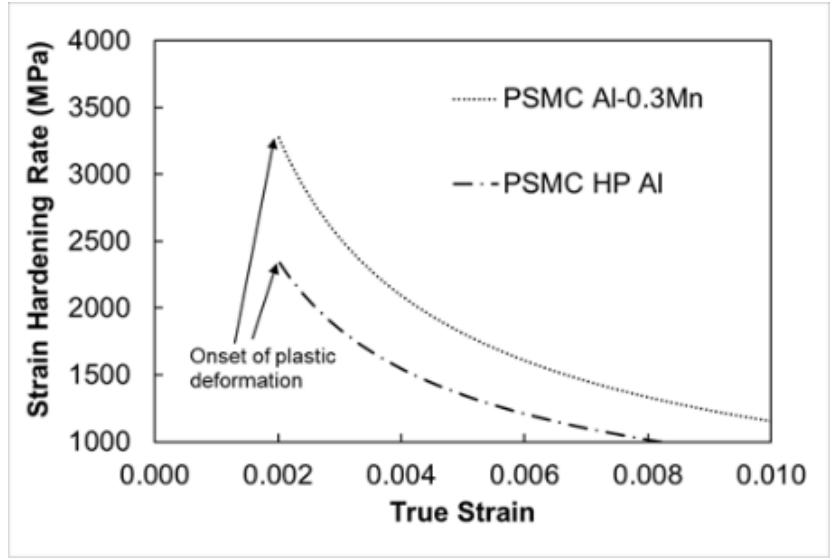


Figure 3.9 Strain hardening curves

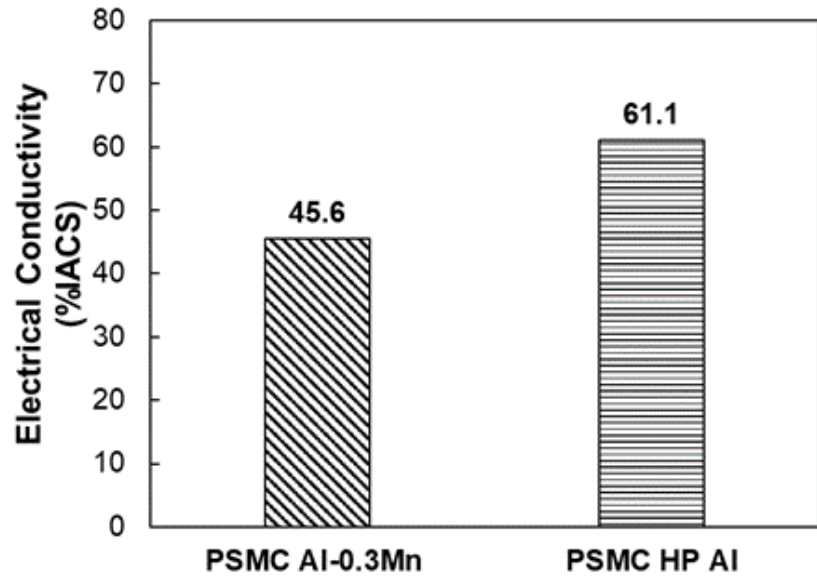


Figure 3.10 Electrical conductivities

Figure 3.9 presents the strain-hardening rate versus true plastic strain curve during the plastic deformation, which was derived from the true stress versus true strain curve (Figure

3.8). Upon the onset of plastic deformation at a strain of 0.002, the strain-hardening rate of the PSMC Al-0.3Mn alloy was 3253 MPa, as the PSMC HP Al exhibited a strain-hardening rate of 2318 MPa. In the early stage of plastic deformation, the strain-hardening rate of PSMC Al-0.3Mn alloy was 40% higher than that of the PSMC HP Al. As the strain increased to 0.008, the strain-hardening rates of the PSMC Al-0.3Mn alloy and HP Al decreased to 1312 and 1007 MPa, respectively. At a strain of 0.008, the strain-hardening rate of the PSMC Al-0.3Mn alloy remained higher than that of the PSMC HP Al by 30%. An observation of the variation of strain-hardening rate versus strain suggested that, compared to the HP Al, the PSMC Al-0.3Mn alloy could strengthen itself spontaneously to a large degree upon plastic deformation. The high content of the intermetallic phases in the microstructure of the PSMC Al-0.3Mn alloy should be responsible for the high tensile properties and strain hardening rate. The tensile behavior of the PSMC Al-0.3Mn alloy and HP Al generally agreed with the microstructural observation.

Table 3.4 Best fit parameters for power equations

| Material | K (MPa) | n | R ² |
|---------------------|---------|--------|----------------|
| PSMC Al-0.3Mn Alloy | 165.17 | 0.3505 | 0.9962 |
| PSMC HP Al | 137.66 | 0.393 | 0.9988 |

3.3.4 Electrical Conductivities

The electrical conductivities of both the PSMC Al-0.3Mn alloy and PSMC HP Al are displayed in Figure 3.10. The electrical conductivity of the PSMC Al-0.3Mn alloy was 45.6 %IACS, while it was 61.1 %IACS for the PSMC HP Al (99.9%). There was

a decrease of 25% in the electrical conductivity of the PSMC Al-0.3 Mn alloy compared to that of the PSMC HP Al. However, the conductivity of 45.6 %IACS was much higher than those (30 %IACS) of the commercially available Al casting alloys. The microstructure analyses indicated that the addition of 0.3 wt% Mn was primarily consumed in the formation of the Al-Mn intermetallic phase. As a result, a limited amount of Mn was dissolved in the primary Al, which made the Al electron movement almost unaffected in the Al-Mn solid solution. The minimum requirement of the electrical conductivity for the EV motor applications is about 48 %IACS [1]. The difference between the 48 and 45.6 %IACS is only 5%. The proper adjustment of the Mn content in Al-Mn solid solution should boost the electrical conductivity of Al-Mn alloy to meet the industrial specification. The similar phenomena taking place in the cast Al-Fe alloys [17, 18] and Mn-containing wrought Al alloys [19] were observed previously.

3.4 SUMMARY

The results of tensile testing of the PSMC Al-0.3Mn alloy and HP Al showed that the UTS, YS and resilience of the PSMC Al-0.3Mn alloy were 72.3 and 20.4 MPa, and 3.14 kJ/m³, respectively, which were higher than those (59.2 and 14.0 MPa, and 1.61 kJ/m³) of the PSMC HP Al. The toughness of the PSMC Al-0.3Mn alloy was 13.40 MJ/m³, which was comparable to that (13.58 MJ/m³) of the PSMC HP Al. But, the elongation of the PSMC Al-0.3Mn alloy was only 28.9%, which was lower than that (37.1%) of the PSMC HP Al. The difference in tensile behavior between the PSMC Al-0.3Mn alloy and the HP Al should be attributed to the fact that the relatively large amount of the micron Al-Fe-Mn and nano Al-Mn intermetallic phases was present in the PSMC Al-0.3Mn alloy, compared to almost little intermetallic phase in the PSMC HP Al. The addition of 0.3 wt% Mn affected the electrical conductivity of the PSMC HP Al, which was only slightly below the industrial specification for the EV motor application.

3.5 REFERENCES

- [1] Y. Li, A. Hu, Y. Fu, S. Liu, W. Shen, H. Hu and X. Nie, “Al Alloys and Casting Processes for Induction Motor Applications in Battery-Powered Electric Vehicles: A Review,” *Metals*, vol. 12, pp.216-241, 2022.
- [2] S. Liu, A. Hu, H. Hu, X. Nie and N.C. Kar, “Potential Al-Fe Cast Alloys for Motor Applications in Electric Vehicles: An Overview,” *Key Eng. Mater.* Vol.923, pp. 3-19, 2022.
- [3] M. Y. Murashkin, I. Sabirov, X., Sauvage, & R. Z. Valiev, “Nanostructured Al and Cu alloys with superior strength and electrical conductivity,” *J Mater Sci.* Vol. 51(1), pp. 33-49, 2016.
- [4] Y. Li, Y. Fu, A. Hu, X. Nie and H. Hu, “Effect of Sr and Ni Addition on Microstructure, Tensile Behavior and Electrical Conductivity of Squeeze Cast Al-6Si-3Cu Al Alloy,” *Key Eng. Mater.* Vol.921, pp. 3-14, 2022.
- [5] H. Ishikawa, Y. Takashima, Y. Okada, “Squirrel-Cage motor Rotor and Squirrel-Cage Motor.” U.S. Patent 9 935 533, 2018.
- [6] P. Sivanesh, K. Charlie, S.J. Robert, F. Ethan, E. Paul, “Aluminum Alloys for Die Casting.” U.S. Patent 20210332461A1, 2021.
- [7] S. W. Nam, D. H. Lee, “The effect of Mn on the mechanical behavior of Al Alloys.” *Met. Mater. Int.* Vol. 6, no. 1 , pp. 13-16, 2000.
- [8] A. J. McAlister, J. L. Murray, “The (Al-Mn) aluminum-manganese system - journal of phase equilibria.” *Bulletin of Alloy Phase Diagrams* Vol. 8, no. 5 , pp. 438–447, 1987.

- [9] J. Davis, ASM Specialty Handbook: *Aluminum and Aluminum Alloys*; ASM International, OH, USA, 2002.
- [10] D. Beaulieu, *Characteristics of Structural Aluminum*; Presses de l'aluminium: Chicoutimi, QC, Canada, 2005.
- [11] T. Bubonyi, P. Barkoczy. "Evaluation of Eutectic Structure in Aluminum Alloys." DOI:10.26649/musci.2019.073, MultiScience - XXXIII. microCAD International Multidisciplinary Scientific Conference, University of Miskolc, Borsod-Abaúj-Zemplén, Hungary, 23-24 May, 2019.
- [12] "Standard Test Method for Density of High-Modulus Fibers." D3800-99, *ASTM*, Vol 15.03, pp. 186-187, 2002
- [13] "Standard Test Method for Dry and Wet Bulk Density, Water Absorption, and Apparent Porosity of Thin Sections of Glass-Fiber Reinforced Concrete," C948-81, ASTM Standards, *ASTM*, Vol 04.05, pp. 588-589, 2002.
- [14] T.J. Collins, "ImageJ for Microscopy," *Biotechniques*, 43(1), S25–S30, 2007.
- [15] "Standard Test Methods for Tension Testing Wrought and Cast Aluminum-and Magnesium-alloy Products," B557M, ASTM Standards, *ASTM*, Vol 02 02, 424-439, 2002.
- [16] W.D. Callister and D.G. Rethwisch: *Materials Science and Engineering*. 10th edition, Wiley, USA, 2018.
- [17] S. Liu, A. Hu, A. Dhaif, W. Shen, H. Hu. "Mechanical Properties and Electrical Properties of Permanent Mold Cast Eutectic Al-1.8Fe Alloy. *Aluminum*

Alloys, Characterization and Processing.” *TMS Annual Meeting & Exhibition, San Diego*, United States of America. In press, 2023.

[18] X. Wang, R.G. Guana, R.D.K. Misra, Y. Wang, H.C. Li, Y.Q. Shang, “The mechanistic contribution of nanosized Al₃Fe phase on the mechanical properties.” *Mater. Sci. Eng A*, vol. 724, pp. 452-460, 2018.

[19] R. M. Miri, “Effect of Manganese (Mn) Content and Homogenization Treatment on Hot Deformation of AA3xxx Aluminum Alloys, ” Master Thesis, University of Waterloo, Waterloo, Ontario, Canada, 2016.

Chapter 4: Section Thickness Effect on Microstructure, Mechanical and Electrical Properties of Permanent Steel Mold Cast Al-0.3Mn Alloy

4.1 INTRODUCTION

The demand for battery-powered electric vehicles (BEVs) rises in the auto market because of environmental concerns and high fuel price. In general, the BEVs are relatively heavier than gasoline-powered vehicles (GPs). The weight reduction in the BEVs becomes urgent for energy efficiency and extended range. Decreasing the weight of the electric motors (EMs), as one of the heaviest components in the BEVs, appears to be a quick solution [1]. Conventionally, copper has been widely used in the EMs due to its high electrical conductivity [2]. However, as a light metallic element with a density of 2700 kg/m³, aluminum is 70% lighter than copper (8960 kg/m³), and its melting point of 660 °C is 423 °C lower than that (1083 °C) of copper. Contrast to copper, aluminum and its alloys can be easily used to manufacture complex components in the EM with various casting processes [3]. But, the strengths including the ultimate tensile strength (UTS) and the yield strength of pure aluminum are very low. Despite that pure aluminum has relatively high electrical conductivity around 60% IACS, its yield strength is only 10 MPa. To achieve the desired performance of the Al-containing EMs during operation, a large cooling system has to be installed in the EMs, which increases their size and weight [4]. To effectively reduce the EM weight, Al alloys with both high strength and electrical conductivity need to be developed and implemented for the EM size reduction by eliminating the cooling system in the EMs. To fabricate Al components in the EM, permanent steel mold casting

(PSMC) as one of the most cost-effective manufacturing techniques, and widely used in casting light alloys [5, 6]. Commercially-available cast Al alloys have high strengths but low electrical conductivities, as the strength and conductivity of metallic materials are mutually exclusive. It has been pointed out [7, 8] that, in Al alloys, insoluble alloying elements can achieve higher electrical conductivity than soluble elements in high-strength alloys. Manganese as a low-cost transition metal has a maximum solubility of about 1.25 in Al at 658 °C [9, 10]. As a result, Mn addition enables the development of low-cost Al alloys with not only high strengths but also high electrical conductivities, which are required for applications in the EMs.

In the past, the influence of section thickness on mechanical properties of cast Al and Mg alloys has been reported in the literature [11-15]. Zhang et al. [13] reported that, the reduction in the section thicknesses of the squeeze cast AM60 alloy from 20 mm to 6 mm increased the solidification rate from 2.8 °C/s to 11.9 °C/s. The tensile properties of the alloy were influenced by the section thickness. The significant increases in elongation (176%), ultimate tensile strength (67%) and yield strength (43%) of the 6 mm alloy over the 20 mm section were achieved. Sun et al. [14] investigated the effect of section thicknesses on tensile properties, strain-hardening and fracture behaviors of the die cast AZ91 with section thicknesses of 2, 6 and 10 mm. The results of tensile testing indicate that ultimate tensile strength (UTS), yield strength (YS), elongation (ϵ_f), strain hardening rate ($d\sigma/d\epsilon$), as well as resilience (U_r) and toughness (U_t) increase significantly with a reduction in the section thickness of the alloy. However, studies on section thickness-

dependent mechanical properties and electrical properties of Mn-containing Al alloys are scarce.

This paper presents the microstructure, mechanical properties, and electrical conductivity of the Al-0.3Mn alloy samples with different section thicknesses of 6, 10 and 20 mm, which were prepared by permanent steel mold casting (PSMC). The microstructure-property relationship and the mechanism for property improvement were discussed.

4.2 EXPERIMENT PROCEDURE

4.2.1 Material and casting

An Al-0.3Mn alloy with the chemical composition listed in Table 4.1 was selected for investigation. In casting run, about 700 g of the alloy melt in a graphite crucible was prepared under the protection of nitrogen in an electrical resistance furnace. The melt was held at $720 \text{ }^{\circ}\text{C} \pm 10 \text{ }^{\circ}\text{C}$ for about 20 min, stirred for 10 minutes to homogenize its chemical composition, and then poured into a permanent steel mold to produce a step casting with the different section thicknesses of 6, 10 and 20 mm.

Table 4.1 Chemical composition of Al-0.3Mn alloy

| Materials | Chemical composition | | | | | | | |
|-----------|----------------------|-------|-------|--------|-------|-------|---------|--------|
| | Mn | Fe | Si | Cu | Zn | C | Al | Others |
| Al-0.3Mn | 0.30 | 0.034 | 0.062 | <0.002 | <0.01 | <0.01 | Al main | None |

4.2.2 Cooling rate determination

As it is quite difficult to precisely place the temperature sensor in the center of each step inside the permanent steel mold for temperature measurements, the numerical simulation (Magmasoft®) as a designated casting software was used to simulate the cooling process of the permanent steel mold casting and determine the cooling rate (CR) of the sections with different thicknesses. The calculation of the cooling rate was based on the initial cooling period of the curves predicted by Magamasoft.

4.2.3 Porosity measurement

Porosity was quantitatively determined by density measurements. Based on the weight measurement of the permanent steel mold cast (PSMC) Al-0.3Mn at different section thickness specimens in air and water, the actual density (D_a) of each specimen was determined using Archimedes principle based on ASTM Standard D3800 [16]

$$D_a = \frac{D_w W_a}{W_a - W_w} \quad (\text{Eq 1})$$

where W_a and W_w are the weight of the specimen in the air and in the water, respectively, and D_w the density of water. The porosity of each specimen was calculated by the density values through the following equation (ASTM C948) [17]

$$\% \text{ Porosity} = \left[\frac{D_t - D_a}{D_t} \right] \times 100\% \quad (\text{Eq 2})$$

where D_t is the theoretical density (2720 kg/m^3) of the Al-0.3Mn alloy, which was calculated based on the weight percentages of pure Al and Mn, with the densities of 2710 and 7430 kg/m^3 , respectively [6].

4.2.4 Microstructure Analysis

Metallographic specimens were cut from the center of the cast step sample. Standard mounting and polishing procedures were then applied to the cut metallographic samples prior to observation. Detailed characteristics of the microstructures were characterized by a scanning electron microscope (SEM), Hitachi™ Tabletop Microscope TM3000 (Tokyo, Japan) with a maximum resolution of 30 nm in the backscatter mode / $1 \mu\text{m}$ in the X-ray diffraction mapping mode, and useful magnifications of 10 to 10,000 to maximize the composition reading of energy dispersive spectroscopy (EDS) data. Quantitative assessment of prepared specimen microstructure included calculation of area fraction of

different phase constituents as well as porosity by using ImageJ, a public domain image processing system to identify microstructure characteristics through image contrast [18]. The sizes of the primary α -Al dendrites were determined by the linear intercept method aided by ImageJ [15].

4.2.5 Tensile Testing

The mechanical properties of both the PSMC Al-0.3Mn with three different thicknesses specimens were evaluated by the tensile testing, which was carried out at ambient temperature on a MTS Criterion (Model 43) tensile test machine (Eden Prairie, MN, USA) equipped with a data acquisition system. According to ASTM B557 [19], subsize flat tensile specimens (0.025 m in gage length, 0.006 m in width) were machined from the PSMC step coupons. The strain rate during tensile testing was 0.5 mm/min with a sampling rate of 10 Hz. The tensile properties, including 0.2% yield strength (YS), ultimate tensile strength (UTS), elongation to failure (e_f), and elastic modulus (E) were obtained based on the average of three tests.

4.2.6 Electrical Conductivity.

The handheld device SIGMASCOPE with FS40 probe was employed for the electrical conductivity measurements of the PSMC specimens based on the phase sensitive eddy current method. This type of signal evaluation enables non-contact measurement. It also minimizes the influence of surface roughness. The measuring range of the device is 0.5 – 108 %IACS (International Annealed Copper Standard), and the accuracy at room temperature was 0.5% of the measured reading. The minimum measurable radius of the

specimen was 7 mm. The electrical conductivity data were obtained based on the average of three tests [20].

4.3 RESULTS AND DISCUSSION

4.3.1 Solidification

Figure 4.1 illustrates the cooling curves of the PSMC Al-0.3Mn with the section thicknesses of 6, 10 and 20 mm, which were predicted by the numerical simulation. The calculated cooling rates are summarized in Table 4.2, which were 2.1, 8.3, and 23.8 °C/s for the sections of 20, 10 and 6 mm, respectively. Figure 4.2 shows the relationship between the cooling rate and different section thicknesses. The cooling rate of the thin section (6 mm) was ten times higher than the thick part (20 mm), which could significantly affect the microstructure development of the alloy including both the primary and secondary phases. The previous studies on various nonferrous alloys [8, 11-15] revealed the relationship between the cooling rate and the microstructure development, i.e., the higher the cooling rate, the finer the microstructure.

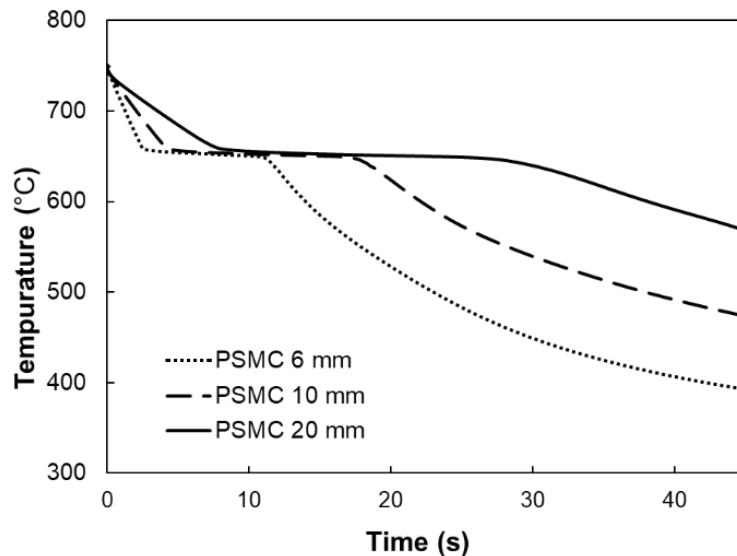


Figure 4.1 Cooling curves of the PSMC Al-0.3Mn alloy with the section thicknesses of 6, 10 and 20 mm.

Table 4.2 Cooling rates of the PSMC Al-0.3Mn alloys with the section thicknesses of 6, 10 and 20 mm

| Thickness (mm) | 20 | 10 | 6 |
|---------------------|-----|-----|------|
| Cooling rate (°C/s) | 2.1 | 8.3 | 23.8 |

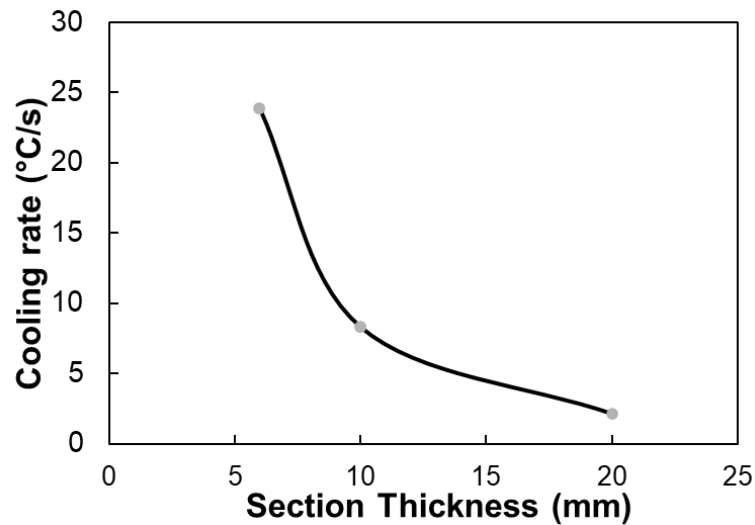


Figure 4.2 Cooling rate of the PSMC Al-0.3Mn alloy vs. section thicknesses.

Figure 4.3 presents the results of solidification sequences of the PSMC Al-0.3Mn alloy with the three section thicknesses of 6, 10 and 20 mm, predicted by simulation Magmasoft. Figure 4.3 (a) through (d) illustrate the PMSC casting solidified by 20%, 40%, 60% and 80%, respectively. It can be clearly seen that the thin section solidified much faster than the thick part as the temperature in the thin section dropped more rapidly. The last solidification location ended at the upper center of the 20-mm section. Consequently, as shown in Figure 4.2, the cooling or solidification rate of the thin section was much higher

than the thick part, which had a large effect on the microstructure as well as the mechanical properties of the alloy.

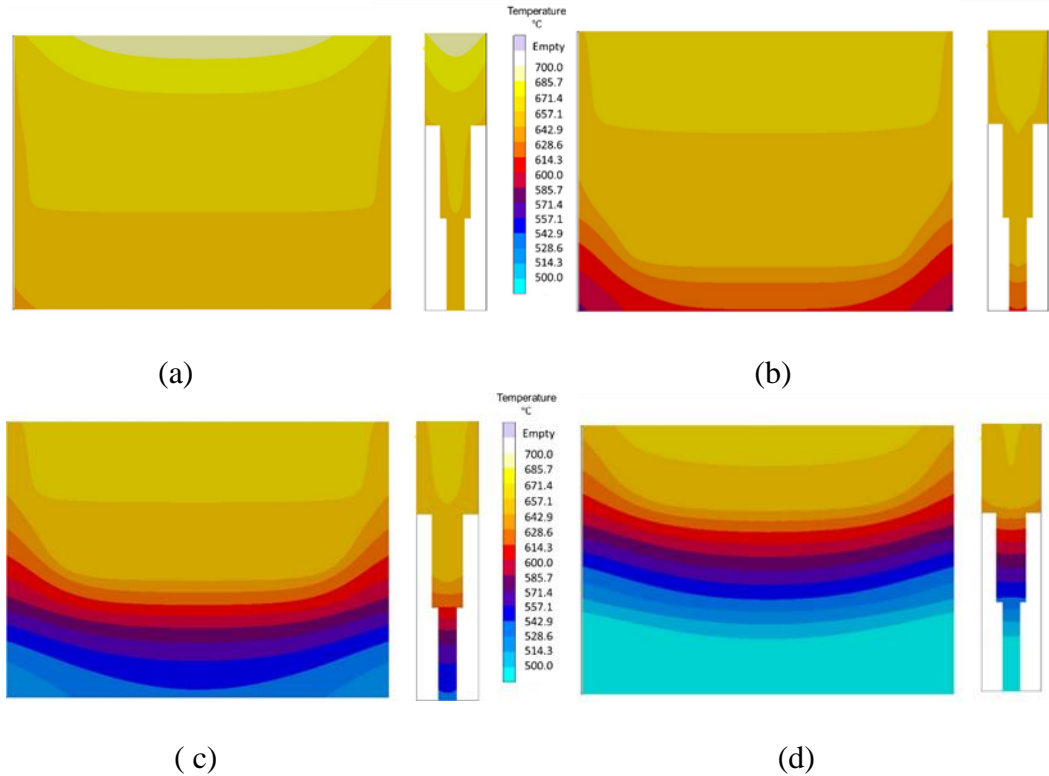
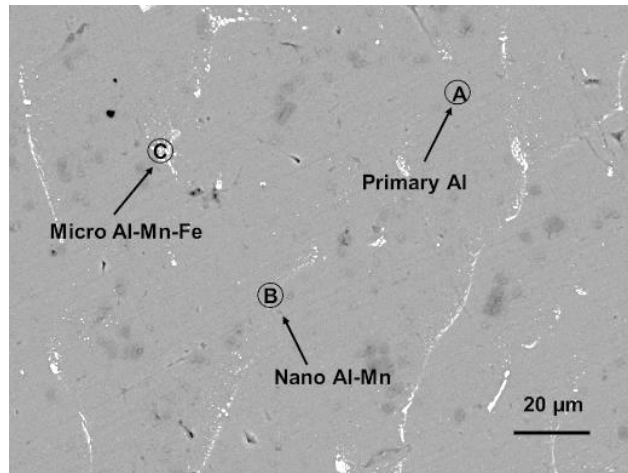


Figure 4.3 Simulation on solidification of the the PSMC Al-0.3Mn alloy with the three section thicknesses of 6, 10 and 20 mm, a) 20% b) 40% c) 60%, and d) 80% solidified.

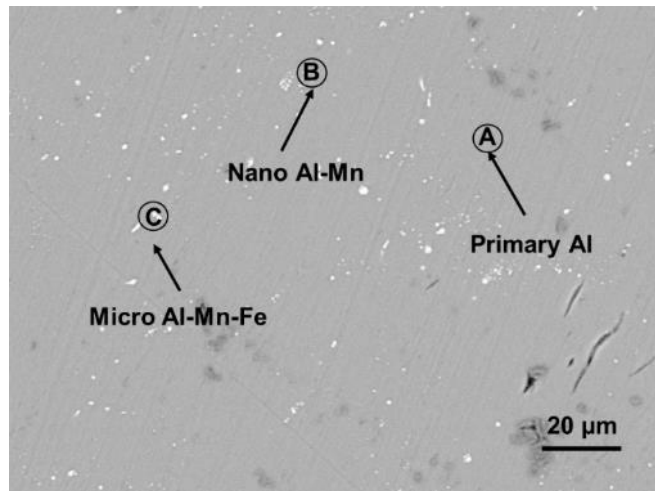
4.3.2 Microstructural Constituents and Phase Identification

Figure 4.4 shows the microstructures of the PSMC Al-0.3Mn alloy for the sections of 6, 10, and 20 mm in low magnification. They mainly consisted of not only the primary α -Al phase (area A, dark grey), but also the nano Al-Mn intermetallic phase (area B, light white), and micron Al-Fe-Mn intermetallic phases (area C, light grey). The SEM analysis at high magnification evidently revealed the presence of the nano-sized phase as shown in Figure 4.5. The results of the EDS analysis are shown in Figure 4.6, and the elements

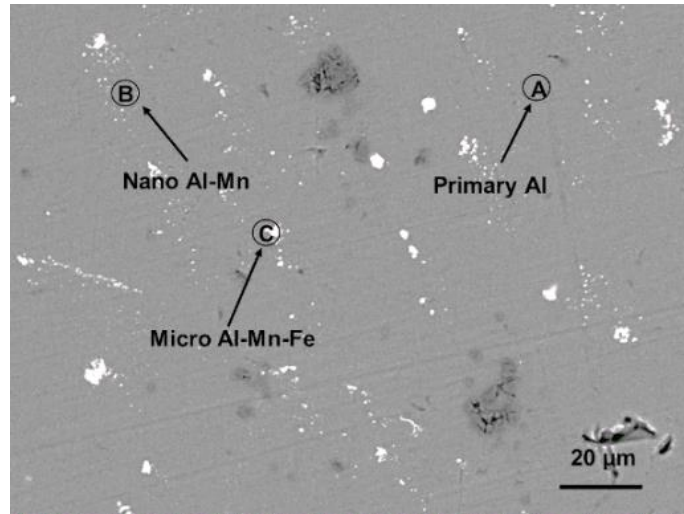
analysis in atomic percentages are listed in Table 4.3. The micron Al-Mn-Fe phase and nano Al-Mn phase were found in the form of fine particles distributing inside and surrounding the boundaries of the primary α -Al grains. The observation on the element distribution and phase morphology in areas A, B and C implied the presence of the primary Al phase as matrix and the intermetallic phases in the form of precipitates as indicated in Figure 4.4(a)-(c).



(a)



(b)



(c)

Figure 4.4 SEM micrographs showing microstructures of the PSMC Al-0.3Mn alloy with the section thicknesses of (a) 6, (b) 10, and (c) 20 mm, respectively.

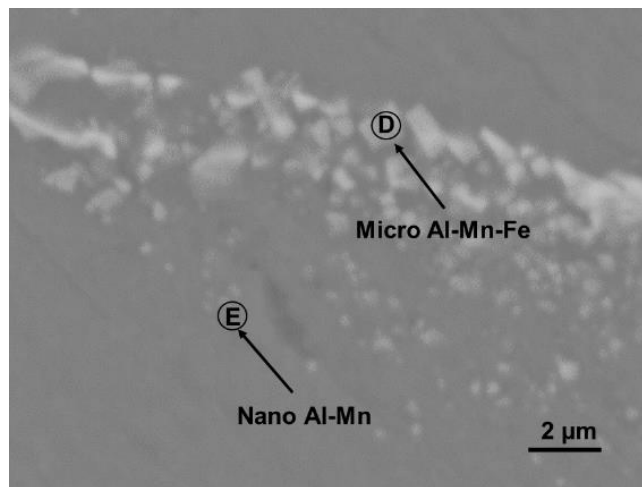
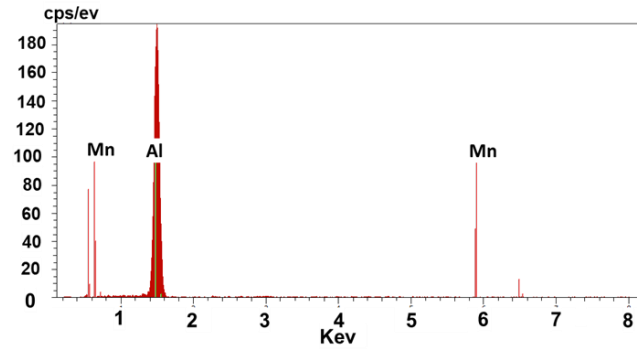
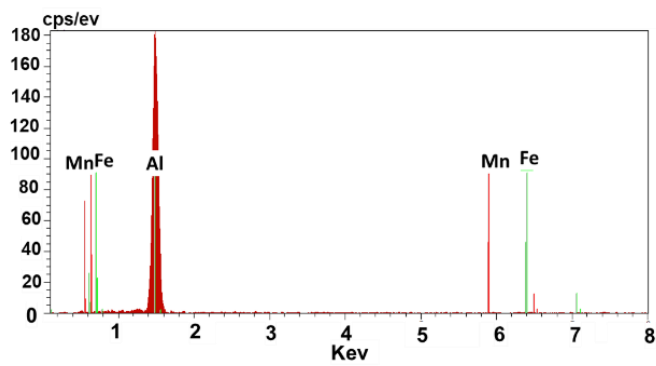


Figure 4.5 Enlarged SEM micrograph showing the presence of the nano eutectic Al-Mn phase in the section of 10 mm, respectively.



(a)



(b)

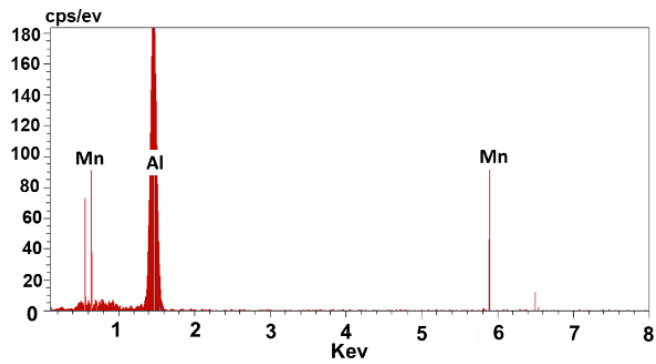


Figure 4.6 EDS spectra (a), (b), and (c) for the areas containing the primary α -Al phase (area A, dark grey), the nano Al-Mn intermetallic phase (area B, light white), and micron Al-Fe-Mn intermetallic phases (area C, light grey), as shown in Figure 4.6(b),

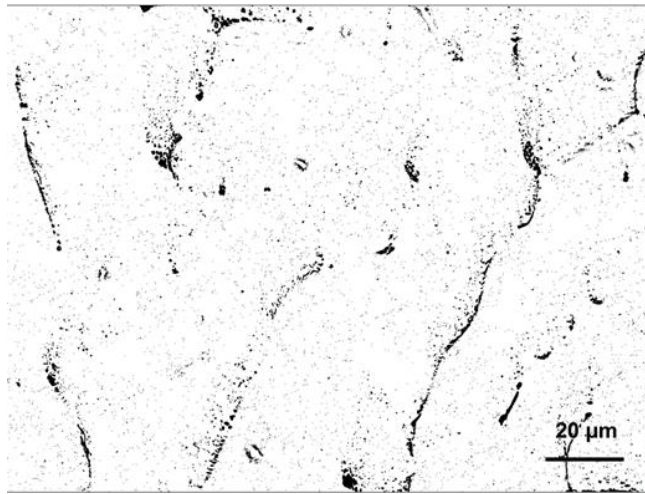
(c)

Table 4.3 Elements in analyzed phase shown in Figures 4.4 and 4.5.

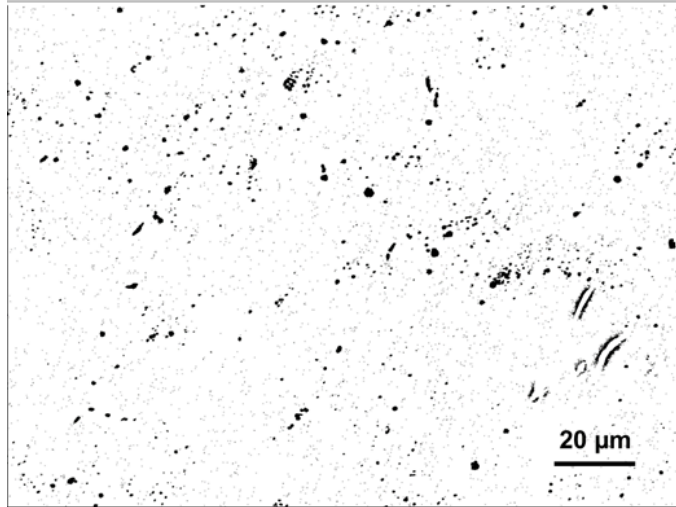
| Phase | Element (wt%) | Section thickness (mm) | | |
|-----------------|------------------|------------------------|-------|-------|
| | | 6 | 10 | 20 |
| α -Al | Al | 99.86 | 99.89 | 99.93 |
| | Mn | 0.14 | 0.11 | 0.07 |
| Nano Al-Mn | Al | 98.75 | 98.76 | 98.90 |
| | Mn | 1.25 | 1.24 | 1.10 |
| Micron Al-Mn-Fe | Al | 96.46 | 96.58 | 95.59 |
| | Mn | 0.30 | 0.41 | 0.89 |
| | Fe | 3.24 | 3.00 | 3.51 |

To determine the area fraction of the intermetallic phases, ImageJ was employed to convert SEM micrographs to binary black and white images. the eutectic Al phase was displayed by black areas, while white areas represented the primary α -Al phase in the binary images. Figure 4.7 shows the converted micrographs highlighting the presence of the intermetallics in the observed alloy represented by the black areas. As shown in Figure 4.8, the area fraction of the intermetallics varied with the section thicknesses. The area fractions of the Al-Mn-Fe and Al-Mn intermetallic phases in the PSMC Al-0.3Mn alloys were 3.1%, 2.1%, and 0.8% for the sections of 6, 10 and 20 mm, respectively. Compared to the low content of the intermetallic phase in the thick section, the high content of the intermetallic phases in the section of 6 mm arose from the high cooling rate. Furthermore,

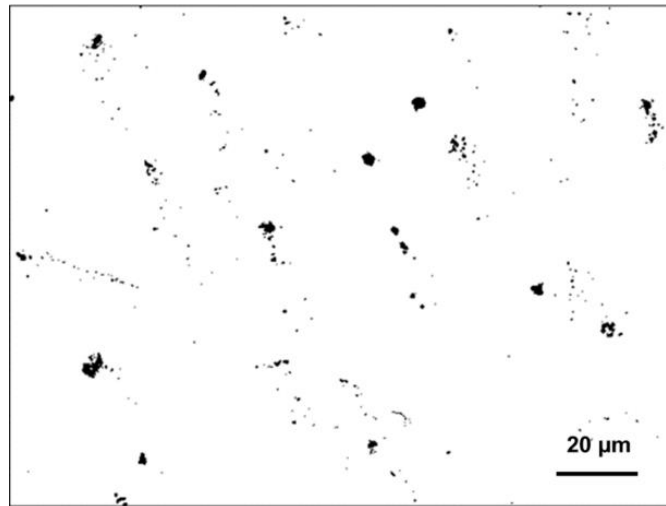
the rapid solidification resulted in the presence of the nano eutectic Al-Fe phase more extensive in the 6-mm section than those in the 10-mm and 20-mm sections, as shown in Figure 4.9. However, the detection of the relatively high Mn (0.89 at%) content in the Al-Mn-Fe phase and low Mn level (0.07 at%) in the primary α -Al grain of the 20-mm section implied that the slow cooling promoted the migration of Mn from the primary phase to the micron Al-Mn-Fe phase during solidification. As a result, the relatively large Al-Mn-Fe particles were formed in the 20-mm sample. The previous studies [21, 22] showed the similar cooling effect on the microstructure of Al alloys.



(a)



(b)



(c)

Figure 4.7 Binary black and white images showing the eutectic content in the PSMC Al-0.3Mn alloy with the section thicknesses of (a) 6, (b) 10, and (c) 20 mm, respectively.

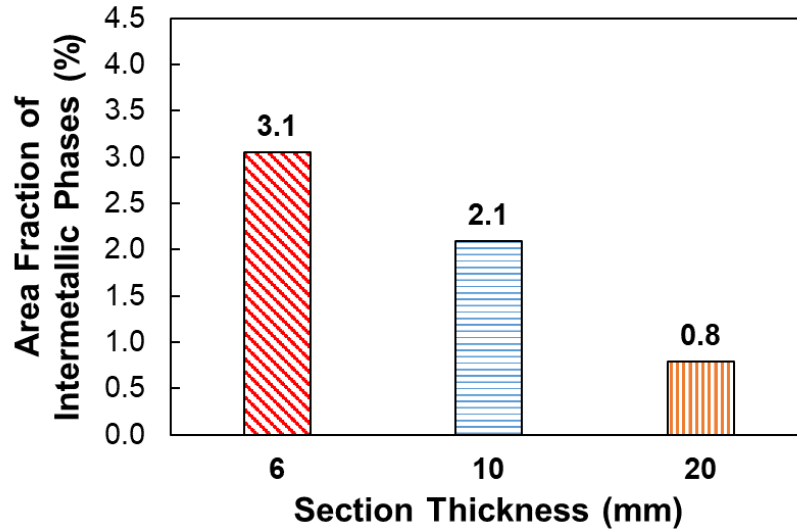
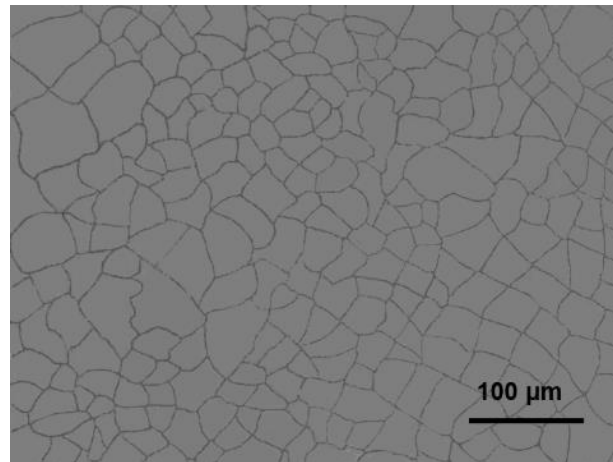


Figure 4.8 Area fractions of the intermetallic phases in the PSMC Al-0.3Mn alloy vs. section thickness.

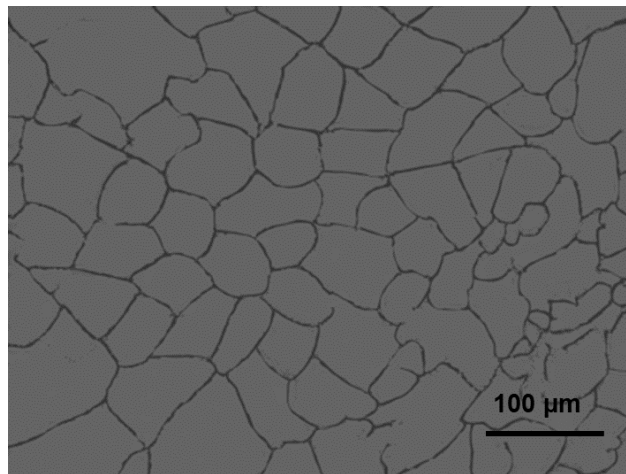
4.3.3 Dendrite size

Figure 4.9 shows optical micrographs taken from the PSMC Al-0.3Mn alloys with the section thicknesses of 6, 10 and 20 mm, respectively. The average sizes of the primary α -Al dendrites were 29, 65, and 106 μm for the sections of 6, 10, and 20 mm, respectively, which are revealed in Figure 4.10. It is worth noting that the primary dendrite size was reduced by three times, as the section thickness decreased from 106 to 29 μm . This should be attributed to the fact that the large amount of thermal energy present in the thick section of liquid alloy required extra time for removal during solidification, as the thermal conductivity and mold temperature were the same for all the sections. It took relatively long time for the thick section to be solidified at the solidification temperature (around 660 $^{\circ}\text{C}$) as illustrated in Figures 4.2 and 4.3. The long solidification time enabled the dendrites to grow and develop a coarse structure (Figure 4.9(c)). In other words, the thin section in

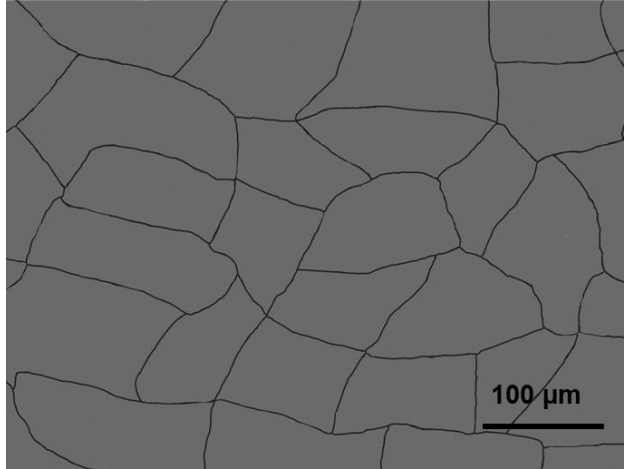
the same mold experienced a rapid cooling rate and resulted in a fine dendritic structure as illustrated in Figure 4.9(a).



(a)



(b)



(c)

Figure 4.9 Optical micrographs revealing the primary α -Al dendrites in the PSMC Al-0.3Mn alloy with the section thicknesses of 6, 10, and 20 mm, respectively.

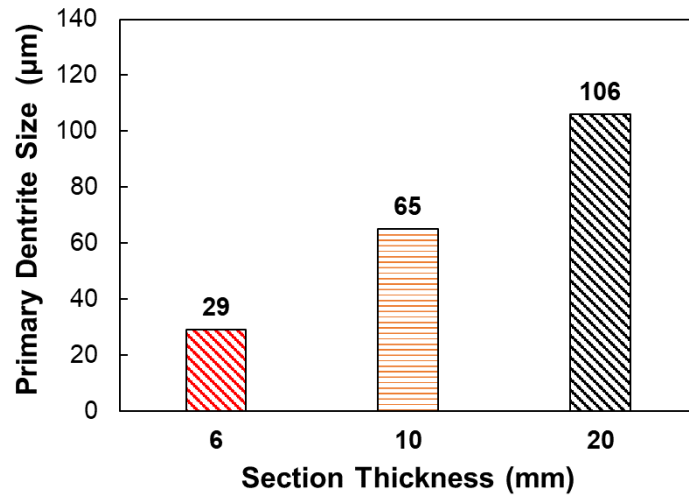
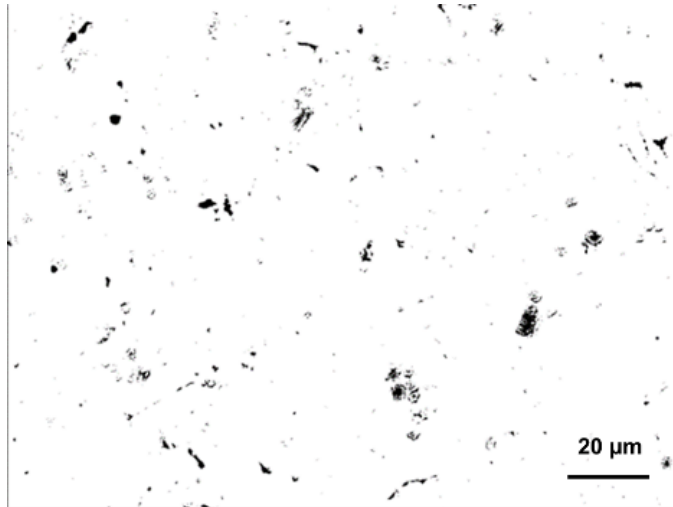


Figure 4.10 Average primary dendrite size in the PSMC Al-0.3Mn alloy with the section thicknesses of 6, 10 and 20 mm.

4.3.4 Porosity evaluation

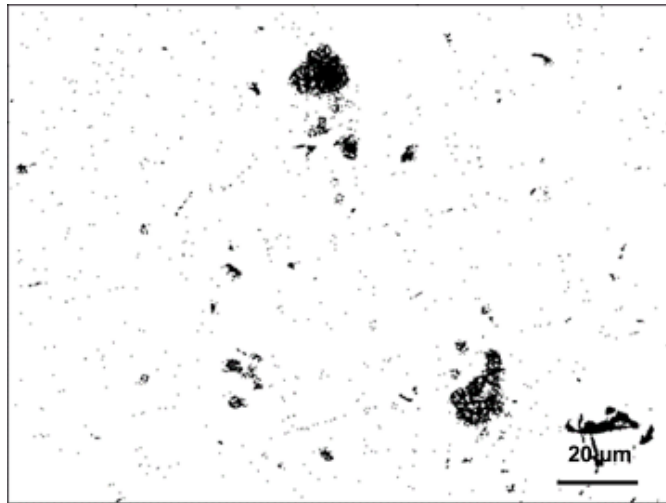
Figure 4.11 presents the binary black and white images converted from SEM micrographs (Figure 4.4) showing the porosity in the different sections of the PSMC Al-0.3Mn alloy. Despite the presence of very few and small pores in the 6 mm specimens as shown in Figure 4.11(a), a number of large pores were evidently present in both the 10 mm and 20 mm specimens as illustrated in Figures 4.10(b) and (c), respectively. Figure 4.12 depicts the porosity contents of the alloy varying with the section thickness. The image analyses indicated that the sections with the thicknesses of 6, 10 and 20 mm had the porosity levels of 1.09%, 2.20% and 2.40%, respectively. Meanwhile, the porosity contents determined by Archimedes principle were 1.25%, 2.26% and 2.58% for the sections of 6, 10 and 20 mm, respectively. The porosity measurements with Archimedes principle were consistent with the image analyses. The porosity level rose with increasing the section thickness. The high porosity levels in the thick sections of 10 and 20 mm should be resulted from the slow solidification. The rapid cooling in the thin section reduced the solute segregation and porosity formation, which led to the low porosity content. Also, there was a reduction in the size of the entrapped pores.



(a)



(b)



(c)

Figure 4.11 Binary black and white images showing porosity in the PSMC Al-0.3Mn alloy with the section thicknesses of (a) 6, (b) 10 and (c) 20 mm, respectively.

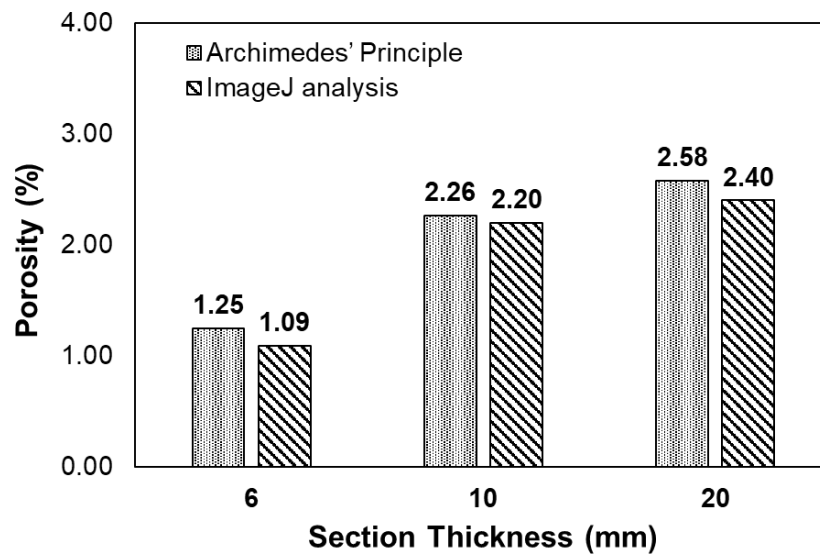


Figure 4.12 Porosity contents vs. section thicknesses.

4.3.5 Tensile Properties

Figure 4.13 shows representative engineering stress and strain curves for the three sections of the PSMC Al-0.3Mn alloy. For all the three sections, the curves show that the alloy deformed elastically first under tensile loading. After reaching the yield point, the alloy started to deform plastically. As shown in Figure 4.13, the slope of the linear portion of the engineering curve for the 6-mm thick specimen had a large increasing tendency than that of the 20-mm counterpart.

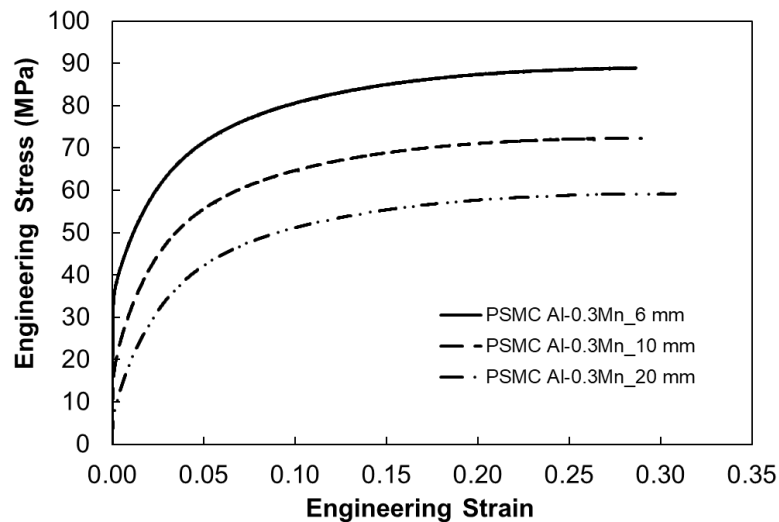


Figure 4.13 Representative engineering stress vs. strain curves of PSMC Al-0.3Mn alloy with different section thickness of 6, 10, and 20 mm, respectively.

Table 4.4 lists the tensile properties of these three different sections including the UTS, YS, e_f , and E, which were extracted from the curves in Figure 4.13. The measured tensile properties were influenced by the section thickness. The UTS, YS, and E increased to 88.9 MPa, 38.7 MPa and 69.9 GPa from 59.2 MPa, 12.4 MPa, and 59.6 GPa, corresponding to the increases of 50.2%, 212.1% and 17.3%, respectively, as the section thickness of the

PSMC Al-0.3Mn decreased to 6 mm from 20 mm. However, the ϵ_f of the PSMC Al-0.3Mn alloy was slightly reduced from 30.8% to 28.6 by only 7.1%, with decreasing the section thickness from 20 to 6 mm. Overall, the thin section generated much higher tensile and yield strengths and moduli than those of the thick section.

Table 4.4 Tensile properties of the PSMC Al-0.3Mn alloy with the section thicknesses of 6, 10 and 20 mm at room temperature.

| Section Thickness (mm) | UTS (MPa) | YS (MPa) | ϵ_f (%) | Modulus (GPa) |
|-------------------------------|------------------|-----------------|------------------------------------|----------------------|
| 6 | 88.9 | 38.7 | 28.6% | 69.9 |
| 10 | 72.3 | 20.4 | 28.9% | 66.3 |
| 20 | 59.2 | 12.4 | 30.8% | 59.6 |

4.3.6 Deformation and Strain Hardening

Resilience

The ability of a material to absorb energy is referred to as resilience when it is deformed elastically, and releases that energy upon unloading. The resilience is usually measured by the modulus of resilience which is defined as the maximum strain energy absorbed per unit volume without creating a permanent distortion. It can be calculated by integrating the stress-strain curve from zero to the elastic limit [5, 23]. In uniaxial tension, the strain energy per unit volume can be determined by the following equation:

$$U_r = \frac{(YS)^2}{2E} \quad (\text{Eq 3})$$

where U_r is the modulus of resilience, YS is the yield strength, and E is the Young's or elastic modulus. The calculated modulus of resilience for the PSMC Al-0.3Mn alloy with three different section thicknesses given in Table 4.5. The comparison of the 6 mm and 20 mm sections indicated that the modulus of resilience for the 6 mm was 10.7 kJ/m^3 much higher than that of the 20 mm (1.3 kJ/m^3). This implies that PSMC Al-0.3Mn alloy with the 6 mm section was much more capable of resisting energy loads in engineering application during service, in which no permanent deformation and distortion were allowed. This was because the 6 mm alloy had a much high YS compared to those of the 10-mm and 20-mm samples.

Toughness

The tensile toughness of a ductile alloy is its ability to absorb energy during static loading condition, i.e., static deformation with a low strain rate. The ability to bear applied stresses higher than the yield strength without fracturing is usually required for various engineering applications. The toughness for ductile alloys can be considered as the total area under the stress-strain curve for the amount of the total energy per unit volume. To evaluate the deformation behavior, the energy expended in deforming a ductile alloy per unit volume given by the area under the stress-strain curve can be approximated by

$$U_t = U_{el} + U_{pl} = \frac{(YS+UTS) \times e_f}{2} \quad (\text{Eq 4})$$

where U_t is the total energy per unit volume required to reach the point of fracture, U_{pl} is the energy per unit volume for elastic deformation, U_{el} is the energy per unit volume for plastic deformation and e_f is the elongation at fracture [5, 24]. Table 4.5 lists the calculated

U_t for the PSMC Al-0.3Mn alloy with the different section thicknesses. The PSMC Al-0.3Mn alloy with the 6-mm section had a U_t value of 18.3 MJ/m³, which was 66.4% higher than that (11.0 MJ/m³) of the 20 mm sample and 36.6% higher than that (13.4 MJ/m³) of the 10 mm section, suggesting that the 2 mm alloy was much tougher than the 10 and 20 mm counterparts. The obtained tensile toughnesses resulted from the fact that the PSMC Al-0.3%Mn alloy with the 6 mm section had the high ultimate tensile strength and yield strength, and a comparable elongation. As a result, the total area under the engineering stress and strain curve was greater for the 6 mm specimen.

Table 4.5 Tensile toughnesses and resiliences of PSMC Al-0.3Mn alloy at room temperature

| Section Thickness (mm) | Resilience (kJ/m³) | Toughness (MJ/m³) |
|-----------------------------------|--|---|
| 6 | 10.7 | 18.3 |
| 10 | 3.1 | 13.4 |
| 20 | 1.3 | 11.0 |

Strain Hardening

To understand the tensile deformation behavior, the true stress and strain were calculated from the engineering stress and strain by:

$$\sigma_t = \sigma (1 + \varepsilon) \quad (\text{Eq 5})$$

$$\varepsilon_t = \ln(1 + \varepsilon) \quad (\text{Eq 6})$$

where σ is the engineering stress, ε is the engineering strain, σ_t is the true stress and ε_t is the true strain [25]. Figure 4.14 shows the representative true stress and strain curves of the PSMC Al-0.3Mn alloy with the three section thicknesses. Under tensile loading, the tensile specimens deformed elastically first. Once the yield points reached, plastic deformation of the alloy set in. However, the fracture of the 6 mm alloy occurred at a much higher stress and strain than those of the 10 and 20-mm thick specimens.

The true stress and strain for plastic deformation can be related by the power law equation:

$$\sigma_t = K \varepsilon_t^n \quad (\text{Eq 7})$$

where K is the strength coefficient and n is the strain-hardening exponent [24]. The regression analysis indicated that the power expression agreed well with the tensile data. The numerical values of the derived constants in Eq (7) with the regression coefficients (R^2) are listed in Table 4.6. The high strain-hardening exponent for the PSMC Al-0.3Mn alloy implied that the 6-mm thick specimen would gain strength more quickly than the 20-mm specimen counterpart during deformation.

Table 4.6 Best fit parameters for power equations

| Section Thickness (mm) | K (MPa) | n | R² |
|-----------------------------------|--------------------|----------|----------------------|
| 6 | 137.35 | 0.222 | 0.996 |
| 10 | 165.17 | 0.3503 | 1.000 |
| 20 | 189.69 | 0.4927 | 0.995 |

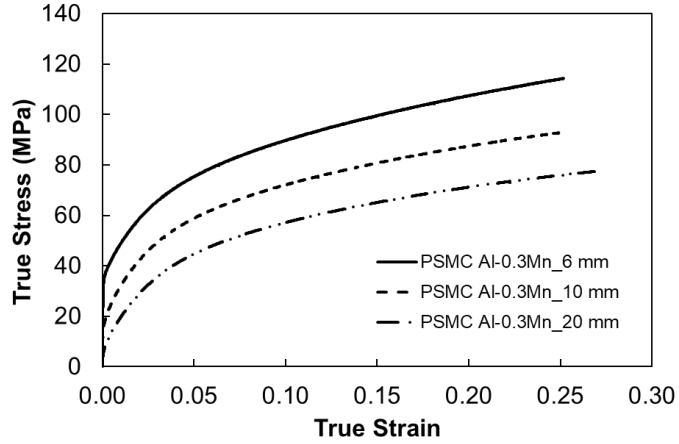


Figure 4.14 Representative true stress vs. strain curves of the PSMC Al-0.3Mn alloy with the three section thicknesses of 6, 10, and 20 mm.

To determine the strain-hardening rate ($d\sigma_t/d\varepsilon_t$), Eq (7) was differentiated to obtain:

$$\frac{d\sigma_t}{d\varepsilon_t} = K n \varepsilon_t^{n-1} \quad (\text{Eq 8})$$

Figure 4.15 presents the strain-hardening rate versus true plastic strain curve during the plastic deformation, which was derived from the true stress versus true strain curve (Figure 4.13). Upon the onset of plastic deformation at a strain of 0.002, the strain-hardening rate of the 6 mm specimen was 3826 MPa, as the 20-mm specimen exhibited a strain-hardening rate of only 2180 MPa. As shown in Figure 4.12, in the early stage of plastic deformation, the strain-hardening rate of the 2 mm-thick PSMC Al-0.3Mn alloy was 75.5% higher than that of the 20-mm specimen. This observation of the variation of strain-hardening rate versus strain suggested that, compared to the 10 mm and 20 mm thick sections, the PSMC Al-0.3Mn with the thin section (6 mm) could strengthen itself spontaneously to a large extent, in response to the initial plastic deformation.

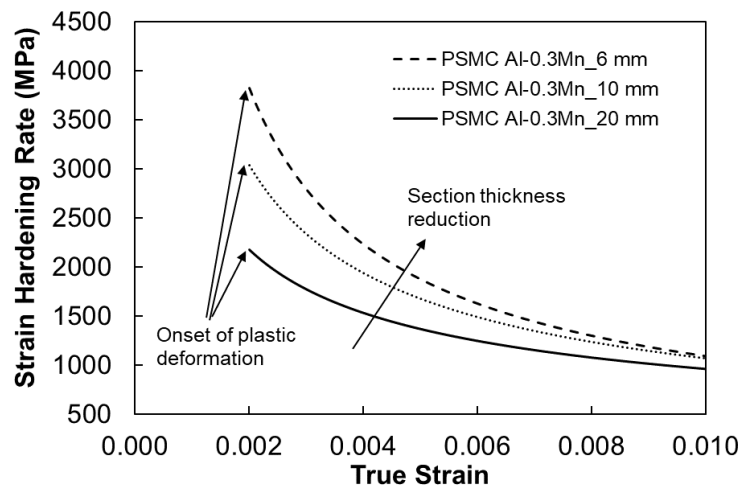


Figure 4.15 Strain hardening rates vs. true strain for plastic deformation of the PSMC Al-0.3Mn alloy with the three section thicknesses of 6, 10 and 20 mm.

4.4 ELECTRICAL CONDUCTIVITIES

Figure 4.16 shows the electrical conductivities of the PSMC Al-0.3Mn alloy with the different section thicknesses. It can be seen from Figure 4.15 that the electrical conductivities for the 6, 10 and 20-mm sections were 45.77, 45.57 and 45.36 %IACS, respectively. There was a decrease of 0.4 %IACS and 0.5 %IACS in the electrical conductivity, as the section thickness of the alloy increased from 6 mm to 10 and 20 mm, respectively. The observation on the variation of the electrical conductivities suggested that the Mn addition of 0.3 wt% had an insignificant effect on the electrical conductivity of the alloy, even when the as-cast section thickness changed considerably. The little change of the electrical conductivity should be attributed to the fact that the very similar phase constituents (micron Al-Mn-Fe phase and nano Al-Mn intermetallics) and morphology were present in the three sections of 6, 10, and 20 mm. The intermetallic contents, varying porosity levels and primary dendrite size might be responsible for the conductivity variation in the different sections of the alloy [20].

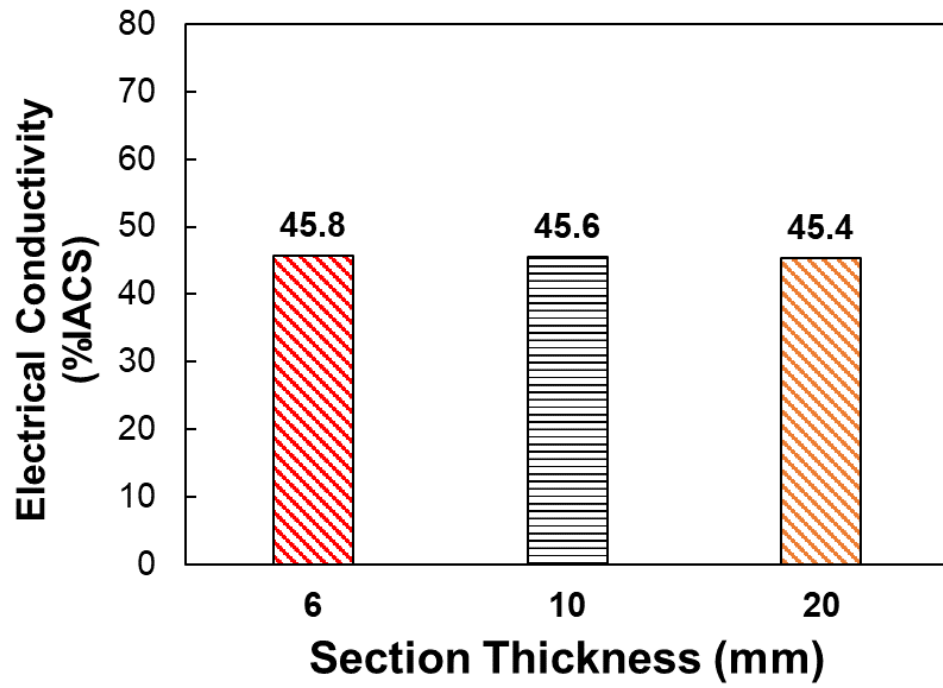


Figure 4.16 Electrical conductivities vs. Section Thickness.

4.5 CONCLUSIONS

The effect of the section thicknesses on microstructure, mechanical and electrical properties of the Al-0.3Mn alloy prepared by the permanent steel mold casting was studied. The conclusions drawn from this research were given below.

- (1) The numerical simulation predicted that the cooling rates of the PSMC Al-0.3Mn alloy increased from 2.1 °C/s to 23.8 °C/s with decreasing the section thicknesses from 20 mm to 6 mm, which implied fine microstructure in the thin section.
- (2) The microstructures of the PSMC Al-0.3Mn alloy consisted of the primary α -Al dendrites, and micron Al-Mn-Fe and nano Al-Mn intermetallic phases. The average sizes of the primary α -Al dendrites were 29, 65, and 106 μm for the sections of 6, 10 and 20 mm, respectively. The area fractions of the Al-Mn-Fe and Al-Mn intermetallic phases in the PSMC Al-0.3Mn alloys were 3.1%, 2.1%, and 0.8% for the sections of 6, 10 and 20 mm, respectively. The reduction in the section thickness decreased the dendrite size, but increased the fraction of the micron Al-Mn-Fe and nano Al-Mn intermetallic phases, since the high cooling rate was present in the thin section.
- (3) The porosity content rose from around 1% to about 2.58%, as the section thickness increased from 6 to 20 mm, respectively. The high porosity levels in the thick section should be resulted from the slow cooling.
- (4) The measured tensile properties of the alloy were influenced by the section thickness. The UTS, YS, and E of the alloy increased to 88.9 MPa, 38.7 MPa, and 69.9 GPa from 59.2 MPa, 12.4 MPa, and 59.6 GPa, respectively, but e_f decreased

slightly to 28.6% from 30.8%, as the section thickness of the PSMC Al-0.3Mn decreased to 6 from 20 mm.

- (5) The analyses of the deformation behavior indicated that the toughness, resilience, and strain hardening rate, increased significantly with a reduction in the section thickness of the alloy, implying the thin section could absorb high energy and strengthen itself spontaneously to a large extent during deformation.
- (6) The electrical conductivities for the 6, 10 and 20-mm sections were 45.77, 45.57 and 45.36 %IACS, respectively. The section thicknesses had a limited effect on the electrical conductivity of the alloy with varying the section thickness.

4.6 REFERENCES

- [1] Yuxian Li, Anita Hu, Yintian Fu, Sufeng Liu, Wutian Shen, Henry Hu and Xueyuan Nie, Al Alloys and Casting Processes for Induction Motor Applications in Battery-Powered Electric Vehicles: A Review, *Metals*. 2022, 12, 216-241.
- [2] W. Shen, A. Hu, S. Liu, H. Hu, Al-Mn alloys for electrical applications: a review, *Journal of Alloys and Metallurgical Systems*, 2023, 2, <https://doi.org/10.1016/j.jalmes.2023.100008>.
- [3] Sivanesh, P.; Charlie, K.; Robert, S.J.; Ethan, F.; Paul, E. Aluminum Alloys for Die Casting. U.S. Patent No. WO 2020/028730 A1, 6 February 2020.
- [4] Joachim Doerr, Nikolai Ardey, Günther Mendl, Gerhard Fröhlich, Roman Straßer, Thomas Laudénbach, The new full electric drivetrain of the Audi e-tron, In: Liebl, J. (eds) *Der Antrieb von morgen 2019. Proceedings*. Springer Vieweg, Wiesbaden. https://doi.org/10.1007/978-3-658-26056-9_2
- [5] Yintian Fu, Yuxian Li, Anita Hu, Henry Hu, and Xueyuan Nie, Microstructure, Tensile Properties and Fracture Behavior of Squeeze Cast Mg Alloy AZ91 with Thick Cross Section, *Journal of Materials Engineering and Performance*. 2020, 29, 4130-4141.
- [6] J. R. Davis, (Ed.) *ASM Specialty Handbook: Aluminum and Aluminum Alloys*; ASM International: Materials Park, OH, USA, 2002.
- [7] M. Y. Murashkin, I., Sabirov, X., Sauvage, & R. Z. Valiev, Nanostructured Al and Cu alloys with superior strength and electrical conductivity, *J Mater Sci*. 2016, 51(1), 33-49.
- [8] S. Liu, A. Hu, H. Hu, X. Nie, and N. C. Kar, Potential Al-Fe Cast Alloys for Motor

- Applications in Electric Vehicles: An Overview, *Key Engineering Materials*. 2022, 923, 3-19.
- [9] B. Grushko, D. Pavlyuchkov, S.B. Mi, S. Balanetsky, Ternary phases forming adjacent to $\text{Al}_3\text{Mn}-\text{Al}_4\text{Mn}$ in Al-Mn-TM (TM = Fe, Co, Ni, Cu, Zn, Pd), *J. Alloys Compd.* Vol. 677 (2016) 148-162.
- [10] A. J. McAlister, J. L. Murray, The (Al-Mn) aluminum-manganese system - journal of phase equilibria. *Bulletin of Alloy Phase Diagrams*. 1987, 8(5).
- [11] H. Hu, M. Zhou, Z. Sun, N. Li, Tensile behaviour and fracture characteristics of die cast magnesium alloy AM50. *J. Mater. Process. Technol.* 2008, 201(1-3), 364-368.
- [12] G. Gu, S. Lin, Y. Xia, Q. Zhou, Experimental study on influence of section thickness on mechanical behavior of die-cast AM60 magnesium alloy. *Materials & Design*. 2012, 38, 124-132.
- [13] X. Zhang, M. Wang, Z. Sun, H. Hu, Section thickness-dependent tensile properties of squeeze cast magnesium alloy AM60. *China Foundry*. 2012, 9(2), 178-183.
- [14] Zixi Sun, Xinyu Geng, Luyang Ren, and Henry Hu, Microstructure, Tensile Properties and Fracture Behavior of HPDC Magnesium Alloy AZ91, *International Journal of Materials, Mechanics and Manufacturing*. 2020, 8 (2), 50-56.
- [15] Li Fang, Xuezhi Zhang, Luyang Ren, Henry Hu, Xueyuan Nie, and Jimi Tjong, Effect of Ni addition on tensile properties of squeeze cast Al alloy A380. *Advances in Materials and Processing Technologies*. 2018, 4(2), 200-209.
- [16] Standard Test Method for Density of High-Modulus Fibers, D3800-99, *ASTM Standards*, ASTM, Vol 15.03, 2002, 186-187.

- [17] Standard Test Method for Dry and Wet Bulk Density, Water Absorption, and Apparent Porosity of Thin Sections of Glass-Fiber Reinforced Concrete,” C948-81, ASTM Standards, ASTM, Vol 04.05, 2002, 588-589.
- [18] T.J. Collins, ImageJ for Microscopy, Biotechniques, 2007, 43(1), S25–S30
- [19] Standard Test Methods for Tension Testing Wrought and Cast Aluminum-and Magnesium-alloy Products,” B557M, ASTM Standards, ASTM, Vol 02 02, 2002, 424-439.
- [20] Y. Li, Y. Fu, A. Hu, X. Nie, H. Hu, Effect of Sr and Ni Addition on Microstructure, Tensile Behavior and Electrical Conductivity of Squeeze Cast Al-6Si-3Cu Al Alloy. Key Engineering Materials. 2022, 921, 3-14.
- [21] S. Kotiadis, A. Zimmer, A. Elsayed, E. Vandersluis & C. Ravindran, High Electrical and Thermal Conductivity Cast Al-Fe-Mg-Si Alloys with Ni Additions, Metallurgical and Materials Transactions A. 2020, 51, 4195–4214.
- [22] Y.H. Zhang, Y.C. Liu, Y.J. Han, C. Wei, Z.M. Gao, The role of cooling rate in the microstructure of Al-Fe-Si alloy with high Fe and Si contents, J. Alloy. Compd. 2009, 473, 442–445.
- [23] William D. Callister, JR., David G. Rethwisch, Materials Science and Engineering, John Wiley & Sons, Hoboken, NJ, 2018, 161-166.
- [24] Toughness, NDT Education Resource Center, Brian Larson, Editor, 2001-2011, The Collaboration for NDT Education, Iowa State University.
- [25] Qiang Zhang, Mohsen Masoumi and Henry Hu, Influence of Applied Pressure on Tensile Behaviour and Microstructure of Squeeze Cast Mg Alloy AM50 with Ca

Addition, J. Mater. Eng. Perform. 2012, 21, 38-46.

Chapter 5: Conclusions

The conclusions drawn from this study can be classified into three categories based on eight research objectives:

I. **Difference between Permanent steel mold cast (PSMC) Al-0.3Mn Alloy and high-purity (HP) Al (99.9%) in mechanical and electrical properties**

1. The results of tensile testing of the PSMC Al-0.3Mn alloy and HP Al showed that the UTS, YS and resilience of the PSMC Al-0.3Mn alloy were 72.3 and 20.4 MPa, and 3.14 kJ/m³, respectively, which were higher than those (59.2 and 14.0 MPa, and 1.61 kJ/m³) of the PSMC HP Al.
2. The toughness of the PSMC Al-0.3Mn alloy was 13.40 MJ/m³, which was comparable to that (13.58 MJ/m³) of the PSMC HP Al.
3. But, the elongation of the PSMC Al-0.3Mn alloy was only 28.9%, which was lower than that (37.1%) of the PSMC HP Al. The difference in tensile behavior between the PSMC Al-0.3Mn alloy and the HP Al should be attributed to the fact that the relatively large amount of the micron Al-Fe-Mn and nano Al-Mn intermetallic phases was present in the PSMC Al-0.3Mn alloy, compared to almost little intermetallic phase in the PSMC HP Al.
4. The addition of 0.3 wt% Mn affected the electrical conductivity of the PSMC HP Al, which was only slightly below the industrial specification for the EV motor application.

II. Effect of section thicknesses on microstructure, mechanical and electrical properties PSMC Al-0.3Mn Alloy

1. The numerical simulation predicted that the cooling rates of the PSMC Al-0.3Mn alloy increased from 2.1 °C/s to 23.8 °C/s with decreasing the section thicknesses from 20 mm to 6 mm, which implied fine microstructure in the thin section.
2. The microstructures of the PSMC Al-0.3Mn alloy consisted of the primary α -Al dendrites, and micron Al-Mn-Fe and nano Al-Mn intermetallic phases. The average sizes of the primary α -Al dendrites were 29, 65, and 106 μm for the sections of 6, 10 and 20 mm, respectively. The area fractions of the Al-Mn-Fe and Al-Mn intermetallic phases in the PSMC Al-0.3Mn alloys were 3.1%, 2.1%, and 0.8% for the sections of 6, 10 and 20 mm, respectively. The reduction in the section thickness decreased the dendrite size, but increased the fraction of the micron Al-Mn-Fe and nano Al-Mn intermetallic phases, since the high cooling rate was present in the thin section.
3. The porosity content rose from around 1% to about 2.58%, as the section thickness increased from 6 to 20 mm, respectively. The high porosity levels in the thick section should be resulted from the slow cooling.
4. The measured tensile properties of the alloy were influenced by the section thickness. The UTS, YS, and E of the alloy increased to 88.9 MPa, 38.7 MPa, and 69.9 GPa from 59.2 MPa, 12.4 MPa, and 59.6 GPa, respectively, but ϵ_f

decreased slightly to 28.6% from 30.8%, as the section thickness of the PSMC Al-0.3Mn decreased to 6 from 20 mm.

5. The analyses of the deformation behavior indicated that the toughness, resilience, and strain hardening rate, increased significantly with a reduction in the section thickness of the alloy, implying the thin section could absorb high energy and strengthen itself spontaneously to a large extent during deformation.
6. The electrical conductivities for the 6, 10 and 20-mm sections were 45.8, 45.6 and 45.4 %IACS, respectively. The section thicknesses had a limited effect on the electrical conductivity of the alloy with varying the section thickness.

Chapter 6: Future Work

The following are the suggestions for the future work.

- Study the effect of different section thicknesses of squeeze cast Al-0.3Mn alloy on microstructure, mechanical and electrical properties, and fracture behavior;
- Investigate the effect of different pressures applied in squeeze cast on microstructure, mechanical and electrical properties, and fracture behavior of Al-0.3Mn alloy;
- Investigate the effect of different Mn contents in terms of weight percentages on microstructure, mechanical and electrical properties, and fracture behavior of Al alloys;
- Investigate the potential of other low solubility alloying elements in aluminum alloys (Ni, Sr, and Ca), which could be used for motor application in electric vehicle to reach high electrical conductivity and strengths.
- Study the effects of heat treatment and local Cu chill cooling on mechanical and electrical properties of the Al-0.3Mn alloy.

APENDICES

Congratulations!

We are pleased to inform you that the review processes for 2023 14th International Conference on Materials and Manufacturing Technologies (ICMMT 2023) has been completed. The conference received submissions from different countries and regions which were reviewed by international experts. Based on the recommendations of the reviewers and the Technical Program Committees, we are pleased to inform you that your paper has been accepted for publication and presentation. You are cordially invited to present the paper at ICMMT 2023 to be held in **Ho Chi Minh City, Vietnam in hybrid virtual style on March 24-26, 2023.**

Paper ID: HM201

**Paper Title: An Overview of Mn-containing Al Alloys for Applications in Electric Vehicles:
Electrical Conductivities, Mechanical Properties and Microstructure**

After careful reviewing processes, the above paper after proper registration and presentation will be published in a volume of **Key Engineering Materials (ISSN print 1013-9826; ISSN cd 1662-9809; ISSN web 1662-9795)**, and submitted for **SCOPUS, SCImago Journal & Country Rank (SJR), Inspec (IET, Institution of Engineering Technology), Chemical Abstracts Service (CAS) index.**

Congratulations on your accepted paper! Thank you for choosing to publish in Journal of Alloys and Metallurgical Systems. Please read this e-mail carefully as it contains important information.

FINALIZE PUBLISHING YOUR ARTICLE:

We work hard to publish our authors' articles online as quickly as possible, so we're happy to report that processing of your manuscript has already begun. To ensure that we publish your article in accordance with your wishes, please now complete these forms

<https://can01.safelinks.protection.outlook.com/?url=http%3A%2F%2Fauthors.elsevier.com%2Fauthorforms%2FJALMES100008%2F3d4a89a450c2df94e265a66445dab8eb&data=05%7C01%7Cuh%40uwindsor.ca%7Cde22f3bb48844179ac3908db4b91b695%7C12f933b33d614b199a4d689021de8cc9%7C0%7C0%7C638186861432348903%7CUnknown%7CTWFpbGZsb3d8eyJWJoiMC4wLjAwMDAiLCJQIjoiV2luMzliLCJBTiI6Ikh1haWwiLCJXCI6Mn0%3D%7C3000%7C%7C%7C&sdata=LHWCpRwr1DayqdpdrPlo7jkm2P1JMehpcIDT9KEDPxw%3D&reserved=0>

If this link does not work, please copy the entire URL (noting that it may run on to a second line in this message) into your browser. You should log in with your Elsevier Profile credentials, which you may have already created when submitting your article.

ACCEPTANCE OF ABSTRACT AS PRESENTER IN 24th INTERNATIONAL CONFERENCE ON ADVANCES IN MATERIALS & PROCESSING TECHNOLOGIES (AMPT 2023)

On behalf of the AMPT 2023 organizing committee, we are pleased to inform you that your abstract submission has been accepted for presentation at the conference.

Your proposed topic and research align well with the theme of our conference, and we believe that your presentation will make a valuable contribution to the event.

Paper ID : 29

Title : SECTION THICKNESS EFFECT ON MECHANICAL AND ELECTRICAL PROPERTIES OF PERMANENT STEEL MOLD CAST AL-0.3MN ALLOY

We appreciate your commitment to submitting the payment and other required documents on time through our online system and adhering to the allotted time limit for your session. Registration will be secured once payment has been made and verified by the organizer. The deadline, registration fee details, and other important information are as stated on our official website:

<https://www.ampt2023.org/home>.

VITA AUCTORIS

NAME: Wutian Shen

PLACE OF BIRTH: Jiangsu, China

YEAR OF BIRTH: 1998

EDUCATION: University of Windsor, B.Sc., Windsor, ON, 2021

University of Windsor, M.Sc., Windsor, ON, 2023